Combined Faculties of the Natural Sciences and Mathematics
Ruperto-Carola-University of Heidelberg, Germany

ON SHEAR AND FLEXION MEASUREMENTS AND PROPERTIES OF DARK MATTER HALOS

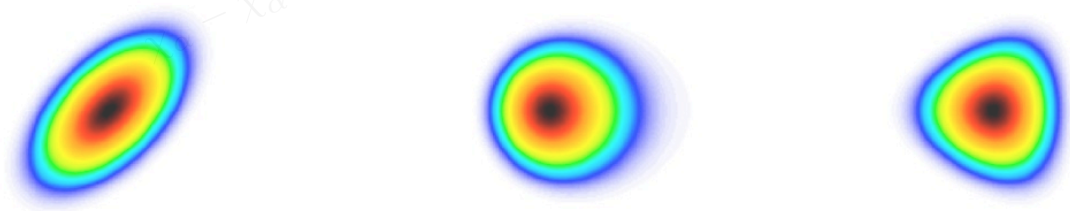

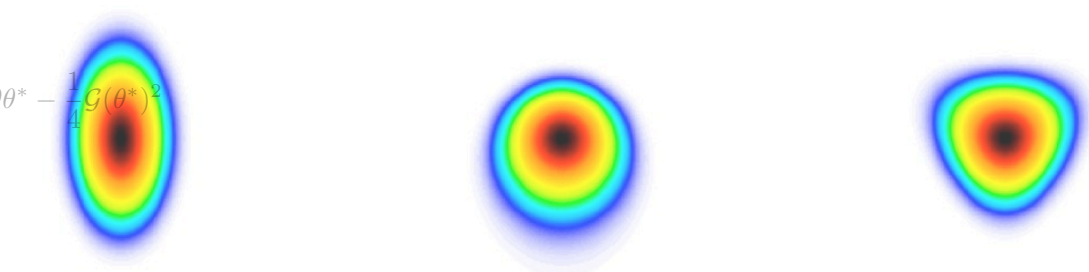

Massimo Viola

Dissertation

submitted to the

Combined Faculties of the Natural Sciences and Mathematics

of the Ruperto-Carola-University of Heidelberg, Germany

for the degree of

Doctor of Natural Sciences

Put forward by

Massimo Viola

born in: Trieste, Italy

Oral examination: December 15, 2010

ON
SHEAR AND FLEXION MEASUREMENTS
AND
PROPERTIES OF DARK MATTER HALOS

Referees: Prof. Dr. Matthias Bartelmann

Prof. Dr. Luca Amendola

Zusammenfassung: In dieser Arbeit untersuchen wir die Kaiser-Squires-Broadhurst-Methode (KSB) zur Abschützung der gravitativen Scherung anhand von Momenten der Flächenhelligkeit kleiner und verrauschter Galaxienbilder. Wir zeigen, in welcher Weise KSB auf einschränkenden mathematischen Annahmen beruht, die das Verhältnis von gefalteter zu ungefalteter Elliptizität, die Form der Punktbildfunktion des Teleskops ebenso wie die Beziehung zwischen Elliptizität und Scherung betreffen und von denen keine in Wirklichkeit erfüllt ist. Wir schlagen Verbesserungen des ursprünglichen KSB-Verfahrens vor und zeigen, dass diese Erweiterungen Fehleinschätzungen in Scherungsmessungen deutlich reduzieren. Darüber hinaus diskutieren wir die Unmäglichkeit, die Annahmen über die Form der Punkbildfunktion im Rahmen von KSB abzuschwächen. Aus diesem Grund entwickeln wir eine neuartige Methode für Messungen des schwachen Gravitationslinseneffekts, DEIMOS, die auf einer mathematisch exakten Entfaltung der Momente der scheinbaren Flächenhelligkeit von der Punktbildfunktion beruht. Wir weisen durch eine Reihe spezailisierter Tests die Genauigkeit und die Stärke dieser neuen Methode nach und zeigen anhand der Daten des GREAT08-Wettbewerbs, wie konkurrenzfähig diese Methode ist.
Darüber hinaus stellen wir eine mögliche Anwendung von Scherungsmessungen auf die Untersuchung der Eigenschaften von Galaxienhaufen dar. Sie beruht auf linearen Filtertechniken und schätzt die innere Steigung des Dichteprofils in Halos aus dunkler Materie ab. Wir finden, dass unter idealisierten Bedingungen die Genauigkeit der Abschätzung bei 15 % liegt, wenn die Konzentration c des Halos bekannt ist, und bei 30% falls nicht. Wenn die Signale vieler Halos überlagert werden können, sollten ihre Dichteprofile daher durch den vorgeschlagenen linearen Filter gut bestimmt sein. Gegenüber Analysen des starken Gravitationslinseneffekts hat diese Methode den Vorteil, unempfindlich gegenüber Substrukturen in den Galaxienhaufen zu sein.

Summary: In this work we analyse the Kaiser-Squires-Broadhurst method (KSB) to estimate gravitational shear from surface-brightness moments of small and noisy galaxy images. We show how KSB relies on restrictive mathematical assumptions concerning the relation between convolved and unconvolved ellipticity, the shape of the telescope's PSF as well as the relation between ellipticity and shear, neither of which hold in practise. We propose improvements to the original KSB relations and we demonstrate that this extension lowers substantially the biases in the shear measurements. Moreover we discuss the impossibility to weaken the assumption on the PSF shape in the KSB framework. For this reason we develop a novel method for weak-lensing measurements, DEIMOS, which is based on a mathematically exact deconvolution of the moments of the apparent brightness distribution of galaxies from the PSFs. We demonstrate the accuracy and capabilities of this new method with a set of specialized tests and show its competitive performance on the GREAT08 challenge data.
Moreover we present a possible application of shear measurement for studying properties of galaxy clusters based on linear filtering techniques to constrain the inner slope of the density profile of dark-matter halos. We find that under idealised assumptions, the inner slope is constrained to $\sim 15\%$ if the halo concentration c is known, and to $\lesssim 30\%$ if not. If the signals of many halos can be stacked, their density profiles should thus be well constrained by the proposed linear filters with the advantage, in contrast with strong lensing analysis, to be insensitive to the cluster substructures.

Considerate la vostra semenza:
fatti non foste a viver come bruti,
ma per seguir virtute e canoscenza.

Consider well the seed that gave you birth:
you were not made to live your lives as brutes,
but to be followers of worth and knowledge.

Dante (1265-1321) Inferno XXVI

Contents

Contents iii

List of Figures v

List of Tables vii

Introduction ix

1 Cosmology 1
- 1.1 General relativity and cosmological principle . . . 1
- 1.2 The density of the universe . . . 4
- 1.3 Distances . . . 6
- 1.4 Structure formation . . . 8
  - 1.4.1 Gravitational instability . . . 8
  - 1.4.2 Power spectrum . . . 10
- 1.5 Non-linear structure formation . . . 12
  - 1.5.1 The structure of Dark matter halos . . . 14

2 Weak gravitational lensing 17
- 2.1 Weak lensing basics . . . 18
  - 2.1.1 Deflection angle . . . 19
  - 2.1.2 Lens equation . . . 20
  - 2.1.3 Local distortions . . . 21
- 2.2 Lens model . . . 24
  - 2.2.1 NFW lensing properties . . . 24
- 2.3 Cosmic shear . . . 26
  - 2.3.1 3D Weak lensing . . . 30

3 Shear and flexion measurements 33
- 3.1 Measuring ellipticity . . . 33
  - 3.1.1 PSF convolution . . . 36
- 3.2 Available tools . . . 36
  - 3.2.1 Model fitting approach . . . 37
  - 3.2.2 Shapelets . . . 37
  - 3.2.3 Moments . . . 38
- 3.3 From ellipticity to shear . . . 38
- 3.4 Accuracy . . . 39
- 3.5 Flexion measurements . . . 41
  - 3.5.1 Cross talk between shear and flexion . . . 45
  - 3.5.2 On some approximations . . . 46
  - 3.5.3 Tests . . . 47

3.5.4 Outlook 49

4 Bias in, and correction to KSB shear measurements 53
4.1 Standard KSB 54
4.1.1 Shear estimates in KSB 55
4.1.2 Third-order relation between g and χ 57
4.1.3 Tests 59
4.2 PSF convolution 64
4.2.1 PSF anisotropy 68
4.2.2 Tests 69
4.3 Conclusions 70

5 Weak lensing with DEIMOS 75
5.1 Notation 75
5.2 The DEIMOS method 76
5.3 Noise and weighting 77
5.3.1 Deweighting bias 79
5.3.2 Deweighting variance 82
5.4 Shear accuracy tests 83
5.5 Comparison to other methods 87
5.6 Conclusions 88
5.7 Outlook 89

6 Inner density profile of dark matter halos 91
6.1 Methods to characterize the shear profile 92
6.1.1 Optimal linear filtering 92
6.1.2 Scale-adaptive filter 96
6.1.3 Dealing with parameters degeneracy 96
6.2 Method uncertainties 99
6.2.1 Model sensitivity 104
6.3 Potential problems 105
6.4 Conclusion 107

7 Conclusions 111

Appendix A 115

Bibliography 117

Acknowledgments 131

List of Figures

1.1 Distances in our universe 8
1.2 Growth factor 10
1.3 Matter power spectrum 12
1.4 Millennium simulation 13

2.1 Abell 2218 18
2.2 Sketch of a typical lensing configuration 20
2.3 Effect of shear and flexion on a circular source. 23
2.4 Shear profile of a generalized NFW halo 25
2.5 Likelihood contour $(1, 2\sigma)$ for $\Omega_{\rm m}$ and σ_8 27
2.6 Cosmological parameters from shear and magnification. . . 29

3.1 Sketch of PSF convolution 34
3.2 Effect of shear and convergence on a circular source 35
3.3 $\mathcal{F}$ and $\mathcal{G}$ flexion from a NFW halo. 42
3.4 Cross talk between shear and flexion 48
3.5 Cross talk between shear and flexion 50

4.1 KSB shear estimate (no weighting, no PSF) 60
4.2 KSB shear estimation (noise, no PSF) 62
4.3 KSB cross-talk 62
4.4 KSB weighting function dependence 63
4.5 KSB ring test (no PSF) 64
4.6 Dependence of A on the observed ellipticity 71
4.7 Dependence of A on the size of the PSF 71
4.8 KSB shear estimation as a function of PSF size 72
4.9 KSB shear estimation (with PSF, no weighting) 73
4.10 KSB shear estimation (with PSF and weighting) 73

5.1 DEIMOS: weighting-induced bias 81
5.2 DEIMOS:Noise of the deweighted and deconvolved ellipticity 83
5.3 DEIMOS:GREAT08 Q metric and shear accuracy m_i 85

6.1 Optimal filter shape 94
6.2 Recovery of the inner slope using linear filter 95
6.3 Degeneracy between inner slope and concentration 97
6.4 Probability distribution of cluster parameters 100
6.5 Magnification bias 101
6.6 Normalised distributions of the value of α 102
6.7 Normalised distributions of the value of P_1. 102
6.8 σ_α as a function of z and M 104

6.9 Shear bias towards halo's center 106
6.10 σ_α as a function of $n_{\rm gal}$ and $r_{\rm min}$ 106
6.11 Recovery of the inner slope including model uncertanties . 108
6.12 Recovery of the shear amplitude including model uncertanties 109

List of Tables

1.1 Cosmological parameters from WMAP-5 6

3.1 Details of future lensing experiments 40

5.1 Equations for moments deconvolution up to order $n = 2$ . . 78
5.2 Correction terms for deweighting moments of order $n = i + j$ 79

6.1 Filter performance 103

Introduction

Curiosity has often been the engine which has driven women and men during centuries in the speculation about the universe, its origin and the laws regulating its evolution. This Thesis is driven by the same curiosity and tries to give a tiny little contribution to the understanding of the universe in which we find ourselves living. The knowledge of the fundamental principles regulating the cosmos, the way in which we look at Nature as scientists, have been shaped during centuries by people's mistakes and intuitions. One of the first fundamental intuition was that, in order to understand how the universe works, it is necessary to record astronomical phenomena. This idea can be traced back to Babylonian time ($1900 - 1200$ B.C.) when for the first time eclipses, positions of the planets and rise and setting of the Moon had been recorded. This approach, which we would call today *scientific*, strongly influenced the Hellenistic and Greek astronomy in later times. Greeks were the first trying to connect all the available observations of the universe to search for simple and universal laws. In particular the conviction was that a geometrical explanation of the universe was possible. For example Plato (and other Greek thinkers later on) attempted to reproduce the irregular observed motion of planets in the sky employing a combinations of uniform circular motions. Aristotle on the other hand thought that rotating spheres carrying the Moon, Sun, planets, and stars around a stationary Earth could have been the explanation for the observed motions. Plato's and Aristotle's ideas have been coded in the Almagest[1] by Ptolomey (100-175 A.D.) in the 150 A.D. All these ideas, which we know nowadays to be wrong, influenced specially the western science for almost thousand years.

A new era for cosmology started when Nasir al-Din al-Tusi (1201-1274) proposed a geometrical technique, called Tusi-couple, which generates linear motion from the sum of two circular motions. This was a very important achievement since allowed to abandon the equant[2] introduced by Ptolomy to explain the observed motion of planets. Copernicus (1473-1543) made use of this important result in 1543[3] when he formulated his heliocentric model. Galileo Galilei (1564-1642), Tycho Brahe (1546-1601) and Johannes Kepler (1571-1630) observations gave confirmations to this new vision of the universe and Newton (1642-1726) explained with his law of gravitation, either the laws that Kepler found about the motion of plan-

[1] Almagest's name comes from the Arabic name '*El-kitab-ul-majisti*' meaning '*The Great Compilation*'

[2] The equant was a point near the center of a planet's orbit which, if you were to stand there and watch, the centre of the planet's epicycle would always appear to move at the same speed.

[3] De revolutionibus orbium coelestium

ets, as well as the observed anomalies in the orbits caused by gravitational interaction between the planets.

Modern cosmology began in 1915 when Einstein published his theory of General Relativity. Some years later, in 1922 Friedmann derived a class of solutions from Einstein's equation under the assumption that the universe is homogeneous and isotropic. There were not any observations at that time supporting this assumption, and so it remained till 1964 when Penzias and Wilson (1965) discovered the a microwaves background radiation (CMB) with almost the same intensity, $\sim 3K$, in all directions in the sky. Surprisingly for almost all scientists in the twenties, Friedmann solutions were not describing a static universe, but were suggesting that the universe was expanding or contracting. Einstein realised that the only possibility to produce a static universe was to introduce a constant term into his equations, the so-called cosmological constant. However in the 1930s Slipher, Hubble and Humanson discovered, observing distant galaxies, that the recession velocity of the galaxies was proportional to their distance from the earth, meaning that the universe was expanding in a way compatible with Friedmann's solutions. For this reason the idea of a cosmological constant was quickly abandoned. Almost in the same years (Zwicky, 1933), studying galaxy clusters, found the first evidence of matter that interacts through gravitation but not through the electromagnetism, so it emits no light. Due to this property it has been called "dark matter". Current observations (e.g. Komatsu et al., 2009) show that almost 25% of the energy-density content of the universe is in this form, while only few percent is in the form of normal baryonic matter. In the 1990s two important results were achieved: WMAP showed that the universe is spatially flat with very high precision and there was the first evidence, coming from supernova studies (Riess et al., 1998), that the universe is accelerating. This was the reason to re-introduce the cosmological costant, which acting effectively as a term counteracting gravity, was able to explain the observed acceleration. Surprisingly enough it was discovered that the cosmological constant (or dark energy as it has been called later to include a larger class of cosmological models) constitutes 70% of the energy-density of the universe nowadays. The current model of the universe, built on the evidence we just briefly mentioned above, is usually called ΛCDM. Testing this model with high precision, and understanding the very nature of dark matter and dark energy, is one of the greatest challenge of modern cosmology.

Gravitational lensing has become in the last decade a competitive cosmological tool. Among other cosmological probes (CMB, supernovae, baryonic acoustic oscillations,...) it has the peculiarity of tracing directly

the matter distribution in the universe, without any assumptions on how light traces the underlying matter.

Significant lensing signals produced by the large scale structure of the universe (the so-called cosmic shear), have been detected in many studies (see Bacon et al., 2000; Kaiser, 2000; Benjamin et al., 2007, for recent examples), and evidence for accelerated expansion (Schrabback et al., 2010) has also been found.

Moreover it has been shown that lensing can constrain properties of dark matter halos and can be used to reconstruct the mass distribution of galaxy clusters, without any assumption on their dynamical status (Bartelmann and Schneider, 2001).

Gravitational lensing acts in practise as a coordinate transformation which modifies the shape of a distant object when matter is present along the line of sight. This transformation can be expressed, at low orders, in terms of spinorial field, the shear, the convergence, the $\mathcal{G}$-flexion and the $\mathcal{F}$-flexion, which are related to the derivatives of the gravitational potential. Each of these fields can be linked to a particular deformation of the object's shape.

Measuring those deformations, which are usually very tiny, is very challenging, given the fact that the intrinsic shape of the objects is unknown, blurring, noise and pixelation massively degrade the quality of the image and moreover the signal is convolved with the telescope's PSF. We will extensively discuss this aspect in **chapter 3**.

Different methods have been developed in the last 15 years for measuring the shear (e.g Kaiser et al., 1995; Refregier and Bacon, 2003; Miller et al., 2007), but none of them turned out to perform well enough in terms of precision and accuracy to be adopted by the whole community. Different testing programs (Heymans et al., 2006; Massey et al., 2007b; Bridle et al., 2010) have been recently set up in order to test the different pipelines. The main result was that almost all the current methods, if properly calibrated, perform well enough to exploit the current surveys. However it has been shown that the present accuracy is not sufficient to fully exploit the next-generation surveys (e.g. EUCLID[4], JDEM[5], DES[6], LSST[7]), in particular if the goal is to achieve percent accuracy on the dark energy equation of state (Amara and Réfrégier, 2008).

Particularly concerning are systematic biases in shear estimates, which do not vanish when averaged over a large ensemble of lensed galaxies. These biases often stem from assumptions made in the derivation or im-

[4] http://sci.esa.int/euclid
[5] http://jdem.gsfc.nasa.gov
[6] http://www.darkenergysurvey.org
[7] http://www.lsst.org

plementation of shear estimation methods, which do not hold in reality.

In this Thesis I investigate the so-called model-independent methods, which try to assume as little information as possible about the data to be analysed, in contrast with the model-dependent approaches which require assumptions on galaxy and PSF shapes.

The prototype of those methods is KSB (Kaiser et al., 1995) which forms a shear estimator from the second-order moments of lensed galaxy images. When doing so, it is not guaranteed that reasonable shear estimates can be achieved for each galaxy. Consequently, KSB requires a careful setup, which is adjusted to the characteristics of the data to be analyzed. Moreover KSB employs strong assumptions on the PSF shape, which are not necessarily fulfilled for a given telescope or observation (Kuijken, 1999a). I will show in **chapter 4** how KSB relies on several other assumptions concerning the relation between convolved and unconvolved ellipticity as well as the relation between ellipticity and shear, neither of which hold in practice. Furthermore I will discuss how improvements to the original KSB relations can be incorporated such that the shear estimates remain free of bias in a wider range of galactic and PSF parameters.

This analysis left some opened questions in particular about the PSF deconvolution.

I will present in **chapter 5** a novel model independent method for weak-lensing measurements (DEIMOS), which employs a mathematically exact deconvolution of the moments of the apparent brightness distribution of galaxies from the PSF, never done in practise in the KSB framework.

In the last four years there have been attempts to include flexion in the weak lensing analysis. Flexion is related to the third derivative of the potential, and is a direct tracer of local variations of shear ($\mathcal{G}$-flexion) and convergence ($\mathcal{F}$-flexion). Theoretical studies (Bacon et al. 2006, Goldberg et al. 2007) demonstrated that gravitational flexion might be able to provide information in the intermediate regime between pure weak-lensing (shear only) and strong lensing, allowing, for example, to improve cluster mass reconstruction. Moreover, being sensitive to local variations of shear and convergence, it can be used to detect substructures in galaxy clusters, which are undetectable using only shear measurements.

Measuring flexion is even more challenging than measuring shear, given the fact that higher moments of the surface-brightness distribution have to be measured. In the last four years there have been different attempts of extending the methods used for shear measurement to flexion. In particular extensions of shapelets and KSB have been proposed (Massey et al., 2007b; Okura et al., 2007).

I will present in **chapter 3** some theoretical calculations demonstrating

that measuring flexion is not only challenging from a practical point of view, but also the interpretation of the measured signal might be problematic closed to the centre of galaxy clusters. In fact, in regions where the shear is not small, the cross talk between shear and flexion can give rise to fields with exactly the same spin properties of the flexion fields. This leads to a possible contamination of the flexion field which has to be taken into account.

In **chapter 6** I will present a possible application of shear measurements for studying properties of galaxy clusters. In particular I will present two optimal filtering techniques which allow to constrain the inner slope of dark matter halos using weak lensing information. I discuss in details under which condition such methods can be applied and which are the accuracy we expect to achieve under realistic conditions.

Part of the work presented in this Thesis is contained in 3 published papers:

- **Viola M.**, Melchior P., Bartelmann M. 2010 *"Biases in, and corrections to, KSB shear measurements"*(arXiv:1006.2470, accepted for publication by *MNRAS*)[8]
- Melchior P., **Viola M.**, Schäfer B.M., Bartelmann M. 2010 *"Weak gravitational lensing with DEIMOS"*(arXiv:1008.1076, accepted for publication by *MNRAS*)[9]
- **Viola M.**, Maturi M., Bartelmann M. 2010 *"Constraints on the inner density profile of dark-matter haloes from weak gravitational lensing"* (*MNRAS* 403:859-869)[10]

[8]Part of chapter 3 and chapter 4
[9]Chapter 5
[10]Chapter 6

Leva dunque, lettore, a l'alte rote
meco la vista, dritto a quella parte
dove l'un moto e l'altro si percuote[0]

Dante (1265-1321) Paradiso X

1 Cosmology

This first chapter is a collection of the most important equations and ideas on which our understanding of the universe is based on. We will not give here a complete and extended overview, for which we refer to (Peacock and Murdin, 2002; Coles and Lucchin, 2002; Bartelmann, 2010), but we will simply introduce the main concepts that are necessary to understand lensing theory and its applications discussed in the rest of the Thesis.

1.1 General relativity and cosmological principle

General relativity is a description of gravity as a geometric property of the space time and up to now is the best description of gravitation in modern physics. The main idea on which the theory is based on may be summarized as follows: *"spacetime tells matter how to move and matter tells spacetime how to curve"*[1] In mathematical terms this is described by the so-called *Einstein field equation*:

$$R_{\mu\nu} - \frac{1}{2} g_{\mu\nu} R + \Lambda g_{\mu\nu} = K T_{\mu\nu} \tag{1.1}$$

where $R_{\mu\nu}$ is the Ricci tensor, R is the Ricci scalar, $g_{\mu\nu}$ is the metric of the spacetime, $T_{\mu\nu}$ is the energy-density tensor and K and Λ are two constants. The so-called Einstein tensor, $G_{\mu\nu} = R_{\mu\nu} - \frac{1}{2} g_{\mu\nu} R$, expresses the curvature of the spacetime, $T_{\mu\nu}$ its energy-density content and $\Lambda g_{\mu\nu}$ is a term proportional to the metric which can be arbitrarily added since it leaves unaffected the energy conservation law ($T^{\mu\nu}_{;\nu} = 0$). The value of K can be fixed requiring that, in the limit of weak gravitational field, the Newton law is recovered. This leads to:

$$K = \frac{8\pi G}{c^4} \tag{1.2}$$

[0] Then, reader, lift your eyes with me to see/the high wheels; gaze directly at that part/where the one motion strikes against the other

[1] This famous definition is by John Archibald Wheeler (1911-2008).

where $G = 6.673 \times 10^{-11}$ $m^3 kg^{-1} s^{-2}$ is the gravitational constant, $c = 299792458$ m/s is the speed of light .

The value of Λ, which is historically known as *cosmological constant*, has to be determined from observations. Setting $T_{\mu\nu} = 0$ in equation 1.1, $\Lambda g_{\mu\nu}$ can be interpreted as a source term for gravity corresponding to a vacuum energy density[2]. There are however other possible interpretations such that the source is not a density associated with the vacuum, but rather a new field, Dark Energy, whose energy density may evolve with time.

In order to apply Einstein equation for describing our universe it is necessary to make some assumptions about the metric of the spacetime and about the content of the universe.

Many models for the universe are based on the so called Cosmological principle, that is the universe is, on large scales (> 150 Mpc), homogeneous and isotropic in its spacial components. This very strong assumption, done for the first time by Friedmann in 1922 just for the sake of simplicity, is supported today by observations of the CMB (Penzias and Wilson, 1965; Smoot et al., 1992; Wu et al., 1999), and by the spatial distribution of galaxies (Abazajian et al., 2003; Colless et al., 2001). The most general metric for a space-time in which such a principle is valid is:

$$ds^2 \equiv g_{\mu\nu} dx^\mu dx^\nu = -(c dt)^2 + a(t)^2 \left[dw^2 + f_K^2(w)(d\vartheta^2 + \sin^2 \vartheta d\varphi^2) \right] \tag{1.3}$$

where w is a radial coordinate and

$$f_K(w) = \begin{cases} K^{-1/2} \sin(K^{1/2} w) & (K > 0) \\ w & (K = 0) \\ |K|^{-1/2} \sinh(|K|^{1/2} w) & (K < 0) \end{cases} \tag{1.4}$$

is a radial function which, to ensure homogeneity, can be either a trigonometric, linear or hyperbolic function of w according to the value of the *curvature* K. The *scale factor* $a(t)$ is responsible for the spatial stretching of the 4-dimensional space-time and can be only function of time, such that isotropy is not violated. The coordinates used here, in which the metric is free of cross term $dt dx^i$ and the space-part of the metric is proportional to a single function of the time, are called *comoving coordinates*. An observer

[2]Current cosmological observations gives the following value: $\Lambda \simeq (2 \times 10^{42} GeV)^2$, leading to an energy density $\rho_\Lambda = \Lambda m_{pl}^2 / 8\pi \simeq 10^{-47} \mathrm{GeV}^4$. However from quantum mechanics the vacuum energy density can be estimated as: $\rho_\Lambda \simeq 10^{74} \mathrm{GeV}^4$. Up to now there is no known natural way to derive the tiny cosmological constant used in cosmology from particle physics

who has $x^i = \text{const}$ is called *comoving*[3]. This metric is called *Friedmann-Lemaître-Robertson-Walker metric* and can be used to derive from Einstein equation a set of equations, describing the expansion of space filled by a homogeneous and isotropic fluid with pressure p and rest energy density ρc^2. They are called Friedmann cosmological equations and read as :

$$\ddot{a} = -\frac{4}{3}\pi G\left(\rho + 3\frac{p}{c^2}\right)a + \frac{\Lambda c^2}{3}a \tag{1.5}$$

$$\dot{a}^2 + Kc^2 = \frac{8}{3}\pi G\rho a^2 + \frac{\Lambda c^2}{3}a^2 \tag{1.6}$$

These equations cover all contributions to ρ, from matter, radiation and vacuum (or dark energy). Interestingly equation 1.6 reveals a connection between the density of the universe and its global geometry[4]:

$$\frac{K}{a^2} = \frac{1}{c^2}\left(\frac{\dot{a}}{a}\right)^2\left(\frac{\rho}{\rho_c} - 1\right) \tag{1.7}$$

where ρ_c is the *critical density*

$$\rho_c \equiv \frac{3}{8\pi G}\left(\frac{\dot{a}}{a}\right)^2 = \frac{3H^2}{8\pi G} \tag{1.8}$$

and it can be formally defined as the density the universe must have to be flat ($K = 0$). It's value today is $\rho_{0,c} = 1.88 \cdot 10^{-29}\ \mathrm{h^2 g/cm^3}$. Furthermore we defined the *Hubble parameter* as the relative expansion rate

$$H(t) \equiv \frac{\dot{a}}{a} \tag{1.9}$$

and its value at the present epoch is the so-called *Hubble constant* $H(t_0) = H_0$. It is parametrized as follow:

$$H_0 = h \cdot 100 \quad \mathrm{km \cdot s^{-1} \cdot Mpc^{-1}} \tag{1.10}$$

Measuring H_0 has always been very challenging, due to the difficulties of measuring distances on cosmological scales and that was the main reason which induced astronomers to parametrise it as shown in the equation above. The best measure of the Hubble constant

$$H_0 = 74.2 \pm 3.6 \quad \mathrm{km \cdot s^{-1} \cdot Mpc^{-1}} \tag{1.11}$$

[3]This class of freely falling observer are the one seeing the universe homogeneous and isotropic.

[4]Here we redefine the density such $\rho \longrightarrow \rho - \Lambda c^2/(8\pi G)$

has been done by Riess et al. (2009) from a new calibration of six Cepheid distances to nearby well-observed supernovae using the AdvancedCamera for Surveys (ACS) and the Near-Infrared Camera and Multi-Object Spectrometer (NICMOS) on the Hubble Space Telescope (HST).

From equation 1.7 we can immediately conclude that the space section of the spacetime will be closed, open or flat if the density parameter

$$\Omega_0 = \frac{\rho_0}{\rho_c} \tag{1.12}$$

defined as the ratio of the actual density ρ_0 and the critical density will be greater, smaller or equal to one.

1.2 The density of the universe

Friedmann equations are valid for a perfect fluid and can be solved assuming an equation of state relating the pressure to the energy density of the fluid:

$$p = w\rho c^2 \tag{1.13}$$

The case $w = 0$ represents a pressurless material (dust) but is a good approximation of any form of non relativistic fluid (e.g. dark matter). A fluid made by ultra-relativistic particle in thermal equilibrium has $w = 1/3$, while $w = -1$ correspond to the vacuum. Any fluid driving the acceleration of the universe ($\ddot{a} > 0$) must have $w(a) < -1/3$ as it is clear from equation 1.5.

We can combine equations 1.5 and 1.6 to yield:

$$\mathrm{d}(\rho(t)a^3(t)) = -3\frac{p(t)}{c^2}a^2(t)\mathrm{d}a \tag{1.14}$$

Solving together equations 1.13 and 1.14 we get that the density changes with the expansion as:

$$\rho(t)a^{3(1+w)} = \rho_0. \tag{1.15}$$

We can now specify this equation for the different component of the universe, and from equation 1.6, setting $K = 0$, we can compute the evolution of the expansion parameter with time in an universe dominated by a fluid with a given equation of state w:

- Matter dominated universe ($w = 0$) :

$$\rho_m = \rho_{m0}(1+z)^3 \quad a(t) \propto t^{2/3}. \tag{1.16}$$

- Radiation dominated universe ($w = 1/3$):

$$\rho_{\rm r} = \rho_{\rm r0}(1+z)^4 \quad a(t) \propto t^{1/2}. \tag{1.17}$$

- Vacuum dominated universe ($w = -1$):

$$\rho_\Lambda = \rho_{\Lambda 0} \quad a(t) \propto \exp(Ht). \tag{1.18}$$

In the previous equations z is the *redshift* and it is linked to the expansion parameter a in this way:

$$(1+z) = \frac{a(t_0)}{a(t)} \tag{1.19}$$

The redshift between two events A and B is also defined as the fractional change in wavelength:

$$z = \frac{\lambda_{\rm B} - \lambda_{\rm A}}{\lambda_{\rm A}} \tag{1.20}$$

Comparing the equations above we can conclude that the expansion of the universe has been dominated in its first phase by radiation (up to $z \sim 3400$), then by matter and ultimately by the vacuum (or any form of dark energy). Using equations 1.12, 1.16, 1.17 and 1.18, the second Friedmann equation (equation 1.6) can be written in the equivalent form:

$$H^2 = H_0^2\left[\frac{\Omega_{\rm r0}}{a^4} + \frac{\Omega_{\rm m0}}{a^3} + \Omega_{\Lambda 0} + \frac{1-\Omega_{\rm m0}-\Omega_{\rm r0}-\Omega_{\Lambda 0}}{a^2}\right] \equiv H_0^2 E^2(a) \tag{1.21}$$

where $\Omega_{\rm m0}$, $\Omega_{\rm r0}$, $\Omega_{\Lambda 0}$ are the present density parameter for matter (dark matter and baryonic matter), radiation, and cosmological constant respectively. $E(a)$ is the so-called *expansion function* and carries information about the expansion history. If instead of assuming that Λ is associated with the vacuum energy density, we assume that it is associated with some form of Dark Energy with a certain equation of state $\omega(a)$,the Hubble parameter reads as:

$$\begin{aligned} H^2 = H_0^2\Bigg[&\frac{\Omega_{\rm r0}}{a^4} + \frac{\Omega_{\rm m0}}{a^3} + \Omega_{\rm DE0}\exp\left(3\int_1^a \frac{{\rm d}a'}{a'}(1+w[a'])\right) + \\ &\frac{1-\Omega_{\rm m0}-\Omega_{\rm r0}-\Omega_{\rm DE0}}{a^2}\Bigg] \equiv H_0^2\tilde{E}^2(a) \end{aligned} \tag{1.22}$$

This equation follows from Einstein's equation assuming Friedmann-Lemaître-Robertson-Walker metric, which we assume to describe the universe at large scales. This means that the four parameters $\Omega_{\rm m0}$, $\Omega_{\rm r0}$,

Ω_{DE0} and H_0 can be used to fully characterised the universe. Determing their values with high precision is one of the biggest challenge in modern cosmology. Table 1.1, adapted from (Bartelmann, 2010), summarises the most recent result coming from WMAP data in combinations with Baryonic Acoustic Oscillation (Percival et al., 2007) and type Ia-Supernovae (Kowalski et al., 2008).

parameter	symbol	WMAP-5					
		alone			+ BAO + SNe		
CMB temperature	T_{CMB} 2.728	$\pm$	0.004 K		–		
total energy density	Ω_{tot}	1.099	$^{+}_{-}$	$^{0.100}_{0.085}$	1.0052	$\pm$	0.0064
matter density	Ω_{m0}	0.258	$\pm$	0.03	0.279	$\pm$	0.015
baryon density	Ω_{b0}	0.0441	$\pm$	0.0030	0.0462	$\pm$	0.0015
cosmological constant	$\Omega_{\Lambda 0}$	0.742	$\pm$	0.03	0.721	$\pm$	0.015
Hubble constant	h	0.719	$^{+}_{-}$	$^{0.026}_{0.027}$	0.701	$\pm$	0.013
power-spectrum normalisation	σ_8	0.796	$\pm$	0.036	0.817	$\pm$	0.026
age of the Universe in Gyr	t_0	13.69	$\pm$	0.13	13.73	$\pm$	0.12
decoupling redshift	z_{dec}	1087.9	$\pm$	1.2	1088.2	$\pm$	1.1
reionisation optical depth	τ	0.087	$\pm$	0.017	0.084	$\pm$	0.016
spectral index	n_s	0.963	$^{+}_{-}$	$^{0.014}_{0.015}$	0.960	$^{+}_{-}$	$^{0.014}_{0.013}$

Table 1.1: Cosmological parameters obtained from the 5-year data release of WMAP (Komatsu et al., 2009), without and with the additional constraints imposed by baryonic acoustic oscillations (Percival et al., 2007) and type-Ia supernovae (Kowalski et al., 2008). Note that spatial flatness ($K = 0$) was assumed in deriving most of these values. This table is adapted from Bartelmann (2010).

1.3 Distances

Defining a metric in the spacetime allows us to locally define the distance between two events in the spacetime. In an Euclidean spacetime the meaning of "distance" between two events is also independent on the observable used to evaluate it. This means, for example, that the distance calculated measuring the flux emitted by a source of known luminosity, has the same value of the distances calculated from the ratio between the source's actual size and the angular size of the source as viewed from earth. If the spacetime is not Euclidean this is not anymore true. In particular, looking at the metric (equation 1.3), it is clear that distances will depend on the expansion rate of the universe. We give here a summary of the most used distance definitions used in cosmology.

- **Proper distance** D_{prop}: is the distance measured by the travel time of a light ray which propagates from a source z_2 to an observer at

$z_1 < z_2$:

$$\begin{aligned} dD_{\text{prop}} &= -c\mathrm{d}t = -c\frac{\mathrm{d}a}{\dot{a}} = -c\frac{\mathrm{d}a}{aH(a)} \\ \Longrightarrow D_{\text{prop}}(z_1, z_2) &= \frac{c}{H_0}\int_{a_2}^{a_1}\frac{a'}{a'E(a')}\mathrm{d}a' \end{aligned} \tag{1.23}$$

- **Comoving distance** D_{com}: is the distance between two objects which remains constant with epoch if the two objects are moving with the cosmic flow:

$$\begin{aligned} dD_{\text{com}} &= -c\frac{\mathrm{d}t}{a} = -c\frac{\mathrm{d}a}{a\dot{a}} = -c\frac{\mathrm{d}a}{a^2H(a)} \\ \Longrightarrow D_{\text{prop}}(z_1, z_2) &= \frac{c}{H_0}\int_{a_2}^{a_1}\frac{(a')^2}{a'E(a')}\mathrm{d}a' \end{aligned} \tag{1.24}$$

- **Angular diameter distance** D_{A} : is defined as the ratio of an object's physical transverse size δA at z_2 to its angular size $\delta\omega$ as seen by an observer at z_1:

$$D_{\text{A}}(z_1, z_2) = \left(\frac{\delta A}{\delta\omega}\right)^{1/2} = a_2 f_K[w(z_1, z_2)] \tag{1.25}$$

  where in the last equality we made use of the fact that in a general spacetime:

$$\frac{\delta A}{4\pi a_2^2 f_K^2[w(z_1, z_2)]} = \frac{\delta\omega}{4\pi} \tag{1.26}$$

- **Luminosity distance** D_{L}: is defined by the relationship between flux F and bolometric luminosity L. It is possible to show that it is related to the angular diameter distance in the following way[5]:

$$D_{\text{L}}(z_1, z_2) = \left(\frac{L}{4\pi F}\right)^{1/2} = \left(\frac{a_1}{a_2}\right)^2 D_{\text{A}}(z_1, z_2) \tag{1.27}$$

A sketch of the different distances in a (spatially) flat and expanding universe is given in figure 1.1.

In the limit of small redshift (i.e. in the limit in which the spacetime can be considered almost euclidean) all the distances are the same:

$$D = \frac{cz}{H_0} \tag{1.28}$$

This relation, known as the *Hubble expansion law*, was empirically derived for the first time by Hubble (1929) observing that the velocity at which galaxies are receding from us is proportional to their distance from us. Historically it has been the first evidence for the expansion of the universe.

[5]This result is valid in an arbitrary space time as shown by Etherington (1933)

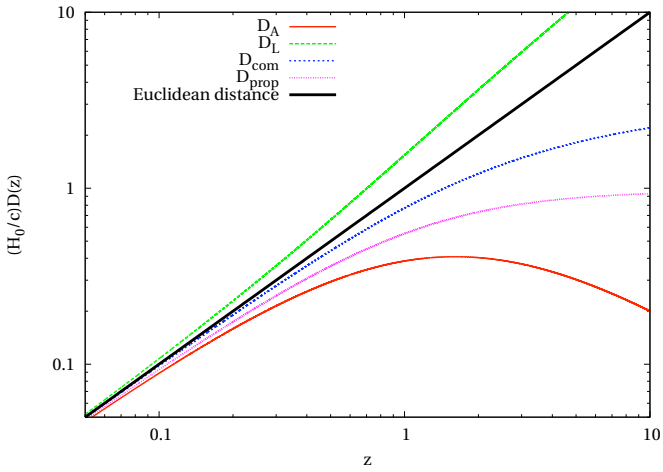

Figure 1.1: Distance measures in a (spatially) flat and expanding universe. *Red line* represents the angular diameter distance, *green line* the luminosity distance, *blu line* the comoving distance and *magenta line* the proper distance. In a perfect Euclidean spacetime all these distances would have the same redshift dependence (*black line*).

1.4 Structure formation

All the solutions of Einstein equation derived in the previous chapters are valid under the assumption that the universe is homogeneous and isotropic. This assumption is correct on large scale, as we discussed before, but it is obviously wrong on small scale where we see stars, galaxies, clusters of galaxies... In our current understanding of structure formation in the universe these inhomogeneities on small scales can be related with the fluctuations in the temperature field seen in the CMB. These primordial fluctuations grow during the evolution and eventually collapse forming clumps of matter, which throughout a series of mergers, give rise to what we call today galaxies or clusters of galaxies. We will concentrate in the following on the description of the linear growth of these primordial perturbations and we will briefly explain how their non linear evolution can be theoretically predicted.

1.4.1 Gravitational instability

A non-relativistic fluid can be described in Newtonian approximation through the continuity equation, the Euler equation and the Poisson equation:

$$\frac{\partial \rho}{\partial t} + \nabla \cdot \rho \bar{v} = 0 \tag{1.29}$$

$$\frac{\partial \bar{v}}{\partial t} + (\bar{v} \cdot \nabla)\bar{v} + \frac{1}{\rho}\nabla p + \nabla \phi = 0 \tag{1.30}$$

$$\nabla^2 \phi - 4\pi G \rho = 0 \tag{1.31}$$

where ρ is the fluid density, $\bar{v}$ is its velocity and p is the pressure. The system has a static solution $\rho = \rho_0$, $\bar{v} = 0$, $p = p_0$ and $\nabla\phi = 0$. The idea is now to perturb infinitesimally that solution and to study the first order solution of the perturbed system. We decompose the density contrast δ in plane-waves:

$$\delta(\bar{x}, a) \equiv \frac{\rho(\bar{x}, a) - \bar{\rho}}{\bar{\rho}} = \delta(a) \exp(-i\bar{k}\bar{x}) \tag{1.32}$$

Using this decomposition the perturbed continuity equation, Euler equation and Poisson equation can be brought into a single differential equation for the density contrast δ :

$$\ddot{\delta} + 2H\dot{\delta} + (v_s^2 k^2 - 4\pi G\bar{\rho})\delta = 0 \tag{1.33}$$

The cosmic expansion, expressed here by the Hubble function, acts as a damping term against the gravitational collapse. Looking at the term in brackets we can identify a typical length scale $\lambda_J = v_s\sqrt{\pi/G\rho_0}$, which is called the *Jeans length*. For wavelengths $\lambda > \lambda_J$ equation 1.33 admits two oscillating solution, while for $\lambda < \lambda_J$ the two solutions are stationary waves one growing and one decaying in time. In a dark matter dominated universe, Equation 1.33 reduces to:

$$\ddot{\delta} + 2H\dot{\delta} - 4\pi G\bar{\rho}\delta = 0 \tag{1.34}$$

which admits the growing solution $\delta \propto t^{2/3} = a$.

To compute the growth of fluctuation during the radiation dominated epoch, a fully relativistic treatment is required and we refer to Peacock (1999) for more details.

In general the growing mode, relevant for structure formation can be described by the growth factor:

$$D_+(a) \equiv \frac{\delta(a)}{\delta_0} \tag{1.35}$$

which is often parametrise as:

$$D_+ = \frac{G(a)}{G(1)} \tag{1.36}$$

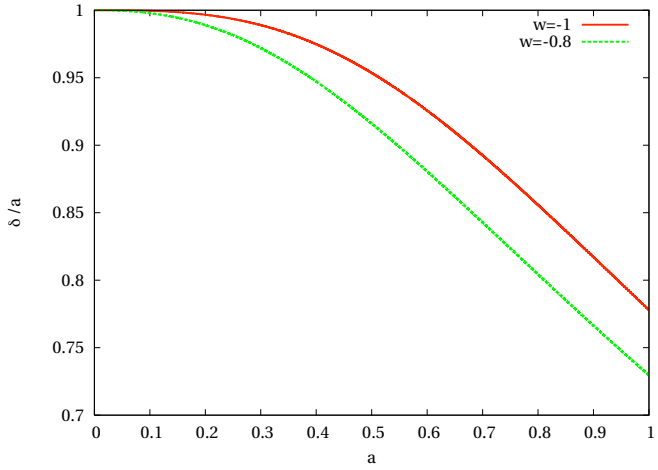

Figure 1.2: Growth factor of linear density perturbations plotted versus scale factor a for a ΛCDM model. Two different equations of state are used for dark energy: *red line* represent the case $w = -1$ (cosmological constant), while the *green line* shows the case of $w = -0.8$.

where

$$G(a) \equiv \Omega_{\rm m}\left[\Omega_{\rm m}^{4/7} - \Omega_\Lambda + \left(1+\frac{\Omega_{\rm m}}{2}\right)\left(1+\frac{\Omega_\Lambda}{70}\right)\right]^{-1} \tag{1.37}$$

is a fitting formula (Carroll et al., 1992). If instead of Λ cosmological constant some form of Dark Energy is assumed, the growth factor will have a different behaviour as a function of time, as it is shown in figure 1.2.

1.4.2 Power spectrum

Inflationary theories predict that the primordial density contrast field is almost a gaussian random field. Its mean vanishes by construction and therefore the field is fully characterized by its variance. The variance of the density contrast field in Fourier space is the so–called *power spectrum:*

$$\langle\hat{\delta}(\vec{k})\hat{\delta}^\star(\vec{k'})\rangle \equiv (2\pi)^3 P_\delta \delta_{\rm D}(\vec{k}-\vec{k'}) \tag{1.38}$$

In an isotropic universe, the spectrum of the density perturbation cannot have a preferred direction, and therefore it must be isotropic. Moreover we can assume that there are not preferred length-scale in the power-spectrum. This two conditions allow us to write the power spectrum in the form:

$$\langle\hat{\delta}(\vec{k})\hat{\delta}^\star(\vec{k'})\rangle = \langle|\delta_k|\rangle \propto k^n \tag{1.39}$$

The index n is the so-called *spectral index* and it indicates the balance between large and small-scale power. We showed before that in a matter dominated universe the perturbations grow like $\delta \propto a$. Analogously it is possible to show that in a radiation dominated universe they grow like $\delta \propto a^2$. We define the *epoch of equivalence* as the time when radiation density is equivalent to matter density. If a perturbation of (comoving) wavelength λ enters the horizon before the equivalence, its collapsing time-scale $t_{\rm coll}$ is longer than the expansion time-scale driven by radiation $t_{\rm exp}$:

$$t_{\rm coll} \sim \sqrt{G\rho_{\rm DM}} > \sqrt{G\rho_{\rm r}} \sim t_{\rm exp} \tag{1.40}$$

The result is that the perturbation gets frozen till after the equivalence. As a consequence smaller perturbations, which enter in the horizon before the equivalence, experience a suppression with respect to large perturbations. It is possible to show that the suppression factor is:

$$f_{\rm sup} = \left(\frac{a_{\rm enter}}{a_{\rm eq}}\right)^2 = \left(\frac{k_0}{k}\right)^2 \tag{1.41}$$

where $k_0 = d_{\rm H}^{-1}(a_{\rm eq})$ and in the last equality we used the fact that $k \propto 1/\lambda$ and

$$\lambda = d_{\rm H}(a_{\rm enter}) = \frac{c}{a_{\rm enter} H(a_{\rm enter})} \begin{cases} a_{\rm enter} & (a_{\rm enter} \ll a_{\rm eq}) \\ a_{\rm enter}^{1/2} & (a_{\rm eq} \ll a_{\rm enter} \ll 1) \end{cases} \tag{1.42}$$

In the previous equation $d_{\rm H}(a)$ is the *horizon size*. It is defined as the size of causally connected region in the universe and it is set by the distance that a photon can travel in a time t after the Big Bang. We can compute now the expected shape of the power spectrum. Let P_0 be the primordial power spectrum (immediately after the inflationary era). Since it is proportional to δ^2 it will grow as a^4 during the radiation epoch and as a^2 during the matter dominated era. At $a_{\rm enter}$ the spectrum has changed to:

$$P_{\rm enter}(k) = k^{-4} P_0(k) \tag{1.43}$$

As we specified before we want the power spectrum to be scale invariant, meaning $k^3 P_{\rm enter} = $ const. therefore we conclude that the primordial power spectrum should scale as $P_0(k) \propto k$. This scale invariant spectrum, with $n = 1$, is called the Harrison-Zeldovich spectrum (Harrison, 1970; Zeldovich, 1972). Because of the suppression of growth on small-scales, the final expression of the power spectrum reads:

$$P_\delta(k) \begin{cases} k & (k \ll k_0) \\ k^{-3} & (k \gg k_0) \end{cases} \tag{1.44}$$

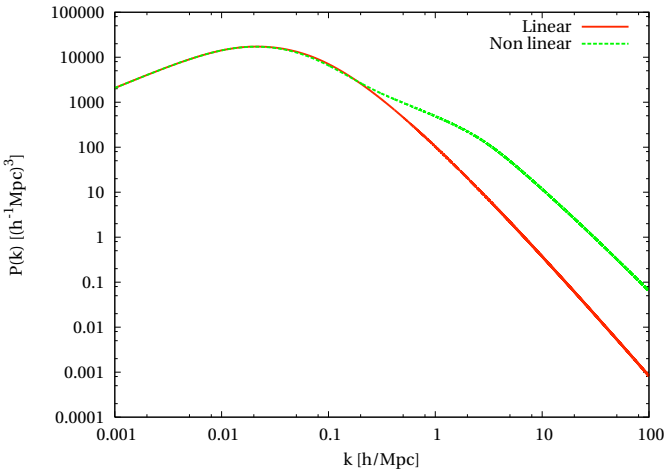

Figure 1.3: Linear (*red line*) and non-linear (*green line*) matter power spectrum for a standard ΛCDM cosmology. The non-linear power spectrum has been calculated following Peacock and Dodds (1996)

The equation above defines the shape of the linear power spectrum. Its amplitude is usually defined in term of the variance of the density contrast within spheres of radius R:

$$\sigma_R^2 = 4\pi \int \frac{k^2 \mathrm{d}k}{(2\pi)^3} W^2(kR) P(k) \tag{1.45}$$

where $W(kR)$ denotes a window function in Fourier space. Historically the amplitude is measured on scale of $R = 8\mathrm{h}^{-1}\mathrm{Mpc}$, since the variance computed on that scale from the distribution of galaxies is roughly 1. σ_8 is one of the crucial parameters in cosmology since it sets the time when structures in the universe start forming.

1.5 Non-linear structure formation

When the density contrast δ approaches unity, the evolution becomes non-linear and therefore equation 1.33 cannot be applied anymore to describe structure formation. During this phase, in which over-densities collapse under the action of gravity, there is a transfer of matter from large scales to small scales, which translates in a transfer of power in the density perturbation field towards smaller modes. The result is a deformation of the power spectrum at small scales as it shown in figure 1.3.

The evolution of the non–linear perturbations and the formation of structures in the universe can be followed using the so-called N–body simulations, in which dark matter (and gas in some cases) are approximated

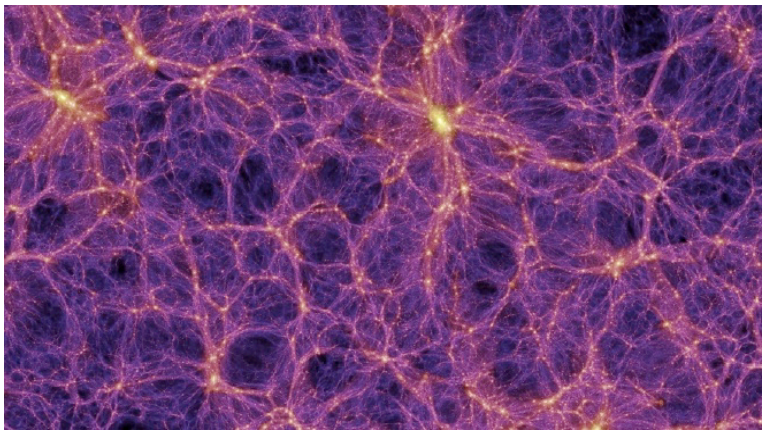

Figure 1.4: Snapshot from the Millennium Simulation (Springel et al., 2005) showing the so-called cosmic web. The clustering of dark matter happens along filaments at whom intersection sits dense clumps of matter, the galaxy clusters.

by a number N of point masses that move under the influence of their mutual gravitational forces. First numerical simulations attempts have been done in the seventies (Peebles, 1970; Press and Schechter, 1974; White, 1976) and in the last decades, thanks to the rapid growth of computer performance and the implementation of more sophisticated algorithm, many different groups simulated structure formation over cosmological time in increasingly larger volume and employing an increasingly higher number of particles (Springel, 2005; Gottlöber et al., 2006). All these studies confirmed that matter in the universe is clustered and that the clustering happens along filaments, at whose intersections sit highly non–linear bound structures, which we call galaxy clusters. A representation of the so–called *cosmic web* coming from cosmological simulations (Springel et al., 2005) can be seen in figure 1.4.

Moreover during last ten years, collisionless dynamics has also been coupled to gas dynamics (which effects are extremely important on small scales), allowing a more direct link to observable quantities. New algorithms for the collisionless system and the implementation of the gas dynamics into the simulation codes allow immense progress in the studies of the non-linear gravitational clustering of dark matter, the formation of galaxies and clusters of galaxies, the interactions of isolated galaxies, the evolution of the intergalactic gas....(Borgani et al., 2006)

Numerical simulations are nowadays a fundamental tool to compute the non-linear deviation of the power spectrum on small scale. There have been however attempts to compute analytically such deviations, for exam-

ple assuming that the two-point correlation function in the linear and non-linear regimes are simply related by a scaling relation (Hamilton, 2001). Generalisations of this work for different cosmological models have been possible using numerical simulations for calibrating the theoretical results. Analytic formulae describing the non-linear deviation of P (k) on small scales have been derived by Peacock and Dodds (1996) and Smith et al. (2003).

1.5.1 The structure of Dark matter halos

One of the prediction of ΛCDM model is the hierarchical growth of structures in the universe. This process is generally non-linear, as we discussed in the previous section, and the basic unit of non-linear structure formation are the so-called *dark matter halos*, which are highly concentrated clumps of dark matter forming via a series of mergers starting from small density perturbation in the early phase of the universe. Numerical simulations of non-linear structure formation in a broad class of cosmological models, even with different types of power spectra for the dark matter density fluctuations, reveal a typical shape for the density profile of dark matter halos (Navarro et al., 1997; Moore et al., 1998). As far as the numerical resolution allows this statement, the density profile begins with at least a mild singularity in the core, then falls off with a relatively flat slope out to a characteristic radius where it gently steepens towards an asymptotic behaviour $\rho \propto r^{-3}$ far away from the core:

$$\rho(r) = \frac{\rho_{\rm s}}{(r/r_{\rm s})^{\alpha}(1 + r/r_{\rm s})^{3-\alpha}} \tag{1.46}$$

Here $r_{\rm s}$ is the *scale radius*, α the *inner slope* and $\rho_{\rm s}$ *the scale density* defined as:

$$\rho_{\rm s} = \rho_{\rm crit}(z)\frac{200(3-\alpha)(r_{200}/r_{\rm s})}{3{}_1F_2(3-\alpha, 3-\alpha, 4-\alpha, -r_{200}/r_{\rm s})}\,, \tag{1.47}$$

where ${}_1F_2(a, b, c, z)$ is a hypergeometric function and r_{200} is the radius enclosing 200 times the critical density of the universe $\rho_{\rm crit}$. The halo concentration is defined as

$$c_{200} = \frac{r_{200}}{r_{\rm s}}. \tag{1.48}$$

Following Keeton and Madau (2001) we interpret the scale radius as the radius where the density profile reaches slope -2, i.e. $\mathrm{d}\ln\rho/\mathrm{d}\ln r = -2$. For the profile of equation 1.46

$$r_{-2} = r_{\rm s}(2-\alpha) \tag{1.49}$$

and thus

$$c_{-2} = \frac{r_{200}}{r_{-2}} = \frac{1}{2-\alpha}c_{200}. \tag{1.50}$$

We note here that the density profile presented in equation 1.46 is just a fitting formula. Up to now there is no theoretical argument justifying that particular form. The value of the inner slope α is still a matter of debate both theoretically and observationally. We will discuss in chapter 6 how it is possible to measure it using weak lensing data. For $\alpha = 1$ these formulae reduce to the so-called NFW profile (Navarro et al., 1997). The profile is fully characterized when the mass, the redshift, the concentration and the inner slope of the halo are specified. However not all of these parameters are independent. Numerical simulations show that it is possible to define fitting formulae relating the concentration with the mass and the redshift of the halo:

$$c_{\rm vir} = \frac{c_0}{1+z}\left(\frac{M}{M_0}\right)^{-\beta} \tag{1.51}$$

with $\beta \sim 0.1$. The normalization depends on the non-linear mass, which is the mass within spheres in which the rms fluctuation in the linear regime is 1.68. We refer to Eke et al. (2001), Bullock et al. (2001a) and Neto et al. (2007) for a more detailed treatment of the mass-concentration relation. In numerical simulations was also found that for a fixed value of mass and redshift, the concentration approximately follows a log-normal distribution

$$p(c)\mathrm{d}c = \frac{1}{\sqrt{2\pi}\sigma_{\rm c} c}\exp\left[-\frac{(\ln c - \ln \bar{c})^2}{2\sigma_{\rm c}^2}\right]\mathrm{d}\ln c \tag{1.52}$$

where $\sigma_{\rm c}$ is the 1-σ deviation of $\Delta(\ln c) \simeq 0.2$ (Navarro et al., 1997; Bullock et al., 2001a).

Tu dubbi, e hai voler che si ricerna
in sì aperta e 'n sì distesa lingua
lo dicer mio, ch'al tuo sentir si sterna[0]
Dante (1265-1321) Paradiso XI

2

Weak gravitational lensing

The deflection of light rays by structures in the universe is called "gravitational lensing". The earliest concept of gravitational lensing can be traced back to Newton in 1704. First calculation had been done by Cavendish around 1784 under the hypothesis that light was made by particles which were experiencing the force of gravity. He was the first one calculating the deflection of light induced by a body of a certain mass. However was Johan Soldner in 1801 who published first the calculation about the deflection of light by the sun. At the same result arrived also Einstein in 1911, but based on the equivalence principle[1] alone. However, he noted in 1915 while he was completing General Relativity, that his (and thus Soldner's) 1911-result was only half of the correct value (Will, 2006). The first observation of light deflection was performed in 1919 during a solar eclipse by Sir Arthur Eddington observing the change in position of stars as they passed near the Sun on the celestial sphere. Despite the big uncertainties in the measurement the result seemed to confirm the deflection angle predicted by Einstein from general relativity. However only in the 1960s, using radio observations, was possible to clearly discriminate between the Newtonian result and Einstein result. The first gravitationally lensed object (the quasar SBS0957 + 561) was discovered only in 1979 by Walsh et al. (1979) and collaborators using the Kitt Peak National Observatory 2.1 meter telescope. Some years later there was the first publication by Lynds and Petrosian (1986) about giant arcs (strong gravitational lensing) in a survey of galaxy clusters, but was only in 1987 when Soucail et al. (1987) presented data of a blue ring-like structure in Abell 370 and Paczynski (1987) proposed a gravitational lensing interpretation. In figure 2.1 we show a more recent image of a massive cluster of galaxies done by the Hubble Space Telescope (HST hereafter), in which

[0] You are in doubt; you want an explanation/in language that is open and expanded/so clear that it contents your understanding

[1] All inertial and freely-falling reference frames are equivalent, and there is no (local) experiment that can distinguish them.

Figure 2.1: Hubble Space Telescope image of Abell 2218, a massive cluster of galaxies. Many strong lensing features, such as arcs and multiple images can be seen. Credit: NASA/ESA.

many strong lensing features, such as giant arcs and multiple images can be seen.

The first cluster weak lensing analysis was done by Tyson et al. (1990). They detected for the first time a systematic alligment of $20-60$ faint background galaxies centred on foreground galaxy clusters of high velocity dispersion. Only in 2000 several groups detected for the first time the light deflection produced by the large scale structure in the universe (cosmic shear) opening up the possibility to use weak gravitational lensing to constrain cosmological parameters (Wittman et al., 2000; Van Waerbeke et al., 2000; Bacon et al., 2000; Kaiser, 2000).

This phenomenon constitutes nowadays an extraordinary tool in astrophysics, since it allows to infer properties of the matter which induces the deflection independently on its dynamical status. For example it is possible to trace directly the matter distribution in the universe, or to study the properties of dark matter halos without any assumptions on how light does trace the underlying matter.

Gravitational lensing however, even if it has a simple and nice mathematical treatment in the framework of general relativity, poses a lot of observational challenges since measuring the deflection of light normally means measuring tiny distortion in the shape of faint background galaxies. We will discuss this crucial point in the following chapter.

2.1 Weak lensing basics

We present here a summary of the main concepts and equations which are basic for gravitational lensing. In particular we concentrate on weak grav-

itational lensing, meaning the regime in which the distortion produced by any intervening structure is small. For a complete overview on weak lensing we refer to Bartelmann and Schneider (2001).

2.1.1 Deflection angle

From general relativity and geometrical optics in Einstein-Maxwell theory we know that light rays propagate in the space-time along null geodesics [2]; massive objects produce distortion of the space-time such that the geodesics are not any longer straight lines as they would be in a flat (euclidean) space. If the light ray does not propagate through the strong gravitational field close to the object's horizon, general relativity predicts that the difference between the actual geodesic and the geodesic the light would follow in a flat space-time is given by:

$$\hat{\vec{\alpha}} = \frac{4GM}{c^2}\frac{\vec{\xi}}{|\vec{\xi}|^2} \tag{2.1}$$

which is usually called *deflection angle*. Here M is the mass of the object bending the space-time, G is the gravitational constant, c the speed of light and $\vec{\xi}$ is the impact vector, orthogonal to the geodesic, which denotes the distance from the lens. In reality any light ray gets deflected by many massive objects. Since the gravitational field can be considered weak the field equation of general relativity can be linearised and therefore the total deflection angle is just the vectorial sum of the deflection angles caused by the single objects. In the continuum limit the sum becomes an integral over the density field ρ along the line of sight. Furthermore in the limit of small deflection angles we can make use of the Born approximation, meaning we can approximate the potential along the deflected geodesic with the potential along the undeflected geodesic:

$$\hat{\vec{\alpha}} = \frac{4G}{c^2}\int \mathrm{d}z \int \mathrm{d}^2\xi' \frac{(\vec{\xi}-\vec{\xi}')\rho(\vec{\xi}',z)}{|\vec{\xi}-\vec{\xi}'|^2} \tag{2.2}$$

If the distances between the observer, the lens, the source are much larger than the dimension of the lens, we can use the thin screen approximation defining a projected mass density:

$$\Sigma(\vec{\xi}) = \int \rho(\vec{\xi},z)\mathrm{d}z \tag{2.3}$$

[2] If an affine connection can be defined on the manifold, *geodesic* are curves whose tangent vectors remain parallel if they are transported along it.

which is the mass density projected onto a plane perpendicular to the line of sight. Using this definition the deflection angle becomes:

$$\hat{\vec{\alpha}} = \frac{4G}{c^2} \int \mathrm{d}^2\vec{\xi}' \Sigma(\vec{\xi}') \frac{(\vec{\xi} - \vec{\xi}')}{|\vec{\xi} - \vec{\xi}'|^2} \tag{2.4}$$

2.1.2 Lens equation

Making use of the expression calculated for the deflection angle we can now relate the true position of the source (η) to its observed position in the sky (ξ). The situation in sketched in figure 3.2 from which we can read:

$$\vec{\eta} = \frac{D_\mathrm{s}}{D_\mathrm{d}}\vec{\xi} - D_\mathrm{ds}\hat{\vec{\alpha}}(\vec{\xi}) \tag{2.5}$$

where $D_{\mathrm{d,s,ds}}$ are the angular-diameter distances between the observer and the lens, the observer and the source, and the lens and the source, respectively. We assume here that the extent of the lens is much smaller than both D_ds and D_s so that the light rays can be approximated by two straight lines with a kink near the deflector. We can write the last equation in a more convenient way, introducing angular coordinates by $\vec{\eta} = D_\mathrm{s}\vec{\beta}$ and $\vec{\xi} = D_\mathrm{d}\vec{\theta}$:

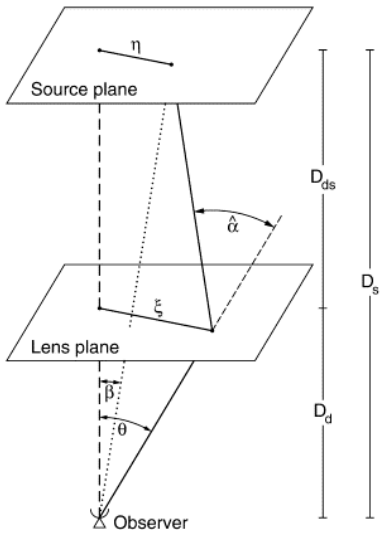

Figure 2.2: Sketch of a typical lensing configuration from Bartelmann and Schneider (2001)

$$\vec{\beta} = \vec{\theta} - \frac{D_\mathrm{ds}}{D_\mathrm{s}}\hat{\vec{\alpha}}(D_\mathrm{d}\vec{\theta}) \equiv \vec{\theta} - \vec{\alpha}(\vec{\theta}) \tag{2.6}$$

where we defined the scaled deflection angle $\vec{\alpha}(\vec{\theta})$. This fundamental equation, relating the true position $\vec{\beta}$ of a source and its observed position $\vec{\theta}$ is non-linear and admits in general more than one solution. This means that a source at a given position $\vec{\beta}$ can have multiple observed images. A sufficient, but not necessary condition for this to happen (Subramanian and Cowling, 1986), is that the dimensionless surface mass density, which we call *convergence*

$$\kappa(\vec{\theta}) = \frac{\Sigma(D_\mathrm{s}\vec{\theta})}{\Sigma_\mathrm{cr}} \tag{2.7}$$

is greater than unity. We defined here the *critical surface mass density* as :

$$\Sigma_{\rm cr} = \frac{c^2}{4\pi G}\frac{D_{\rm s}}{D_{\rm d}D_{\rm ds}} \tag{2.8}$$

We can use $\Sigma_{\rm cr}$ as a discriminant between the strong $\Sigma_{\rm cr} > 1$ and weak lenses $\Sigma_{\rm cr} < 1$. In terms of κ the scaled deflection angle reads:

$$\vec{\alpha}(\vec{\theta}) = \frac{1}{\pi}\int {\rm d}^2\theta' \kappa(\vec{\theta}') \ln|\vec{\theta} - \vec{\theta}'| \tag{2.9}$$

This expression suggests that the scaled deflection angle can be written as the gradient of the deflection potential

$$\Psi(\vec{\theta}) = \frac{1}{\pi}\int {\rm d}^2\theta' \Sigma(\vec{\theta}') \ln|\vec{\theta} - \vec{\theta}'|, \tag{2.10}$$

as $\vec{\alpha} = \nabla\Psi$.

2.1.3 Local distortions

Suppose now to have an extended source (e.g a galaxy) which we observe at some position $\vec{\theta}$ in the sky. In presence of matter along the line of the sight we expect that the shape of the observed image will differ from the shape of the source, since the rays are deflected differentially. If we assume that the source is much smaller with respect to the scale on which the lens properties change we can locally expand the lens equation and truncate the expansion at low orders:

$$\beta_i \simeq \theta_i - \Psi_{,ij}\theta^j - \frac{1}{2}\Psi_{,ijk}\theta^j\theta^k \tag{2.11}$$

In many weak lensing applications the expansion of the lens equation can be safely truncated at first order. However if the sources are large or in regions of the lens plane where the potential varies rapidly (e.g. in proximity of a galaxy cluster), the second order terms become important. The linearisation of the lens equation fails completely close to the centre of galaxy clusters, where giant arcs occurs. In this case the full lens equation has to be studied. The occurrence of giant arcs can be used as a visual distinction between the weak and the strong lensing regime.

It is convenient to introduce at this point a complex notation for the relevant lensing quantities which will appear in the following. We introduce the complex mapping:

$$\begin{pmatrix} v_1 \\ v_2 \end{pmatrix} \longrightarrow v_1 + iv_2 = z \tag{2.12}$$

In polar form z reads as:

$$z = \sqrt{v_1^2 + v_2^2} e^{i\phi} \quad \text{with} \quad \phi = \arctan \frac{v_2}{v_1} \tag{2.13}$$

We start defining a complex gradient operator Newman and Penrose (1962); Bacon et al. (2006):

$$\partial = \frac{\partial}{\theta_1} + i\frac{\partial}{\theta_2} \equiv \partial_1 + i\partial_2 \tag{2.14}$$

which in polar coordinates it has the form

$$\partial = e^{i\phi}\left(\frac{\partial}{\partial r} + \frac{i}{r}\frac{\partial}{\partial \theta}\right) \tag{2.15}$$

This representation shows clearly that when ∂ is applied to a spin s quantity [3] it raises its spin by one. Analogously, ∂^* lowers the spin by one. Applying now this operator one time to the deflection potential we can generate the deflection angle:

$$\alpha = \partial\Psi \tag{2.16}$$

which is a spin-1 field. Applying it twice we can generate the *convergence* (spin-0)

$$\kappa = \frac{1}{2}\partial\partial^*\Psi = \frac{1}{2}(\Psi_{,11} + \Psi_{,22}) \tag{2.17}$$

and the *shear* (spin-2)

$$\gamma = \frac{1}{2}\partial\partial\Psi = \frac{1}{2}[(\Psi_{,11} - \Psi_{,22}) + 2i\Psi_{,12}] \tag{2.18}$$

while applying it three times is it possible to generate the so-called $\mathcal{F}$-*flexion* (spin-1)

$$\mathcal{F} = \frac{1}{2}\partial\partial\partial^*\Psi = \frac{1}{2}[(\Psi_{,111} + \Psi_{,122}) + i(\Psi_{,112} + \Psi_{,222})] \tag{2.19}$$

and the $\mathcal{G}$-*flexion* (spin-3)

$$\mathcal{G} = \frac{1}{2}\partial\partial\partial\Psi = \frac{1}{2}[(\Psi_{,111} - 3\Psi_{,122}) + i(3\Psi_{,112} + \Psi_{,222})] \tag{2.20}$$

We can now use these new fields to re-write equation 2.11:

$$\beta \simeq (1-\kappa)\theta - \gamma\theta^* - \frac{1}{4}\mathcal{F}^*\theta^2 - \frac{1}{2}\mathcal{F}\theta\theta^* - \frac{1}{4}\mathcal{G}(\theta^*)^2 \tag{2.21}$$

[3] We say that a quantity has spin s if it is invariant under a rotation of the Cartesian coordinate frame by a rotation angle $\phi = 2\pi/s$ and $s \in [1, 2, ...]$. Vectors are spin-1 quantities.

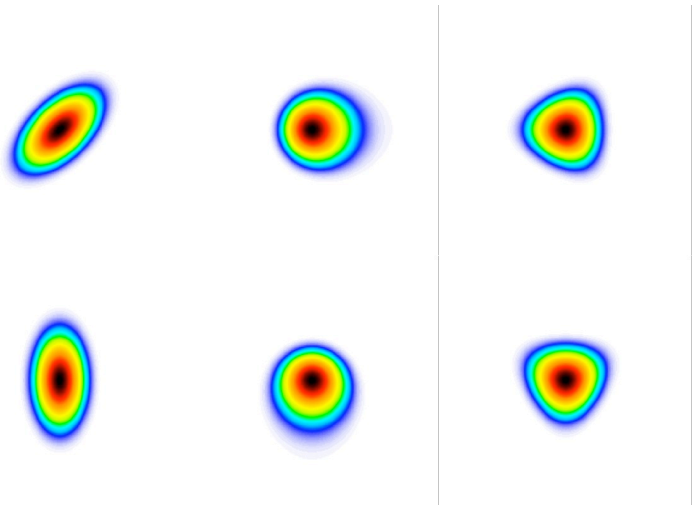

Figure 2.3: Effect of shear and flexion on a circular source. The image is taken from Bartelmann (2010, in preparation).

This equation relates the true and the observed position in terms of quantities with well defined spin properties and linked to the deflection potential. In the case of an extended source the shape will be determined by solving the lens equation for each point within the source. One interesting aspect of Liouville's theorem is that lensing conserves the total number of photons emmited by the source. Hence the surface-brightness in the lens plane , I, and in source plane I^s are related:

$$I(\vec{\theta}) = I^s[\vec{\beta}(\vec{\theta})] \tag{2.22}$$

This equation, together with equation 2.21, tells how the global shape of a source gets modified by lensing. For example circular sources, if flexion can be neglected, will appear elliptical. The effect of flexion on a circular source is to produce an arclet-shape, as can be seen in figure 2.3. The bottom line here is that each of the fields we previously defined, is related to a peculiar deformation of the object's shape. Measuring these deformations permits to have information on shear and flexion. How this is done in practise will be discussed in the next chapter.

Another interesting effect is the so-called *magnification*. It is defined as the ratio between the flux computed in the lens plane and the flux computed in the image plane. From 2.22 we have:

$$\mu = \frac{1}{\det A} \tag{2.23}$$

where $\det A$ is the jacobian determinant of the lens equation. Its first order

expansion around the origin reads as:

$$\det A \simeq (1-\kappa)^2 - \gamma\gamma^\star - \theta\left[(1-\kappa)\mathcal{F}^\star + \frac{\gamma^\star\mathcal{F} + \gamma\mathcal{G}^\star}{2}\right] - \theta^\star\left[(1-\kappa)\mathcal{F} + \frac{\gamma^\star\mathcal{G} + \gamma\mathcal{F}^\star}{2}\right] + \mathcal{O}(\theta^2) \tag{2.24}$$

2.2 Lens model

In the previous section we showed how the deflection angle is linked to the density profile of the lens. If the lens is axially symmetric (i.e. the surface brightness is independent on the position angle with respect to the lens centre), the scale deflection angle has the following form:

$$\alpha(x) = \frac{M(\xi_0 x)}{\pi\xi_0^2\Sigma_{\rm cr}}\frac{1}{x} \equiv \frac{m(x)}{x} \tag{2.25}$$

where $m(x)$ represents a dimensionless mass inside a radius x. Note that:

$$m(x) = 2\int_0^x \mathrm{d}yy\kappa(y) \tag{2.26}$$

where $\kappa(y)$ is defined in equation 2.7. For an axially symmetric lens the lens equation has a one-dimensional form, and using the previous equation it reads as:

$$y = x - \frac{m(x)}{x} \tag{2.27}$$

This form suggests that we can express all the lensing fields in terms of $m(x)$. Recalling the definition of shear and convergence we gave in the previous section, it is easy to show that:

$$\kappa(x) = \frac{1}{2x}\frac{dm(x)}{x}, \tag{2.28}$$

$$\gamma(x) = \frac{m(x)}{x^2} - \kappa(x) = \bar{\kappa}(x) - \kappa(x) \tag{2.29}$$

where $\bar{\kappa}(x)$ is the mean surface mass density inside a circle of radius x centred on the lens.

2.2.1 NFW lensing properties

We can now specialise the equation we presented in the previous section for a NFW profile. If we take $\xi_0 = r_{\rm s}$, the density profile, defined in equation 1.46, implies for the inner slope $\alpha = 1$ the surface mass density

$$\Sigma(x) = \frac{2\rho_{\rm s} r_{\rm s}}{x^2 - 1} f(x) \tag{2.30}$$

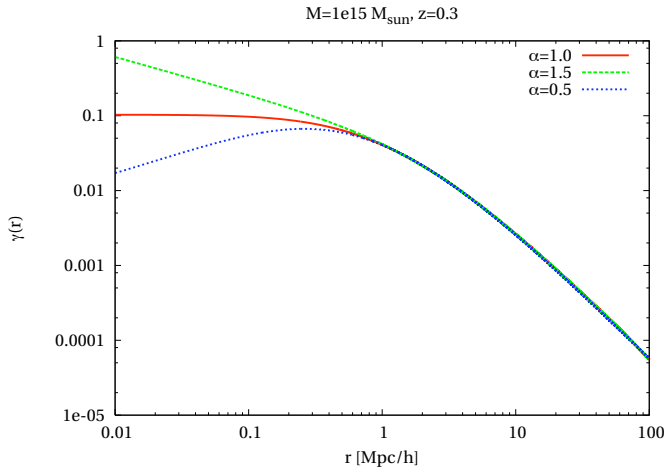

Figure 2.4: Shear profile of a generalized NFW halo for three different values of α. The case $\alpha = 1$ corresponds to the usual NFW profile. Note the strong dependence on the inner slope.

with

$$f(x) = \begin{cases} 1 - \frac{2}{\sqrt{x^2-1}} \arctan \sqrt{\frac{x-1}{x+1}} & (x > 1) \\ 1 - \frac{2}{\sqrt{1-x^2}} \operatorname{arctanh} \sqrt{\frac{1-x}{1+x}} & (x < 1) \\ 0 & (x = 1) \end{cases} \tag{2.31}$$

as shown by Bartelmann (1996). Defining $\kappa_s = \rho_s r_s \Sigma_{cr}^{-1}$ the convergence reads as:

$$\kappa(x) = 2\kappa_s \frac{f(x)}{x^2 - 1} \tag{2.32}$$

and from equation 2.26 we can compute:

$$m(x) = 4\kappa_s g(x) \tag{2.33}$$

where

$$g(x) = \ln \frac{x}{2} + \begin{cases} \frac{2}{\sqrt{x^2-1}} \arctan \sqrt{\frac{x-1}{x+1}} & (x > 1) \\ \frac{2}{\sqrt{1-x^2}} \operatorname{arctanh} \sqrt{\frac{1-x}{1+x}} & (x < 1) \\ 1 & (x = 1) \end{cases} \tag{2.34}$$

The shear can be then easily computed combining equations 2.29, 2.32 and 2.33.

If $\alpha \neq 1$ it is generally not possible to find an analytic expression for the shear profile and therefore equation 2.29 has to be computed numerically. We show in figure 2.4 the shear profile for three values of α (0.5,1.0,1.5). The inner shear profile depends sensitively on the inner slope α.

The shear profile depends on the two parameters of the density profile, of which the concentration depends mildly on the halo redshift. An additional and stronger dependence on halo and source redshifts is introduced through the geometry of the lens system.

2.3 Cosmic shear

Up to this point we discussed how a bundle of light rays gets deflected by the presence of a single mass along the line of sight. In order to derive the deflection angle we made use of the thin lens approximation. However in reality any light ray gets deflected by any density perturbation along the line of sight. We summarise here how is possible to generalise the results derived for a single mass to the case in which the deflector is given by the large scale structures in the universe. First of all the thin lens approximation used before cannot be employed since structures can be elongated along the line of sight. However in the weak lensing regime the deflection angle can be derived assuming that the gravitational potential is slowly varying everywhere. Under this assumption it is possible to show that the deflection angle

$$\vec{\alpha}(\vec{\theta}) = \frac{2}{c^2}\int_0^w \mathrm{d}w' \frac{f_K(w-w')}{f_K(w)} \nabla_\perp \Phi[f_K(w')\vec{\theta}, w'] \tag{2.35}$$

is given by a weighted integral of the perpendicular (to the line of sight) potential gradient, where the weight is given by the ratio of comoving angular-diameter distances, from the deflecting potential to the source, $f_K(w-w')$, and from the observer to the source, $f_K(w)$. This result is a direct consequence of the geodesic equation in general relativity. In exact analogy with the calculation done in the thin lens approximation, it is possible to define an *effective convergence*:

$$\kappa_{\mathrm{eff}}(\vec{\theta}, w) = \frac{1}{2}\nabla\vec{\alpha}(\vec{\theta}, w) = \frac{3H_0^2\Omega_{\mathrm{m}}}{2c^2}\int_0^{w_H} \mathrm{d}w \bar{W}(w) f_K(w) \frac{\delta[f_K(w)\vec{\theta}, w]}{a(w)} \tag{2.36}$$

where we used Poisson equation to replace the Laplacian of the potential by the density contrast:

$$\triangle\,\Phi = \frac{3H^2\Omega_{\mathrm{m}}}{2a}\delta. \tag{2.37}$$

The weighting function

$$\bar{W} \equiv \int_w^{w_H} \mathrm{d}w' n(w') \frac{f_K(w-w')}{f_K(w)} \tag{2.38}$$

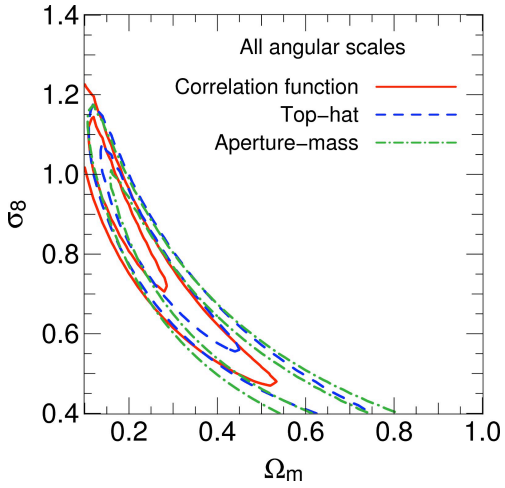

Figure 2.5: Likelihood contour $(1, 2\sigma)$ for $\Omega_{\rm m}$ and σ_8 using different shear correlation functions between 1 and 230 arcmin from Fu et al. (2008)

takes into account that the sources might have a redshift distribution $n(w)$. We refer to Bartelmann and Schneider (2001) for a derivation of the above equation.

Eventually we are interested in the statistical properties of the effective convergence, which we can describe using its power spectrum. Using Limber's equation [4] we can express the convergence power spectrum in terms of the matter density power spectrum:

$$P_\kappa^{kl}(l) = \frac{9H_0^4\Omega_{\rm m}^2}{4c^4}\int_0^{w_H} {\rm d}w \frac{\bar{W}^k(w)\bar{W}^l(w)}{a^2 w} P_\delta\left(\frac{l}{f_K(w)}, w\right) \tag{2.39}$$

We make explicit here that the power spectrum can be computed considering one single redshift distribution for the galaxies $k = l$, or can be computed after dividing the galaxy population in two or more bins with redshift distribution $n_k(w)$ and $n_l(w)$. We discuss this second approach, known as lensing tomography, in the next section. It is worth to note already at this point that equation 2.39 has been derived employing Limber's approximation, which requires that the redshift distribution must be sufficiently wide to encompass many wavelenghts of the relevant fluctuation $2\pi/k_l$ along the line of sight, where $k_l = lH_0/D_{\rm A}(w)$ is the wavenumber that projects onto the angular scale at distance w (Hu, 1999; Simon, 2007).

Typically weak lensing probes scales in the range $\theta \in [1, 100]$ arcmin, which, assuming that the sources are at redshift 1, corresponds roughly

[4] It's an approximation introduced by Limber (1953) used to relate any projected correlation function to the spatial, three dimensional correlation function.

to $k \in [0.2, 20]$ hMpc^{-1}. In this range, as can be seen from figure 1.3, deviations from linearity in the power spectrum become important and they turn to be dominant at scale $\theta < 10'$ (or $k > 2$ hMpc^{-1}).

Analogously to the effective convergence an *effective shear* can be defined and it is possible to show that the shear power spectrum reads exactly as the convergence power spectrum. The power spectrum, defined in equation 2.39, is sensitive to cosmology in three different ways: explicitly in the pre-factor $\Omega_{\rm m}^2$, in the geometrical factor $f(w - w')/f(w)$, and in the $3D$ matter power spectrum P_δ and in its evolution with time. It is sensitive in particular to the normalization of the power spectrum σ_8 in combination with $\Omega_{\rm m}$ as can be seen in figure 2.5 (Fu et al., 2008). Since weak lensing probes the non linear part of the power spectrum it is crucial to have reliable and precise theoretical prediction on the non linear power spectrum in order to extract sensible cosmological information.

A very interesting and promising approach to break the degeneracy between σ_8 and $\Omega_{\rm m}$ using weak-lensing, comes from the measurement of cosmic magnification on galaxy by galaxy base, exploiting the fact that the magnification power-spectrum scales with $\Omega_{\rm m}$ and not with $\Omega_{\rm m}^2$ as the shear power-spectrum (van Waerbeke, 2010). In figure 2.6 are shown cosmological parameter constraints from shear and magnification exploiting a 1500 sq. deg. survey.

In practical applications the measured quantity is not the power spectrum but the two-point shear correlation functions. They are defined by considering pairs of positions θ and $\theta + {\rm d}\theta$, and defining the tangential and cross-component of the shear at position θ for this pair as

$$\gamma_{\rm t} = -\,{\rm Re}(\gamma e^{-2i\phi}) \quad \gamma_\times = -\,{\rm Im}(\gamma e^{-2i\phi}) \tag{2.40}$$

where ϕ is the polar angle of the separation vector θ. The two point shear correlation function is then defined as (Kaiser, 1992)

$$\xi_\pm(\vec{\theta}) = \langle \gamma_{\rm t}(\vec{\theta}')\gamma_{\rm t}(\vec{\theta} - \vec{\theta}')\rangle \pm \langle \gamma_\times(\vec{\theta}')\gamma_\times(\vec{\theta} - \vec{\theta}')\rangle = \int \frac{l{\rm d}l}{2\pi} P_\kappa(l) J_{0/4}(l\theta) \tag{2.41}$$

and the last equality shows how they are related to the lensing power-spectrum. $J_{0/4}$ are the zero-th and four-th order Bessel function of the first kind and correspond to the "+" and "−" correlation function respectively.

All other possible two-point statistical measures of the cosmic shear, such as the shear dispersion in a circle, in ring or the aperture mass dispersion, can be expressed as integrals over these two correlation functions (Crittenden et al., 2002; Schneider et al., 2002; Eifler et al., 2009). We are not interested here to go in more details and we refer for further information about two point shear statistics to Bartelmann and Schneider (2001), Munshi et al. (2008), Eifler et al. (2009).

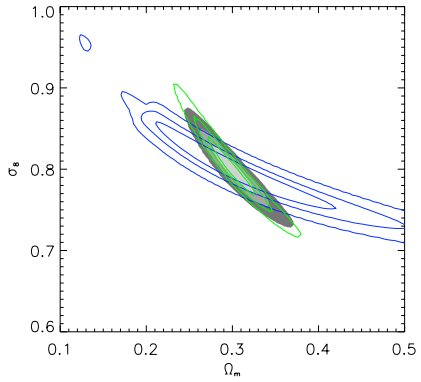

Figure 2.6: Cosmological parameters constraints from shear (green thin solid contours) and magnification (blue thick contours) for a 1500 sq.deg. survey. The filled contour shows the error contour obtains from a 750 deg^2 shear analysis combined with a 750 deg^2 magnification analysis. The image is taken form van Waerbeke (2010).

The shear is not however a direct observable quantity, but it can be inferred from measurement of the ellipticity of the galaxies as it will be shown in the next chapter. Hence measuring the shear correlation function means in practise measuring the ellipticity correlation function. The relation between shear and ellipticity χ correlation function is then:

$$\begin{aligned}\langle \chi_i \chi_j \rangle &= \langle (\chi_i^s + \gamma_i)(\chi_j^s + \gamma_j) \rangle = \\ \langle \chi_i^s \chi_j^s \rangle &+ \langle \chi_i^s \gamma_j \rangle + \langle \gamma_i \chi_j^s \rangle + \langle \gamma_i \gamma_j \rangle \simeq \langle \gamma_i \gamma_j \rangle\end{aligned} \tag{2.42}$$

We assumed here that the observed ellipticity of a galaxy can be written as the sum of its intrinsic ellipticity χ^s and the shear[5] and in the last step we assumed that the intrinsic ellipticities of galaxies are randomly distributed on the sky, so that they are correlated neither with the intrinsic ellipticities nor with the shears of other galaxies. However galaxies can intrinsically align (for example due to tidal forces of a common structure surrounding them) and therefore have correlated intrinsic ellipticities. If this is the case the term $\langle \chi_i^s \chi_j^s \rangle$, known in literature as the II signal, does not vanish.

Analogously if the galaxy ellipticities are correlated with the tidal gravitational field of their host halo, then the intrinsic ellipticity of a nearby source galaxy will be correlated with the lensing shear acting on a more distant source galaxy, leading a non-vanishing $\langle \gamma_i \chi_j^s \rangle$ term. This effect has been discussed for the first time by Hirata and Seljak (2004), and is known as GI signal. Both the II and the GI terms can be sources of systematics in

[5]We refer to the next chapter for a more detailed discussion.

the derivation of the shear correlation function from the ellipticity correlation function. We refer to Heavens and Peacock (1988),Crittenden et al. (2001), Porciani et al. (2002), Hirata and Seljak (2004), Lee and Lee (2008), Okumura et al. (2009), Schneider and Bridle (2010) for further discussion about intrinsic alignment.

2.3.1 3D Weak lensing

The first cosmic shear analyses used only two dimensional shear information (Bacon et al., 2000; Brown et al., 2003; Hamana et al., 2002; Jarvis et al., 2003). However if photometric redshifts of the sources are known it is possible to perform a full 3-dimensional lensing analysis. This allows to improve the accuracy in the determination of cosmological parameter, in particular there is a big gain in the constraint on the dark energy equation of state w (Heavens, 2003), since the expansion history and the growth of structures can be directly traced. The idea is to give a representation of the 3D shear field in terms of spin-spherical harmonics:

$$\gamma_1(\vec{r}) \pm i\gamma_2(\vec{r}) = \sqrt{\frac{2}{\pi}} \sum_{lm} \int \mathrm{d}k k^2 \gamma_{lm}(k) Y_l^m(\hat{\vec{n}}) j_l(kr) \tag{2.43}$$

where $j_l(kr)$ is a spherical Bessel function, Y a spherical harmonic, k is a wave-number, l is an integer, $m = -l, ...l$ and $\hat{\vec{n}}$ represents the direction θ, ϕ. The coefficients γ_{lm} are related to the transform of the lensing potential $\Psi(\vec{r})$ by:

$$\gamma_{lm}(k) = \frac{1}{2}\sqrt{\frac{(l+2)!}{(l-2)!}}\Psi_{lm}(k) \tag{2.44}$$

Using the fact that the lensing potential is related to the gravitational potential by a radial integral and the gravitational potential is related to the over-density δ via Poisson equation we can re-write the above equation in the form :

$$\gamma_{lm}(k) = -\frac{1}{2}\sqrt{\frac{(l+2)!}{(l-2)!}}\frac{3\Omega_\mathrm{m}H_0^2}{2c^2k^2}\int \mathrm{d}k'(k')^2\eta_l(k,k')\delta_{lm}^0 \tag{2.45}$$

where

$$\eta_l(k,k') \equiv \frac{4}{\pi}\int_0^\infty \mathrm{d}w f_K(w) j_l(kw) \int_0^w \mathrm{d}w' j_l(k'w') \frac{f_K(w) - f_K(w')}{f_K(w'} \frac{G(w')}{a(w')} \tag{2.46}$$

This equation relates the coefficients of the shear field to the underlying linear over-density field. In practise a harmonic description of the data is

given defining the following shear estimator:

$$\hat{g}_{lm} \equiv \sqrt{\frac{2}{\pi}} \sum_{\text{galaxies g}} \gamma_g j_l(k s_g) Y_l^m(\hat{\vec{n}}_g) \tag{2.47}$$

where s is the radial coordinate given in terms of photometric redshift. Following a similar procedure used to arrive to equation 2.45 it is possible to relate the coefficient of the shear estimator to the linear over-density. The covariance of this estimator is used then to compute cosmological parameters. The first attempt of a full 3D lensing analyses has been done on COMBO-17[6] dataset (Kitching et al., 2008). Given the small size of the survey the constraints on the dark energy equation of state derived from this analyses are very weak ($w_{\rm DE} = -0.15^{+0.67}_{-0.70}$). As clearly stated by the authors this attempt was mainly a proof of concept and much larger surveys are needed to reach percent accuracy in the determination of $w_{\rm DE}$.

An intermediate approach between 2D and 3D lensing is the so-called *lensing tomography*. In this case the sources are divided in redshift slices and then shear correlation functions are computed inside each slice and between different slices (Schrabback et al., 2010). The description of the shear power spectrum in terms of the matter power spectrum is given by equation 2.39, where in general $k \neq l$. The number of slices used in tomographic analyses is chosen considering the number of available galaxies in the survey (there should be enough galaxies per slice to keep small the shot noise) and the variation of the shear across the redshift range of the whole distribution (if the lensing signal is almost constant then having a lot of slices does not improve the analyses). Different attempts to apply lensing tomography on real data have been done in the last years Bacon et al. (2005); Semboloni et al. (2006); Massey et al. (2007b); Schrabback et al. (2010). The lack of good photometric redshift information and the small size of the surveys didn't allow to really constrain the dark matter equation of state. The best achieved result comes from the analyses of the COSMOS field constrainig $w_{\rm DE} < -0.41$ at 90% confidence level.

[6]The survey consists of five fields each covering 0.26 square degrees. We refer to Wolf et al. (2001, 2004) for more details

Per me si va ne la città dolente,
per me si va ne l'etterno dolore
per me si va tra la perduta gente[0]
Dante (1265-1321) Inferno III

3 Shear and flexion measurements

Measuring with high precision the lens-induced distortion in the galaxy shapes is one of the most challenging aspect of weak lensing. Difficulties arise in first place since galaxies are not intrinsically circular, but they have their own shape. Therefore is not possible to disentangle, observing a single object, the lensing-induced distortion from the intrinsic shape, which is an inaccessible quantity. This means that the only possibility to extract information about shear and flexion is to average over many galaxies in a region where shear and flexion can be considered constant, assuming that the average of the intrinsic galaxy ellipticity and intrinsic galaxy flexion vanishes over a sufficient number of galaxies. Moreover any observed image is the convolution of the real image and the Point Spread Function (PSF). A spherically symmetric PSF causes a circularisation of the object, while any anisotropies in the PSF translate in spurious ellipticity or in general in spurious distortion of the object. Hence any attempt of measuring shear and flexion should take properly into account those effects which might cause severe systematics in the measurements. A sketch showing the effect of intrinsic ellipticity, shear and PSF convolution on a circular image is shown in figure 3.1

Furthermore observed images are pixelated and degraded by noise. Both effects render very challenging, specially for faint sources, any attempt of measuring shear and flexion.

3.1 Measuring ellipticity

We discussed in the previous chapter how a lensing transformation modifies the shape of a given source. In particular if the source is circular, convergence acts to increase the average radius of the image, shear acts to stretch the circle into an ellipse (see figure 3.2). Using equation 2.22 we

[0]Through me the way into the suffering city/through me the way to the eternal pain/through me the way that runs among the lost

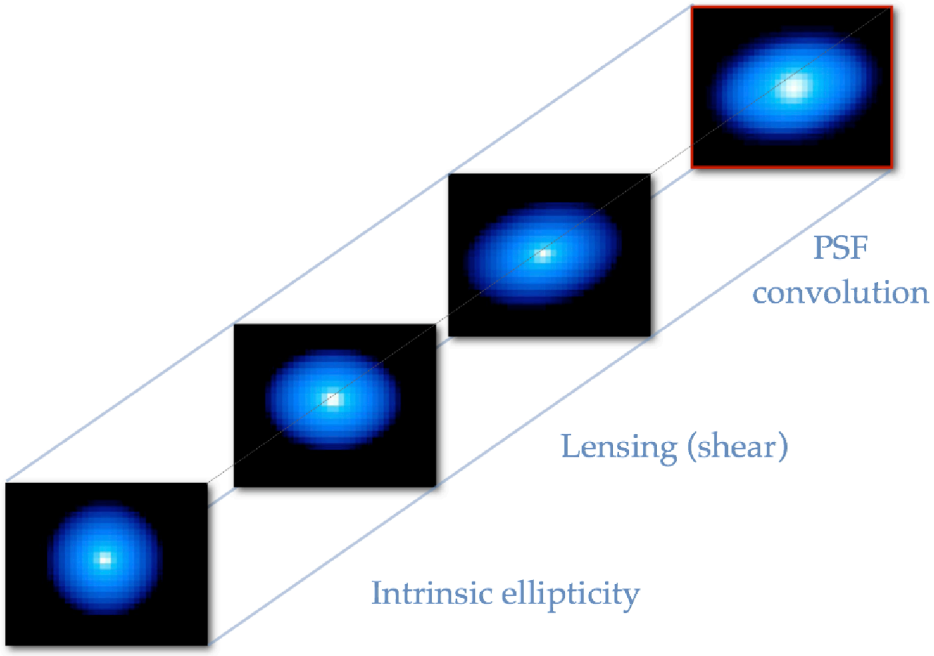

Figure 3.1: Effect of intrinsic ellipticity, shear and PSF convolution on a circular image.

can compute the semi-major axis a and semi-minor axis b of the ellipse in terms of shear and convergence:

$$\begin{aligned} a &= \frac{1}{(1-\kappa+|\gamma|)} \\ b &= \frac{1}{(1-\kappa-|\gamma|)} \end{aligned} \tag{3.1}$$

These two number can be combined to form the ellipticity [1] of the ellipse

$$\epsilon = \frac{a-b}{a+b} = \frac{|\gamma|}{1-\kappa} \equiv g \tag{3.2}$$

This equation shows that the image's ellipticity depends only on g, the *reduced shear*, and not individually on the shear and the convergence. Observationally this is the accessible quantity, as it might be clear also by writing the jacobian of the linearised lensing equation in the following way:

$$A \equiv \frac{\partial \vec{\beta}}{\partial \vec{\theta}} = \left(\delta_{ij} - \frac{\partial^2 \Psi(\vec{\theta})}{\partial \theta_i \partial \theta_j} \right) = (1-\kappa) \begin{pmatrix} 1-g_1 & -g_2 \\ -g_2 & 1+g_1 \end{pmatrix}. \tag{3.3}$$

[1] In mathematical term this is called also *second flattening* and it defines the degree of "squashing", from no flattening (a perfect circle) to complete flattening (a straight line)

The multiplicative factor $(1-\kappa)$ is responsible of rescaling the image, but the distortion is generated by g.

In reality however galaxies are generally not circular and therefore the relation between ellipticity and shear is not as straightforward as presented in equation 3.2. Seitz and Schneider (1997) showed that if a galaxy has a non vanishing intrinsic ellipticity ϵ^s, the relation between observed ellipticity and reduced shear reads as:

$$\epsilon = \frac{\epsilon^s + g}{1 + g^\star \epsilon^s} \qquad (3.4)$$

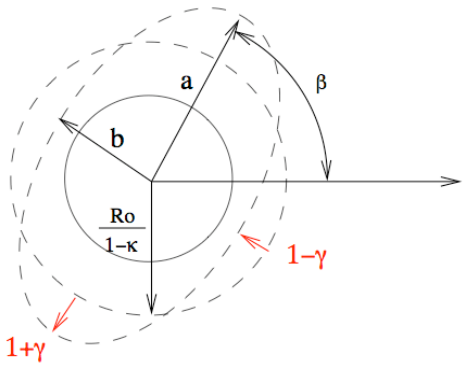

Figure 3.2: Effect of shear and convergence on a circular source from Munshi et al. (2008)

Note that this relation is valid for $|g| \leq 1$. This nice mathematical relation is unfortunately useless when applied to a single object, since is not possible to infer ϵ^s from any observation. We will come back to this point in section 3.3.

The definition of ellipticity we gave above is note unique. Another possible definition of the ellipticity is given by[2]:

$$\chi = \frac{a^2 - b^2}{a^2 + b^2} = \frac{2|g|}{1 + |g|^2} \qquad (3.5)$$

In this case the relation between ellipticity and reduced shear is more complicated and in particular is non-linear. It will be clear later on in the chapter the reason why this ellipticity definition has been introduced. If the galaxy has a non vanishing intrinsic ellipticity χ^s, equation 3.5 becomes more complicated:

$$\chi^s = \frac{\chi - 2g + g^2\chi^\star}{1 + |g|^2 - 2\,\mathrm{Re}(g\chi^\star)} \qquad (3.6)$$

Schneider and Seitz (1995). ϵ and χ are related through:

$$\begin{aligned} \epsilon &= \frac{\chi}{1 + (1 - |\chi|^2)^{1/2}} \\ \chi &= \frac{2\epsilon}{1 + |\epsilon|^2} \end{aligned} \qquad (3.7)$$

Other possible definitions of ellipticity in terms of semi and major-axes would be possible, but they are not used in weak-lensing applications. In the following we will call "ellipticity" both ϵ and χ as is normally done in the literature.

[2]In mathematical term this is called *third eccentricity*.

3.1.1 PSF convolution

The observed shape of any object is the result of a convolution of its surface brightness $I^0(\vec{\theta})$ with the point spread function $P(\vec{\theta})$ due to instrumental and atmospheric effects:

$$I^{\rm con}(\vec{\theta}) = \int I^0(\vec{\theta}')P(\vec{\theta}-\vec{\theta}')\mathrm{d}^2\theta'. \tag{3.8}$$

If the PSF is spherically symmetric, the convolution results in a smearing of the surface brightness with the effect of rendering the object more circular. Moreover any anisotropy in the PSF shape will imprint a spurious ellipticity in the observed surface brightness. Correcting for these effects is a crucial step in any weak lensing analysis. Furthermore the PSF can vary spatially and in time, and hence it must be measured and modelled for each image individually. This can be done using stars in our own galaxy present in the field. Since the number of stars in the field might not be large enough to smoothly map the PSF variation across the field, usually interpolating techniques between the points where stars appear on the image are employed (Jarvis and Jain, 2004; Hoekstra, 2004; Jain et al., 2006).

3.2 Available tools

In the last 15 years there has been a flourishing of different techniques to extract lensing information from convolved and very noise images of galaxies. The reason is that, as we mentioned already, having unbiased shear estimation is of crucial importance to constrain cosmological parameters and in particular dark energy models. We will summarise here the most used one and we refer to Bridle et al. (2009) for a more extended presentation. A useful way to categorise different lensing estimates is by introducing the concept of *active* and *passive* approaches (Massey et al., 2007a). Active approaches start defining a model for the unlensed and unconvolved source, they shear it and they convolve finally with a model for the PSF. A minimisation procedure is then used to estimate the best-fit lensing transformation parameters. Examples of methods using an active approach are LENSFIT (Miller et al., 2007; Kitching et al., 2008) and the method proposed by Bernstein and Jarvis (2002). Passive approaches on the other are based on measurement of moments of the convolved galaxy surface brightness. Combinations of second order moments are then used to build up a shear estimator and corrections for the effect of the PSF are employed. Prototype of those methods is KSB (Kaiser et al., 1995), which was also the first proposed method for converting measurements of galaxy ellipticity into shear.

3.2.1 Model fitting approach

One of the most straightforward approaches to estimate the ellipticity of galaxies is model fitting (Kuijken, 1999a; Bridle et al., 2002). The idea is very simple and relies on the choice of a model for the source (typically an elliptical Sérsic profile) and a model for the PSF. These two models have to be convolved in order to describe the observed galaxy image. Usually a Monte Carlo method is used to find best-fitting galaxy model parameters for each individual galaxy. The basic rationale of this approach is that if the family of models is a good representation of the true surface brightness profile, the highest possible S/N of the result parameter should be obtained. The most recent and developed tool employing a model fitting approach is LENSFIT (Miller et al., 2007; Kitching et al., 2008). It performs a Bayesian technique for model selection and the goal is to determine the posterior probability distribution of the model parameters. In the Bayesian approach the likelihood function has to be determined and a prior probability distribution for the ellipticity distribution has to be assumed. Normally the model encodes 6 free parameters: position (x and y), ellipticity (x and y), brightness and radius. Miller et al. (2007) showed that if the fit is done in Fourier space is possible to analytically marginalise over position and brightness, hence one needs to marginalise only over the radius to have the likelihood function for the ellipticity. Model-based approaches often perform excellently for strongly degraded data because certain implicit or explicit priors keep the results within reasonable bounds, e.g. the source ellipticity smaller than unity. On the other hand, when imposing these priors to data, whose characteristics differ from the expectation, these approaches may also bias the outcome.

3.2.2 Shapelets

The basic idea here is to linearly decomposed galaxy images into a series of orthogonal basis functions (called shapelets), which are product of Gaussian with Hermite or Laguerre polynomials (in Cartesian or polar coordinate respectively). The same decomposition can be done for the convolution kernel and the convolution can be expressed in shapelet space as a simple matrix multiplication. Hence a deconvolution can be done analytically simple by a matrix inversion (Refregier and Bacon, 2003). However gaussian-based function requires a large number of coefficients to reproduce the extend wings of a typical galaxy. If the wings are truncated in the model since they are hidden in the noise, galaxy ellipticities will be systematically underestimated. Moreover it has been shown that shear estimate turns out to be biased if the shape to be described has too steep

profile Melchior et al. (2010a)

3.2.3 Moments

Another possible approach to measure ellipticity of galaxies is based on the moments of the surface brightness distribution. Historically this has been the first method used in weak lensing analysis and it has been developed by Kaiser et al. (1995).

The shape of an extended source can be described by angular moments of its surface brightness distribution $I(\vec{\theta})$,

$$Q_{ij...k} = \int I(\vec{\theta})\theta_i\theta_j...\theta_k \mathrm{d}^2\theta \ . \tag{3.9}$$

Q is the total flux, Q_i defines the centroid of the image, and higher-order moments provide information on the image's morphology. Without loss of generality we assume, from now on, the distribution to be centred such that the two first-order moments vanish. Combinations of second moments can be used to quantify the image's ellipticity, which we introduce as

$$\chi = \frac{(Q_{11} - Q_{22}) + 2iQ_{12}}{Q_{11} + Q_{22}} \ . \tag{3.10}$$

If the ellipticity is defined according to equation 3.2, its representation in terms of moments reads as:

$$\epsilon = \frac{(Q_{11} - Q_{22}) + 2iQ_{12}}{Q_{11} + Q_{22} + 2(Q_{11}Q_{22} - Q_{12}^2)^{1/2}} \ , \tag{3.11}$$

Model-independent approaches do not – or at least not as strongly – assume particular knowledge of the data to be analysed. They should therefore generalize better in applications, where priors are not obvious, e.g. on the intrinsic shape of lensed galaxies. The traditional KSB method forms a shear estimator from the second-order moments of lensed galaxy images. When doing so, it is not guaranteed that reasonable shear estimates can be achieved for each galaxy. Consequently, KSB requires a careful setup, which is adjusted to the characteristics of the data to be analysed. KSB furthermore employs strong assumptions on the PSF shape, which are not necessarily fulfilled for a given telescope or observation (Kuijken, 1999a). A detailed analysis of this method will be given in the next chapter.

3.3 From ellipticity to shear

Information on the intrinsic ellipticity of a single object is not accessible. Hence in order to estimate the shear one has to average over many galaxies

in a region where g can be considered constant, assuming that the average[3] of χ^s vanishes,

$$0 = \langle \chi^s \rangle = \left\langle \frac{\chi - 2g + g^2\chi^*}{1 + |g|^2 - 2\,\mathrm{Re}(g\chi^*)} \right\rangle . \tag{3.12}$$

This equation does not have a general analytical solution. Therefore either a numerical solution for g is searched, either a Taylor expansion around $g \simeq 0$ can be done:

$$g \simeq \frac{\langle \chi \rangle}{2} \left(\frac{1}{1 - \sigma_\chi^2} \right) \tag{3.13}$$

The term in bracket is the so-called *shear responsivity* and represents the response of ellipticity to a small shear, while σ_χ is the dispersion of the intrinsic ellipticity distribution. The last equation provides unbiased shear estimates if the ellipticity of the single galaxies and the ellipticity dispersion are unbiased. Moreover the shear must be small otherwise a linear approximation of equation 3.12 is not sufficient.

We introduced in the previous section another ellipticity estimator ϵ. In this case it is possible to show (Seitz and Schneider, 1997) that:

$$\langle \epsilon^n \rangle = g^n \tag{3.14}$$

This result leads to the fact that $\langle \epsilon \rangle$, in contrast with $\langle \chi \rangle$ is always an unbiased local estimator of the shear. This means, in other terms, that if ϵ is used as definition of galaxy ellipticity, the shear can be perfectly recovered averaging over a sufficiently high number of sources without any need of measuring the dispersion of the intrinsic ellipticity of the considered population.

In practical applications χ and ϵ are both used as definition for ellipticity. However methods based on moments measurement normally use χ since it has a more simple representation in terms of moments and it turns out to be less noisy than ϵ.

3.4 Accuracy

Typically the intrinsic ellipticity dispersion of galaxies is $\sigma_\chi \simeq 0.3$. Therefore one needs a large number N of galaxies to decrease the statistical noise $\sim \sigma_\chi / \sqrt{N}$ on the shear measurement.

The number of available galaxies for averaging depends on the analyses one want to perform. In cluster lensing applications, the shear is usually estimated on a grid which covers the lens plane (Bartelmann et al.,

[3] we consider here a simple arithmetical mean

Table 3.1: On going and future weak lensing experiments, with area coverage, depth and number of galaxies with measurable shapes

	Area/sq.deg.	Median z	Density[1]	Start date
DES[2]	5000	~ 0.7	~ 10	2011
JDEM[3]	2000	1	$20-30$	2013
EUCLID[4]	20000	~ 0.9	40	2017
LSST[5]	20,000	~ 1.2	40	2018

1996; Cacciato et al., 2006; Merten et al., 2009). The size of the grid is chosen such that in each grid cell the lensing potential can be considered almost constant. Normally this value is set to be $\approx 35''$. Assuming a typical number density of background galaxies of $30/\text{arcmin}^2$, this means that, on average, in each grid cell there are ≈ 10 galaxies, leading to a noise in the shear measurement around 10%.

In cosmic shear the quantity which is normally estimated is the two point shear correlation function. The correlation is computed, as shown in section 2.2, by averaging all possible galaxy pairs separated by an angular scale $d\theta$. Using a survey like COSMOS (Scoville et al., 2007), covering 1.64deg^2 and with roughly 80 galaxies per squared arcminute, the average can be done over approximately $10^3 - 10^4$ pairs (Schrabback et al., 2010), meaning that the statistical error drops to percent level. These numbers are the state of the art for cosmic shear measurements nowadays. New surveys will cover even large areas in the sky and they will detect even fainter galaxies (see Table 3.1 for an overview of the characteristics of the new generation lensing surveys) and therefore the impact of statistical errors in cosmic shear measurement will drop below the per-mille level.

It is therefore crucial in order to fully exploit the future cosmic shear analyses to be able to measure galaxy ellipticities with an accuracy of 1 part in 10^{-3}.

The small statistical errors make cosmic shear an ideal tool for future dark energy studies (Peacock et al., 2006; Albrecht et al., 2006), provided that the other systematics which might arising in shear measurements will be of the same magnitude. In particular Amara and Réfrégier (2008) showed that this is the requirement in order to get percent constraints on dark energy from a DUNE-like mission. These very tight requirements challenged the community to test different pipelines used to

[1] Number of galaxies per squared arcminute
[2] http://www.darkenergysurvey.org
[3] http://jdem.gsfc.nasa.gov
[4] http://sci.esa.int/euclid
[5] http://www.lsst.org

measuring galaxy ellipticities under realistic conditions and several test programs have been established. The first one has been the Shear TEsting Program (STEP) (Heymans et al., 2006; Massey et al., 2007b), followed by the GRavitational lEnsing Accuracy Testing 2008 (GREAT08) (Bridle et al., 2009). The main result of those tests is that the current pipelines are good enough to exploit the current lensing survey but they cannot reach the required per-mille accuracy necessary for the new generation of lensing survey.

3.5 Flexion measurements

Flexion is related to the third derivative of the lensing potential (third-order lensing effect) and is responsible for the skewed and arclike appearance of lensed galaxies. We described the flexion formalism in section 2.1.3, where we showed that any third order distortion caused by a single lens plane, can be expressed as a sum of a spin-1 field, namely the $\mathcal{F}$-flexion, and a spin-3 field, namely the $\mathcal{G}$-flexion. $\mathcal{F}$-flexion is a direct local measurement of $\nabla\kappa$ and therefore it is weaker and shorter range than the $\mathcal{G}$-flexion, which is a local measurement of ∇g. This behaviour can be clearly seen in figure 3.3 where we computed the modulus of the flexion fields expected for a NFW halo.

Following the representation of the ellipticity in terms of second moments of the surface-brightness, we introduce here some combinations of higher moments of the surface brightness, which we will eventually relate to the flexion field. We will closely follow the notation presented by Okura et al. (2007). We start defining two combinations of third moments

$$\begin{aligned} \hat{\zeta} &\equiv (Q_{111} + Q_{122}) + i(Q_{112} + Q_{222}) \\ \hat{\delta} &\equiv (Q_{111} - 3Q_{122}) + i(3Q_{112} - Q_{222}) \end{aligned} \tag{3.15}$$

which have respectively spin-1 and spin-3. Since flexion has dimension of $1/L$ we need to normalise $\hat{\zeta}$ and $\hat{\delta}$ with a combination of moments having spin-0 and dimension L^4. Usually this is done defining the normalisation factor as a combination of fourth moments:

$$\xi \equiv Q_{1111} + 2Q_{1122} + Q_{2222} \tag{3.16}$$

Using this definition, the so-called *HOLICS* (in Okura et al. (2007) terminology) read:

$$\begin{aligned} \zeta &\equiv \frac{\hat{\zeta}}{\xi} \\ \delta &\equiv \frac{\hat{\delta}}{\xi} \end{aligned} \tag{3.17}$$

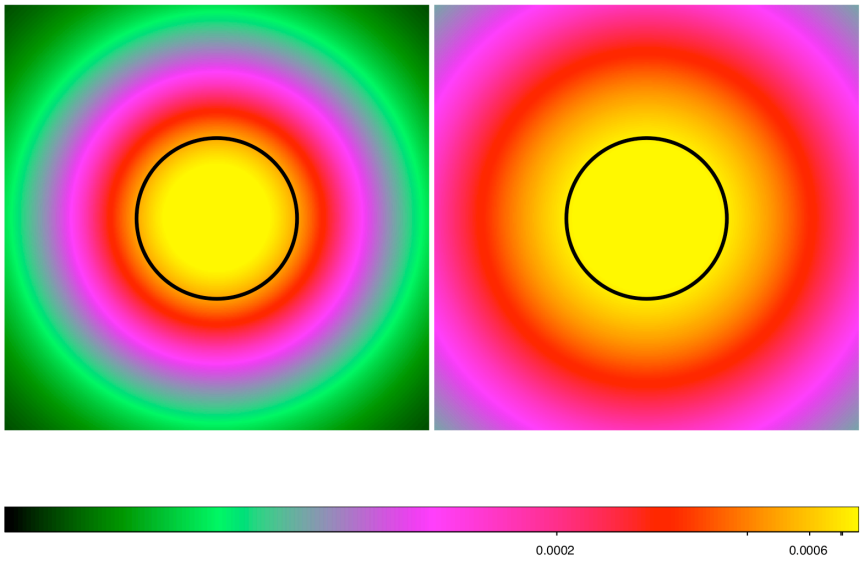

Figure 3.3: Modulus of $\mathcal{F}$-flexion (*left panel*) and $\mathcal{G}$-flexion (*right panel*) calculated for a NFW halo with $M = 5 \times 10^{14} M_{\odot}$ at $z = 0.5$. The sources are assumed here to be at $z = 2$. The *black circle* indicated the scale radius of the halo.

Another possible choice for the normalisation would be $(TrQ)^2 = (Q_{11} + Q_{22})^2$, which has the advantage of being a combination of second moments instead of fourth moments (which might be difficult to measure in practise due to noise):

$$\begin{aligned} \tilde{\zeta} &\equiv \frac{\hat{\zeta}}{(TrQ)^2} \\ \tilde{\delta} &\equiv \frac{\hat{\delta}}{(TrQ)^2} \end{aligned} \tag{3.18}$$

However using this normalisation renders the transformation of $\tilde{\delta}$ and $\tilde{\zeta}$ under lensing more complicated.

We compute now how ζ and δ transform under lensing. The computation is lengthy and relies on two steps:

- Computing the transformation of 3rd and 4th moments under lensing. This computation can be done neglecting the centroid shift induced by lensing:

$$\begin{aligned} Q^s_{ijk} \simeq\ & A_{il}A_{jm}A_{kn}Q_{lmn} + \frac{1}{2}(A_{il}A_{jm}D_{kno} + A_{jm}A_{kn}D_{ilo} \\ & + A_{il}A_{kn}D_{jmo} - 4A_{il}A_{jm}A_{kn}F_o)Q_{lmno} \end{aligned} \tag{3.19}$$

$$\begin{aligned} Q^s_{abcd} \simeq\ & A_{aj}A_{bm}A_{co}A_{dq}Q_{jmoq} + \frac{1}{2}(A_{aj}A_{bm}A_{co}D_{dqr} + A_{bm}A_{co}A_{dq}D_{ajr} \\ & + A_{aj}A_{co}A_{dq}D_{bmr} + A_{aj}A_{bm}A_{dq}D_{cor} - 4A_{aj}A_{bm}A_{co}A_{dq}F_r)Q_{jmoqr} \end{aligned} \tag{3.20}$$

  where A is the jacobian matrix defined in equation 3.3 and $D_{ijk} = A_{ij,k}$ (Bacon et al., 2006).

- Correcting for the lensing induced centroid shift. The centroid shift can be written at first order in shear and flexion as:

$$\Delta^\theta_i = TrQ\left[\frac{3}{2}F_i + \frac{5}{4}(F^\star\chi)_i + \frac{1}{4}(G\chi^\star)_i\right]. \tag{3.21}$$

  We can use this result to relate the HOLICs computed using moments with respect to the true centre (ζ, δ) with the one computed in the first step with respect to the apparent centre (ζ^a, δ^a):

$$\begin{aligned} \zeta &= \zeta^a + 2\frac{TrQ}{\xi}\Delta^\theta + \frac{TrQ}{\xi}(\chi\Delta^{\theta\star}) \simeq \zeta^a + \frac{(TrQ)^2}{\xi}\left(3F + 4F^\star\chi + \frac{1}{2}\right) \\ \delta &= \delta^a + 3\frac{TrQ}{\xi}\Delta^\theta \simeq \delta^a + \frac{9}{2}\frac{(TrQ)^2}{\xi}\chi F \end{aligned} \tag{3.22}$$

These calculations show that at first order in the flexion fields the transformation of δ and ζ under a lensing transformation read as:

$$\begin{aligned}\zeta^{\rm s} &= \frac{1}{(1-\kappa)(1-4\,{\rm Re}(g^*\eta)-5\,{\rm Re}(F\iota_I^*)-{\rm Re}(G\iota_{III}^*))}\\ &\times\left[\zeta-2g\zeta^*-g^*\delta-\frac{1}{4}\left(8F^*\eta-16\frac{(TrQ)^2}{\xi}F^*\chi\right.\right.\\ &\left.\left.+9F-12\frac{(TrQ)^2}{\xi}F+2G\eta^*-2\frac{(TrQ)^2}{\xi}G\chi^*+G^*\lambda\right)\right],\end{aligned} \tag{3.23}$$

$$\begin{aligned}\delta^{\rm s} &= \frac{1}{(1-\kappa)(1-4\,{\rm Re}(g^*\eta)-5\,{\rm Re}\,F\iota_I^*-{\rm Re}(G\iota_{III}^*))}\\ &\times\left[\delta-3g\zeta-\frac{1}{4}\left(10F\eta+7F^*\lambda-18\frac{(TrQ)^2}{\xi}F\chi+3G\right)\right],\end{aligned} \tag{3.24}$$

where η and λ are dimensionless spin-2 and spin-4 quantities, respectively, defined with 16-pole moments, and ι_I and ι_{III} are spin-1 and spin-3 quantities, respectively. They are defined as following:

$$\eta \equiv \frac{(Q_{1111}-Q_{2222})+2i(Q_{1112}+Q_{1222})}{\xi} \tag{3.25}$$

$$\lambda \equiv \frac{(Q_{1111}-6Q_{1122}+Q_{2222})+4i(Q_{1112}-Q_{1222})}{\xi} \tag{3.26}$$

$$\iota_I \equiv \frac{(Q_{11111}+2Q_{11122}+Q_{12222})+i(Q_{11112}+2Q_{11222}+Q_{22222})}{\xi} \tag{3.27}$$

$$\iota_{III} \equiv \frac{(Q_{11111}-2Q_{11122}-Q_{12222})+i(3Q_{11112}+2Q_{11222}-Q_{22222})}{\xi} \tag{3.28}$$

Moreover $\zeta^{\rm s}$ and $\delta^{\rm s}$ denotes the intrinsic first and second flexion and the *reduced flexion* has been defined as:

$$\begin{aligned}F &\equiv \frac{\mathcal{F}}{1-\kappa}\\ G &\equiv \frac{\mathcal{G}}{1-\kappa}\end{aligned} \tag{3.29}$$

Equations 3.23 and 3.24, relating the intrinsic deformation $(\zeta^{\rm s},\delta^{\rm s})$ with the lens-induced deformation (ζ,δ), look complicated, involving high order moments of the light distribution and different combinations of the lensing fields. Normally they are simplified employing the following approximations:

- The expectation value of the intrinsic flexion vanishes;

- η and λ are small;
- Terms containg 6-th moments are negligible;
- The shear is small.

Under these conditions a linear relation between the HOLICs and the flexion fields can be found:

$$F \simeq \left\langle \frac{\zeta}{(9/4) - 3(trQ)^2/\xi} \right\rangle \qquad G \simeq \frac{4}{3}\langle\delta\rangle \tag{3.30}$$

3.5.1 Cross talk between shear and flexion

In the derivation of equations 3.30 all terms showing cross talk between shear and flexion have been neglected. This approximation is certainly valid for cosmic flexion and in the out-skirts of galaxy clusters, but we expect them to break down in proximity of massive structures where both the shear and the flexion cannot be considered small anymore. We re-derive here the relation between the flexion estimators and the lensing fields dropping the assumption that the shear-flexion cross talk is negligible. If those terms are not neglected we get to the following equation for the G flexion.

$$0 = \langle\delta\rangle - 3g\langle\zeta\rangle - (1/4)\left[10F\langle\eta\rangle - 18F\left\langle \frac{\chi(TrQ)^2}{\xi} \right\rangle + 3G\right] \tag{3.31}$$

We assumed here that the convergence, the shear and the flexion are constant in the area in which the average is taken, and that all terms in the denominator of equation 3.24 can be neglected. Moreover we assume that also the term $G\langle\lambda\rangle$ can be neglected. We will comment on these assumptions in the next section. We can now write $\langle\zeta\rangle$ in terms of F according to equation 3.30. This approximation is sufficient here since any further correction would create terms which are second order in g. Moreover we can use the well know relation $\langle\chi\rangle \simeq 2g$ and the fact that $\langle\eta\rangle \simeq 3g$ as showed by Okura and Futamase (2009) in order to write the relation between δ and G in terms of g and F :

$$\frac{4}{3}\langle\delta\rangle \simeq G + gF\left(19 - 12\left\langle \frac{(TrQ)^2}{\xi} \right\rangle\right) - 6F\left\langle \chi\frac{(TrQ)^2}{\xi} \right\rangle \tag{3.32}$$

The terms TrQ and ξ are spin 0 quantities and give information about the apparent size of the objects. Therefore if all the sources are of the same size (which is a good approximation for ground base observation where the apparent size of the objects is set by the PSF) then the term $(TrQ)^2/\xi$ is almost constant and therefore we can make the following approximation:

$$\left\langle \frac{\chi (TrQ)^2}{\xi} \right\rangle \simeq \frac{(TrQ)^2}{\xi} \langle \chi \rangle \simeq 2g \frac{(TrQ)^2}{\xi} \tag{3.33}$$

leading to the simpler expression:

$$\frac{4}{3}\langle \delta \rangle \simeq G + gF\left(19 - 24\frac{(TrQ)^2}{\xi}\right) \tag{3.34}$$

Employing the same approximations we can compute a similar expression for $\langle \zeta \rangle$:

$$\begin{aligned}
&\langle \zeta \rangle - 2g\langle \zeta^\star \rangle = \frac{9}{4}F - 3\left\langle \frac{(TrQ)^2}{\xi} \right\rangle + \frac{9}{4}g^\star G \\
&- \frac{1}{2}G\left\langle \frac{(TrQ)^2}{\xi}\chi^\star \right\rangle + 6F^\star g - 4F^\star \left\langle \frac{(TrQ)^2}{\xi}\chi \right\rangle \\
&\simeq F\left(\frac{9}{4} - 3\frac{(TrQ)^2}{\xi}\right) + g^\star G\left(\frac{9}{4} - \frac{(TrQ)^2}{\xi}\right) + 2F^\star g\left(3 - 4\frac{(TrQ)^2}{\xi}\right)
\end{aligned} \tag{3.35}$$

3.5.2 On some approximations

This paragraph is a bit technical and gives a justification on the approximations made in order to arrive at equations 3.34 and 3.35. We concentrate here on the assumptions we used to derive equation 3.34, but the same line of argument can be used also for the derivation of equation 3.35. We assumed in the previous section that:

- The term $G\langle \lambda \rangle$ can be neglected.
- All the terms in the denominator of equation 3.24 are small, and therefore can be neglected;

The first assumption is easy to justify since λ is a spin-4 quantity (i.e. it has a directional dependence) and therefore the expectation value of the intrinsic λ is assumed to vanish. Moreover the fact that λ is a spin-4 quantity means that its lensing induced change can only be related to

terms like GF, g^2,...or any combinations of the lensing fields producing a spin-4 field. This implies that the term $G\langle\lambda\rangle$ won't be linear in the lensing fields and therefore can be neglected for our purposes. In order to justify the second assumption we perform a Taylor expansion of the denominator of equation 3.24 and we compute the correction terms to equation 3.34 which are first order in the lensing field:

$$\begin{aligned} Cor = \mathrm{Re}(g^\star)\left[\eta\delta - 10F\eta - 7F^\star\lambda + 18\frac{(TrQ)^2}{\xi}F\chi - 3G\right] \\ + \mathrm{Re}(F\iota_I^\star)[5\delta - 15g\zeta] + \mathrm{Re}(G\iota_{III}^\star)[\delta - 3g\zeta] \end{aligned} \tag{3.36}$$

The next step is to take the average of the correction terms Cor under the usual assumption that the lensing fields are constant in the region over which the average is taken:

$$\begin{aligned} \langle Cor\rangle = 4g_i\langle\delta\eta_i\rangle - Fg_i\left(10\langle\eta\eta_i\rangle - 18\frac{(TrQ)^2}{\xi}\langle\chi\eta_i\rangle\right) - 15gF_i\langle\zeta\iota_{Ii}\rangle \\ + 7F^\star g_i\langle\lambda\eta_i\rangle + 5F_i\langle\delta\iota_{Ii}\rangle + G_i\langle\delta\iota_{IIIi}\rangle - 3gG_i\langle\zeta\iota_{IIIi}\rangle \end{aligned} \tag{3.37}$$

The first term ($\langle\delta\eta_i\rangle$) is an average between a spin-3 and a spin-2 quantity, and therefore vanishes. Analogously vanish the second to last term ($\langle\delta\iota_{Ii}\rangle$) and the last term ($\langle\zeta\iota_{IIIi}\rangle$) being an average between a spin-1 and a spin-3 field. From the previous section we know that η and χ are both related to the source's ellipticity. It is therefore a reasonable guess that the terms $\langle\eta\chi\rangle$ and $\langle\eta\eta\rangle$ are proportional to the ellipticity dispersion σ_ϵ^2. Typically $\sigma_\epsilon \simeq 0.3$. This order or magnitude calculation tells us that the terms in brackets in the equation above give only a percent contribution to the gF term in equation 3.34. It is more difficult to argue about the order of magnitude of the left over terms. They do not vanish since they involve average of spin-1 quantities ($\langle\zeta\iota_{Ii}\rangle$), spin-3 quantities ($\langle\delta\iota_{IIIi}\rangle$) and spin-4 and spin-2 quantities ($\langle\lambda\eta_i\rangle$). However we expect them to be very small, since they all involve high-order moments of the light distribution. Moreover all these terms are practically impossible to be measured since noise dominates at large scales in any real galaxy image.

3.5.3 Tests

In this section we present some preliminary tests we did in order to quantify the importance of the cross-talk between shear and flexion in a galaxy cluster environment. We start discussing the possible contaminations to the G-flexion signal. The first step is to study the relative importance of the G term and the $gF(24 - 19(TrQ)^2/\xi)$ term appearing on the right

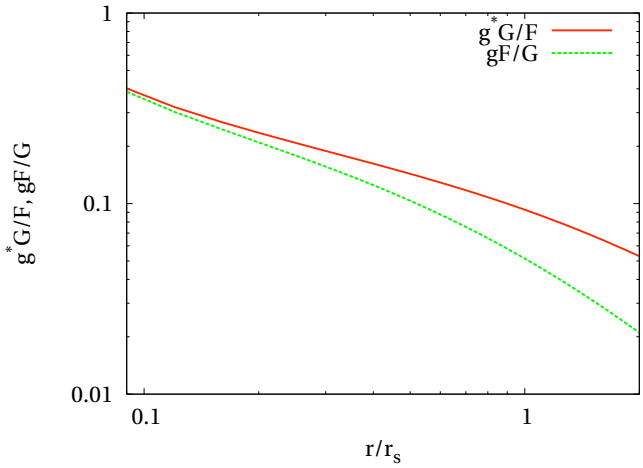

Figure 3.4: Ratio between Fg and G-flexion field and between Gg^* and F-flexion as a function of the distance from cluster centre. We assume here that the density profile of the cluster is described by a NFW profile.

hand side of equation 3.34 as a function of the distance from the cluster centre. We assume that the density profile of the cluster is described by an NFW profile and we assume that all the sources have the same size, such that equation 3.34 holds. Furthermore we assume that the profile of the sources is a circular top hat. This is a very crude approximation, but for a source with this profile it possible to compute analytically $(TrQ)^2/\xi = 3/4$, which implies that $(19 - 24(TrQ)^2/\xi) = 1$. This means that the relative importance between the two terms of the r.h.s. of equation 3.34 is given simply by ratio Fg/G. We plot its behaviour as a function of the distance from the cluster centre in figure 3.4 (green curve). In general we have $(TrQ)^2/\xi < 3/4$[4], meaning that the result shown in figure 3.4 has to be considered as a lower limit.

At scales smaller than half the scale radius of the cluster, the error commited if one identifies the measured field δ with the flexion G is larger than 10%. These scales are very interesting since are intermediate between the pure weak lensing regime (shear only) and the strong lensing regime and are the scales where most of the flexion signal is. Therefore it is extremely important to have in mind that what δ probes at these scales is a combination of G-flexion and a product between F-flexion and reduced shear.

We can perform the same analyses for the F-flexion. We start noticing that any measurement of ζ traces always the $g^\star G$ field and not the F field,

[4]For a Sérsic type galaxies we find numerically $(TrQ)^2/\xi \simeq 0.3$

if the same assumptions about the source properties are employed (this is clear substituting $(TrQ)^2/\xi) = 3/4$ in equation 3.35). This field can have up to half of the expected flexion field strength in the very central region of the cluster as it it clear from figure 3.4 (red line).

As second step we considered a more realistic situation. We simulated a triaxial galaxy cluster with substructures (Giocoli et al. in prep) and we computed its lensing signal. We produced discrete maps of the convergence, the shear and the flexion (128×128pixel), and for each pixel we simulated 100 galaxies [5] with an intrinsic ellipticity dispersion of $\sigma = 0.3$, following a Sérsic-type profile:

$$I(r) = I_0 \exp\left[-b_{n_s}\left(\left(\frac{r}{R_e}\right)^{1/n_s} - 1\right)\right] \tag{3.38}$$

where R_e is the radius containing half of the flux and n_s the Sérsic index and b_{n_s} is a constant which depends on n_s. This type of profile is identical to a Gaussian for $n_s = 0.5$ and is steeper in the centre for $n_s > 0.5$. In the following test, we assume $n_s = 1.5$, which represents the average value for rather bright galaxies in the COSMOS field (Sargent et al., 2007). We applied to each of them a lensing transformation according to the value of the lensing fields in the pixel, we measured their surface brightness moments after the transformation, and we computed for each of them δ according to equation 3.24. We then take the average of δ inside each pixel and we produced a "measured" G-flexion map. The result is shown in figure 3.5. It is clear that there is a region (the one inside the big circle in the figure), with radius almost the scale radius of the cluster, where the measured G-flexion signal (top right panel) does not match the theoretical one (bottom left panel). The difference between the two maps can be explained if the Fg field (bottom right panel) is considered. This result confirms the previous simple analyses: for scales smaller than the scale radius, δ is not a tracer of the G-flexion, but rather of a combination of G-flexion and F-flexion times shear, as it is clearly shown in equation 3.34.

3.5.4 Outlook

There are still a lot of open questions concerning flexion measurements which we plan to address in the next future:

- The relative importance of the mixed terms (shear times flexion) in equations 3.34 and 3.35 with respect to the flexion field depends on the cluster properties (which determine the density profile) and

[5] We choose this very high number of object in order to have an almost negligible statistical error.

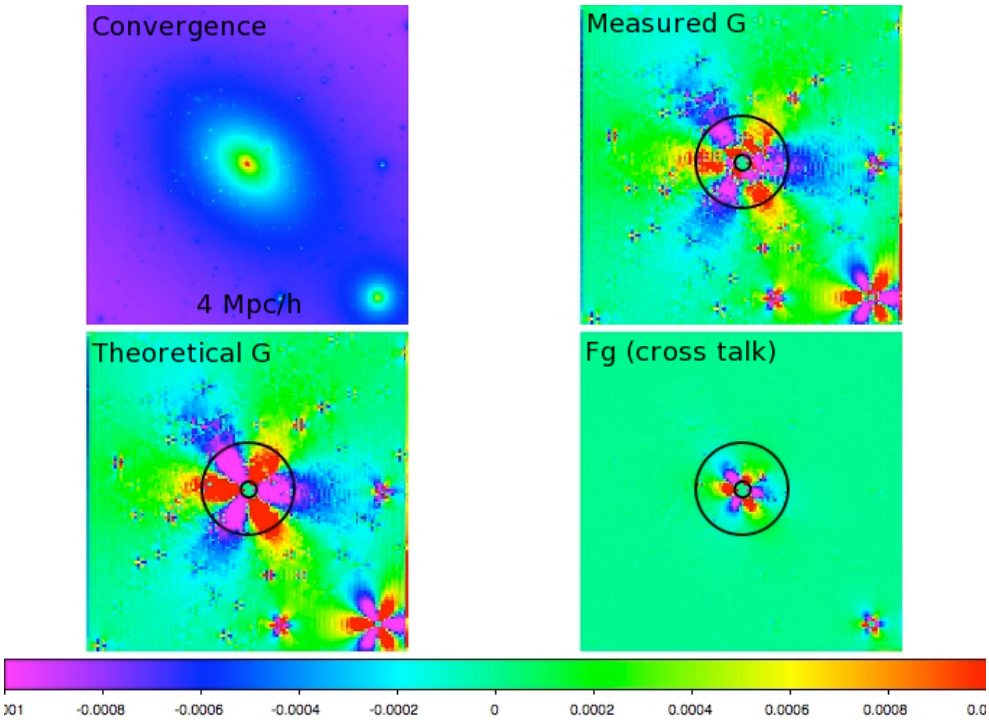

Figure 3.5: *Top left panel*: convergence map of a cluster of $10^{15} M_{\odot}$ with substructure at redshift $z = 0.5$. The sources are assumed to be at $z = 2$. *Top right panel:* map obtained averaging δ over 100 galaxies inside each pixel. The galaxies follow a Sérsic profile and have an intrinsic ellipticity dispersion of $\sigma = 0.3$. All of them are sheared and flexed according to the shear and flexion value inside the pixel. *Bottom left panel:* Theoretical G-flexion calculated from the potential of the simulated cluster. *Bottom right panel:* Theoretical gF field calculated from the potential of the simulated cluster. The larger circle represents the region in which the gF field is not negligible anymore with respect to the G-flexion ($gF/G > 10\%$). The smaller circle encompasses the region of strong lensing. The size of all images is $4Mpc/h$.

on the morphological properties of the source population via the $(TrQ)^2/\xi$ term. Detailed investigations are planned in this direction.

- Measurements of F-flexion are tricky since any error in the centroid determination seriously affects the estimation of ζ (which is a spin 1 field). With which precision do we have to know the centroid ?

- In order to measure (δ, ζ) is necessary to have information on the 4th moment of the light distribution of the source, since they appear in the normalisation ξ. With which precision are we able to measure those moments ?

- As we previously discussed it is possible to choose $(TrQ)^2$ as normalisation for the HOLICs instead of ξ. The obvious advantage of this choice is that only 2nd and 3rd moments have to be measured. But how are the new quantities $(\tilde{\delta}, \tilde{\zeta})$ related to the flexion and shear fields ?

- Which is the intrinsic flexion dispersion ? This is a crucial information to have since it determines the statistical error associated to any flexion measurement.

Another key question, which requires a particular attention, concerns the PSF deconvolution. There have been attempts to fully extend the KSB formalism taking into account the effects of Gaussian weighting in calculation of noisy shape moments and higher order PSF anisotropy as well as isotropic smearing (Okura et al., 2008). However strong assumptions on the PSF shape have to be employed (i.e. the PSF is described by an isotropic kernel and a small anisotropic part) and moreover this calculation shows that up to 8-moments of the light distribution have to be measured in order to compute the required corrections. Computation of such high moments might strongly limit the effective number of galaxies usable for flexion measurement, since high signal to noise is required. Another possibility, which has been investigated in the last years, is to extend the shapelets formalism for flexion measurements (Massey et al., 2007b). The main advantage of shapelets is that an exact PSF deconvolution can be done. However it has been shown that circular shapelets provide biased shear estimator if the shape to be described is steeper than a gaussian. The same problem might arise also for flexion estimator (Melchior et al., 2010a).

In chapter 5 we will present a new method, based of moment measurements but employing an exact PSF deconvolution, which might be very useful for future flexion measurements.

Apri la mente a quel ch'io ti paleso
e fermalvi entro; ché non fa scienza,
sanza lo ritenere, avere inteso.[0]

Dante (1265-1321) Paradiso V

4

Bias in, and correction to KSB shear measurements

One of the most popular method to estimate gravitational shear from surface-brightness moments of small, convolved and noisy galaxy images is KSB (Kaiser et al., 1995; Luppino and Kaiser, 1997; Hoekstra et al., 1998). It derives galaxy ellipticites from the weighted second moment of the observed images, and then gives an approximate correction for the effect of the weighting function and for the effect of the PSF. The main advantage of KSB is that it is easy to implement and it is very fast (which is an important requirement specially for cosmic shear survey, where million of galaxies have to be analysed). However its mathematical derivation relies on three potentially problematic assumptions. These are:

- While gravitational shear must be estimated from averaged galaxy images, KSB derives a shear estimate from each individual image and then takes the average. Since the two operations do not commute, KSB gives biased results.
- KSB implicitly assumes that galaxy ellipticities are small, while weak gravitational lensing assures only that the change in ellipticity due to the shear is small.
- KSB does not invert the convolution with the point-spread function, but gives an approximate PSF correction which – even for a circular PSF – holds only in the limit of circular sources.

In this chapter we quantitatively demonstrate the biases due to all assumptions, extend the KSB approach consistently to third order in the shear and ellipticity and show that this extension lowers the biases substantially. The issue of proper PSF deconvolution will be addressed the next chapter.

[0]Open your mind to what I shall disclose,/and hold it fast within you; he who hears,/but does not hold what he has heard, learns nothing.

4.1 Standard KSB

We review in this section the standard KSB formalism, neglecting, for the moment, PSF convolution. Any measurements of moments has to incorporate a weighting function in order to suppress the pixel noise dominating at large spatial scales. The presence of weighting changes the definition of ellipticity given in equation 3.10 to:

$$\chi_\alpha = \frac{1}{Tr(Q)} \int \mathrm{d}^2\theta I^{\mathrm{obs}}(\vec{\theta}) \eta_\alpha W\left(\frac{|\vec{\theta}|^2}{\sigma^2}\right) , \tag{4.1}$$

with

$$\eta_\alpha = \begin{cases} \theta_1^2 - \theta_2^2 & \text{if} \quad \alpha = 1 \\ 2\theta_1\theta_2 & \text{if} \quad \alpha = 2 \end{cases} . \tag{4.2}$$

Note that also TrQ in equation 4.1 is evaluated using weighted moments. Using equation 2.21, neglecting the flexion terms, and the conservation of the surface brightness, $I^{\mathrm{obs}}(\vec{\theta}) = I^{\mathrm{s}}(A\vec{\theta})$, we can infer the surface brightness in the source plane. From its second moments,

$$\begin{aligned} Q^{\mathrm{s}}_{ij} &= \int \mathrm{d}^2\beta I^{\mathrm{s}}(\vec{\beta}) \beta_i \beta_j W\left(\frac{|\vec{\beta}|^2}{\hat{\sigma}^2}\right) \\ &= (\det A) A_{ik} A_{il} \int \mathrm{d}^2\theta I^{\mathrm{obs}}(\vec{\theta}) \theta_k \theta_l \\ &\times W\left(\frac{(|\vec{\theta}|^2 - 2\eta_\alpha g^\alpha + |\vec{\theta}|^2|g|^2)}{\sigma^2(1+|g|^2)}\right) , \end{aligned} \tag{4.3}$$

we form the ellipticity

$$\chi^{\mathrm{s}}_\alpha = C \int \mathrm{d}^2\theta I^{\mathrm{obs}}(\vec{\theta}) \xi_\alpha W\left(\frac{|\vec{\theta}|^2 - 2\eta_\beta g^\beta + |\vec{\theta}|^2|g|^2}{\sigma^2(1+|g|^2)}\right) , \tag{4.4}$$

where

$$C = \frac{(\det A)(1-\kappa)^2}{Tr(Q^{\mathrm{s}})} \text{ and} \tag{4.5}$$

$$\xi_\alpha = \eta_\alpha - 2g_\alpha|\vec{\theta}|^2 + (-1)^\alpha \eta_\alpha (g_1^2 - g_2^2) + 2g_1 g_2 \eta^\dagger_\alpha . \tag{4.6}$$

The relation between the two filter scales in equation 4.3 is given by $\hat{\sigma}^2 = (1-\kappa)^2(1+|g|^2)\sigma^2$ and the multiplicative term $(\det A)(1-\kappa)^2$ in equation 4.5 will cancel out once $Tr(Q^{\mathrm{s}})$ is written in terms of $Tr(Q)$. Note that Einstein's sum convention is not implied in $(-1)^\alpha\eta_\alpha$, and that

$$\eta^\dagger_\alpha = \begin{cases} \eta_2 & \text{if} \quad \alpha = 1 \\ \eta_1 & \text{if} \quad \alpha = 2 \end{cases} . \tag{4.7}$$

We adopt this notation for a general tensor,

$$\Omega^{\dagger}_{\alpha\beta\ldots\zeta} = \begin{cases} \Omega_{2\beta\ldots\zeta} & \text{if} \quad \alpha = 1 \\ \Omega_{1\beta\ldots\zeta} & \text{if} \quad \alpha = 2 \end{cases} \tag{4.8}$$

Combining equations 4.1 and 4.4 gives a more complicated relation between ellipticities in the source and in the lens planes than equation 3.6 due to the presence of the weight function. Keeping only first-order terms in g, this relation is

$$\chi_\alpha - \chi^{\rm s}_\alpha = g^\beta P^{\rm sh}_{\alpha\beta}, \tag{4.9}$$

(Kaiser et al., 1995; Hoekstra et al., 1998) with

$$P^{\rm sh}_{\alpha\beta} = -2\frac{\chi_\alpha L_\beta}{Tr(Q)} - 2\chi_\alpha\chi_\beta + 2\frac{B_{\alpha\beta}}{Tr(Q)} + 2\delta_{\alpha\beta} \tag{4.10}$$

and

$$\begin{aligned} L_\beta &= \frac{1}{\sigma^2}\int \mathrm{d}^2\theta I^{\rm obs}(\vec{\theta}) W' |\vec{\theta}|^2 \eta_\beta \,, \\ B_{\alpha\beta} &= \frac{1}{\sigma^2}\int \mathrm{d}^2\theta I^{\rm obs}(\vec{\theta}) W' \eta_\alpha \eta_\beta \,. \end{aligned} \tag{4.11}$$

The notation we use here follows Bartelmann and Schneider (2001).

4.1.1 Shear estimates in KSB

Equation 4.9 directly relates the measured weighted ellipticity χ to the shear g if the intrinsic ellipticity of the source $\chi^{\rm s}$ is known. Since χ and $\chi^{\rm s}$ cannot be disentangled for individual galaxies, averages over ensembles of images are necessary to estimate g,

$$\langle\chi_\alpha\rangle - \langle\chi^{\rm s}_\alpha\rangle = \langle g^\beta P^{\rm sh}_{\alpha\beta}\rangle \rightarrow \langle g_\alpha\rangle = g_\alpha = \langle P^{\rm sh}\rangle^{-1}_{\alpha\beta}\langle\chi^\beta\rangle \,. \tag{4.12}$$

The original KSB method actually performs the average of $P^{\rm sh}$, but this requires all source characteristics like apparent size and morphology to be locally constant. When considering convolution with the telescope's PSF (see section 4), this argument also applies to the shape of the PSF. Since generally the PSF shapes are not sufficiently stable across different areas of the image or even different observations, it is common – particularly for cosmic shear applications – to interchange the averages,

$$\langle\tilde{g}_\alpha\rangle = \langle(P^{\rm sh})^{-1}_{\alpha\beta}\chi^\beta\rangle \,, \tag{4.13}$$

Erben et al. (2001), assuming that $\langle(P^{\rm sh})^{-1}\chi^{\rm s}\rangle = 0$. This condition is not guaranteed since $P^{\rm sh}$ itself depends on χ. The symbol $\tilde{g}_\alpha$ in equation 4.13

denotes the shear estimate obtained by solving equation 4.9 with $\chi^s = 0$. We introduce it since $\tilde{g}$ is not the true shear (which is inaccessible for a single galaxy), but the shear one would measure if the source was circular. The true shear g is then sought by averaging $\tilde{g}$. Equation (3.6) shows that for $\chi^s = 0$ and $W(x) = 1$, $\langle\tilde{g}\rangle$ is related to χ by

$$\langle\tilde{g}\rangle = \left\langle \frac{1-\sqrt{1-\chi^2}}{\chi} \right\rangle \simeq \left\langle \frac{\chi}{2} + \frac{\chi^3}{8} + \frac{\chi^5}{16} + ... \right\rangle \ . \tag{4.14}$$

In general, $\langle\tilde{g}\rangle$ differs from the true shear g computed in equation 3.13.

Assuming that $g \ll 1$, meaning $\langle\chi\rangle \ll 1$, and the distribution of the intrinsic ellipticities to be Gaussian with standard deviation σ_χ, the difference can be written as:

$$g - \langle\tilde{g}\rangle \simeq \frac{\langle\chi\rangle}{2}\left(\frac{\sigma_\chi^2}{1-\sigma_\chi^2}\right) - \frac{3\sigma_\chi^2\langle\chi\rangle}{8} \tag{4.15}$$

from which

$$\langle\tilde{g}\rangle \simeq g\left(1 - \frac{1}{4}\sigma_\chi^2\right) \ . \tag{4.16}$$

For a realistic $\sigma_\chi \simeq 0.3$, the bias introduced by averaging shear estimates instead of ellipticities is $\approx 2\%$.

Moreover, averaging shear estimates does not allow one to assume that $\tilde{g}$ is small, as done in the original derivation of $P^{\rm sh}$, since it is always of the same magnitude as χ. In coordinates rotated such that $\tilde{g}$ has only one non-vanishing component, and in absence of a weight function, the relation between χ and $\tilde{g}$ provided by KSB[1] in equation 4.9 is

$$\tilde{g}^{\rm KSB} \simeq \frac{\chi_1}{2} + \frac{\chi_1^3}{2} + \frac{\chi_1^5}{2} + ... \ . \tag{4.17}$$

Obviously, this is correct only to lowest order. Comparing Eqs. (4.14) and (4.17), the error made by KSB in the shear estimation is a function of the measured ellipticity and scales as $(3\chi^3/8 + 7\chi^5/16)$. Typically, $|\chi| \in [0.5...0.8]$, implying that the bias KSB introduces in the shear estimate (without weight function) is in the range $[6...33]\%$. The reason for this bias comes from the fact that second- or higher-order terms in g have been neglected in the derivation of equation 4.9, while terms like $\chi^2 g$ have been kept. Once g is identified with $\tilde{g}$, these mixed terms are effectively of the same order as the g^3 terms. In a consistent first-order relation between

[1]Here and throughout this chapter the notation *KSB* refers to the solution of any equation following from equation 4.13. In applications to real data $P^{\rm sh}$ has been treated however in many different ways by different authors. We refer to Heymans et al. (2006) for a complete overview.

χ and $\tilde{g}$, only the first-order term in χg can be considered. Then, $P^{\rm sh}_{\alpha\beta}$ looks like

$$P^{\rm sh,(0)}_{\alpha\beta} = \frac{2B_{\alpha\beta}}{TrQ} + 2\delta_{\alpha\beta} \; . \tag{4.18}$$

We shall refer to this approximation as KSB1. In this case, the solution for $\tilde{g}$ is

$$\tilde{g}^{\rm KSB1} = \frac{\chi}{2} \; . \tag{4.19}$$

The error on the shear estimate made by KSB1 scales like $(-\chi^3/8 - \chi^5/16)$, leading to an underestimate which is considerably smaller than the overestimate given by KSB. However, as discussed before, χ is practically never small, meaning that first-order approximations may be poor.

In a frequently used variant of KSB, $P^{\rm sh}_{\alpha\beta}$ is approximated by half its trace (KSBtr hereafter),

$$P^{\rm sh}_{\alpha\beta} \simeq \frac{1}{2} Tr(P^{\rm sh}_{\alpha\beta})\delta_{\alpha\beta} \; . \tag{4.20}$$

This is usually justified saying that the trace is less noisy than the inverse of the full tensor, as we shall show in Sect. 3.3. This statement is certainly correct for large ellipticities. However, it turns out to work much better than the full tensor even in the absence of noise, PSF and weighting. The reason is that it leads to the relation

$$\tilde{g}^{\rm KSBtr} \simeq \frac{\chi}{2} + \frac{\chi^3}{4} + \frac{\chi^5}{8} + ... \tag{4.21}$$

between $\tilde{g}$ and χ, which biases the shear estimate by $\chi^3/8 + \chi^5/16$.

We can summarise the preceding discussion as follows:

1. KSB incorrectly approximates equation 3.6;
2. KSB1 is mathematically consistent;
3. KSBtr approximates equation 3.6 better even though it lacks mathematical justification;
4. No KSB variant discussed so far is correct to third order in χ.

4.1.2 Third-order relation between g and χ

We now derive a consistent third-order relation between χ and $\tilde{g}$, including the effects of the weight function. We follow closely the approach in Sect. 4.6.2 of Bartelmann and Schneider (2001), and use Einstein's sum

convention. We start from equation 4.4 and Taylor-expand the weight function around $g = 0$ to third order in g,

$$\begin{aligned} & W\left(\frac{(|\vec{\theta}|^2 - 2\eta_\alpha g^\alpha + |\vec{\theta}|^2|g|^2)}{\sigma^2(1+|g|^2)}\right) \simeq \\ & W\left(\frac{|\vec{\theta}|^2}{\sigma^2}\right) - 2W'\left(\frac{|\vec{\theta}|^2}{\sigma^2}\right)\frac{\eta_\beta g^\beta(1-|g|^2)}{\sigma^2} + \\ & 2W''\left(\frac{|\vec{\theta}|^2}{\sigma^2}\right)\frac{(\eta_\beta g^\beta)^2}{\sigma^4} - \frac{4}{3}W'''\left(\frac{|\vec{\theta}|^2}{\sigma^2}\right)\frac{(\eta_\beta g^\beta)^3}{\sigma^6} + \mathcal{O}(g^4), \end{aligned} \tag{4.22}$$

where

$$\frac{\eta_\beta g^\beta}{(1+g^2)} \simeq \eta_\beta g^\beta(1-g^2) + \mathcal{O}(g^4) \tag{4.23}$$

was used. Note that the derivatives of the weight function are taken with respect to θ^2. Truncating the series at a given order implies that the final result will depend on the shape of the weight function.

We proceed with the calculation of $\chi^{\rm s}_\alpha Tr(Q^{\rm s})$ to third order in χg,

$$\begin{aligned} & \frac{\chi^{\rm s}_\alpha Tr(Q^{\rm s})}{(\det A)(1-\kappa)^2} = \int {\rm d}^2\theta \xi_\alpha I(\vec{\theta}) W\left(\frac{|\vec{\theta}|^2 - 2\eta_\beta g^\beta + |\vec{\theta}|^2 g^2}{\sigma^2}\right) = \\ & \chi_\alpha Tr(Q) - 2g^\beta B_{\alpha\beta} + 2g^\beta g^\gamma D_{\alpha\beta\gamma} - 2g_\alpha Tr(Q) + 4g_\alpha g^\beta L_\beta + \\ & - 4K_{\beta\gamma}g_\alpha g^\beta g^\gamma + (-1)^\alpha(g_2^2 - g_1^2)\chi_\alpha Tr(Q) \\ & - 2(-1)^\alpha B_{\alpha\beta}(g_2^2 - g_1^2)g^\beta + 2g_1 g_2 \chi^\dagger_\alpha Tr(Q) + \\ & - 4B^\dagger_{\alpha\beta} g^\beta g_1 g_2 - \frac{4}{3}U_{\alpha\beta\gamma\delta}g^\beta g^\gamma g^\delta + \mathcal{O}(g^4), \end{aligned} \tag{4.24}$$

where the definitions

$$\begin{aligned} D_{\alpha\beta\gamma} &= \frac{1}{\sigma^4}\int {\rm d}^2\theta I^{\rm obs}(\vec{\theta}) W'' \eta_\alpha\eta_\beta\eta_\gamma \,, \\ U_{\alpha\beta\gamma\delta} &= \frac{1}{\sigma^6}\int {\rm d}^2\theta I^{\rm obs}(\vec{\theta}) W''' \eta_\alpha\eta_\beta\eta_\gamma\eta_\delta \end{aligned} \tag{4.25}$$

appear. L_α and $B_{\alpha\beta}$ are given in equation 4.11. In the same way, we evaluate

$$\begin{aligned} & \frac{Tr(Q^{\rm s})}{(\det A)(1-\kappa)^2} \simeq Tr(Q)(1+|g|^2) - 2g^\alpha L_\alpha + 2g^\alpha g^\beta K_{\alpha\beta} - \\ & 2g^\alpha \chi_\alpha Tr(Q) + 4g^\alpha g^\beta B_{\alpha\beta} - 4D_{\alpha\beta\gamma}g^\alpha g^\beta g^\gamma - \frac{4}{3}J_{\alpha\beta\gamma}g^\alpha g^\beta g^\gamma \\ & = Tr(Q)(1+f(g)), \end{aligned} \tag{4.26}$$

where we implicitly defined $f(g)$ and

$$\begin{aligned} K_{\alpha\beta} &= \frac{1}{\sigma^4}\int \mathrm{d}^2\theta I^{\mathrm{obs}}(\vec{\theta})W''|\vec{\theta}|^2\eta_\alpha\eta_\beta\,, \\ J_{\alpha\beta\gamma} &= \frac{1}{\sigma^6}\int \mathrm{d}^2\theta I^{\mathrm{obs}}(\vec{\theta})W'''|\theta|^2\eta_\alpha\eta_\beta\eta_\gamma\,. \end{aligned} \tag{4.27}$$

From these quantities, we compute

$$\chi_\alpha - \chi^{\mathrm{s}}_\alpha = \frac{\chi_\alpha Tr(Q)(1+f(g)) - \chi^{\mathrm{s}}_\alpha Tr(Q^{\mathrm{s}})}{Tr(Q)(1+f(g))}. \tag{4.28}$$

This equation holds exactly in absence of a weight function. If a weight function is included, $f(g)$ is at most of order 0.02, and we shall consider equation 4.28 exact to third order. After some algebra we find

$$\boxed{\chi_\alpha - \chi^{\mathrm{s}}_\alpha = \frac{g^\beta[P_{\alpha\beta} + g^\gamma(R_{\alpha\beta\gamma} + g^\delta S_{\alpha\beta\gamma\delta})] + \Xi_\alpha + \mathcal{O}(g^4)}{1+f(g)}} \tag{4.29}$$

where

$$\begin{aligned} R_{\alpha\beta\gamma} &= 2\frac{\chi_\alpha K_{\gamma\beta}}{Tr(Q)} + 4\frac{\chi_\alpha B_{\gamma\beta}}{Tr(Q)} - 2\frac{D_{\alpha\beta\gamma}}{Tr(Q)} - 4\frac{\delta_{\alpha\gamma}L_\beta}{Tr(Q)}\,, \\ S_{\alpha\beta\gamma\lambda} &= \frac{2K_{\beta\gamma}\delta_{\alpha\lambda}}{TrQ} + \frac{4}{3}\frac{U_{\alpha\beta\gamma\lambda}}{TrQ}\,, \end{aligned} \tag{4.30}$$

and

$$\begin{aligned} \Xi_\alpha = &\left(\chi_\alpha - \frac{2B_{\alpha\beta}g^\beta}{TrQ}\right)|g|^2 - (-1)^\alpha(g_2^2 - g_1^2)\left(\chi_\alpha - \frac{2B_{\alpha\beta}g^\beta}{TrQ}\right) - \\ &2g_1g_2\left(\chi^\dagger_\alpha - \frac{2B^\dagger_{\alpha\beta}g^\beta}{TrQ}\right) \end{aligned} \tag{4.31}$$

Introducing second and third-order terms leads to a non-linear relation between χ and g which needs to be solved numerically. Moreover, sixth-order moments of the observed surface-brightness distribution appear in $R_{\alpha\beta\gamma}$ and eight-order moments in $U_{\alpha\beta\gamma\delta}$ because of the Taylor expansion of the weight function to third order. We discuss in the following Section how to deal with the non-linear relation between shear and ellipticity and possible noise issues due to the appearance of higher moments.

4.1.3 Tests

We now show the results of simple tests carried out to check how well the four variants of KSB estimate the shear. We consider a circular source

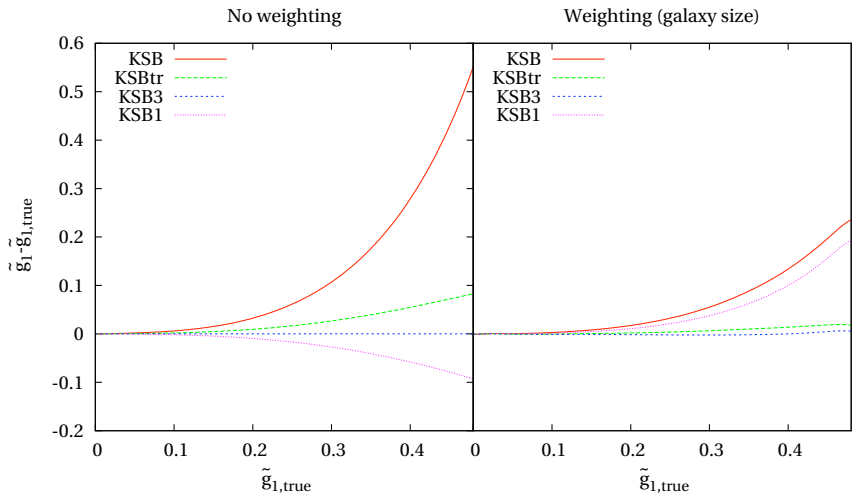

Figure 4.1: Shear estimate $\tilde{g}_1$ as a function of the applied shear for noise-free and unconvolved Sérsic-type galaxy images as provided by KSB (red line), KSBtr (green line), KSB3 (blue line), and KSB1 (magenta line). In the *left panel* no weighting function has been used to measure moments of the light distribution, while in the *right panel* a Gaussian weighting function has been employed with a width equal to the size of the object. The effective galaxy radius was $R_e = 2$ pixel, the Sérsic model was tenfold oversampled, and the image side-length was 40 pixels.

($\chi^s = 0$) with a Sérsic brightness profile, as defined in equation 3.38 with $n_s = 1.5$, which represents the average value for rather bright galaxies in the COSMOS field (Sargent et al., 2007). We shear this profile by a variable amount $\tilde{g}_1$, keeping $\tilde{g}_2 = 0.1$ fixed, using equation 2.21. Flexion is assumed to vanish in these tests. For all following tests, the effective galaxy radius was $R_e = 2$ pixels, the Sérsic model was tenfold oversampled, and the image side-length was set such as to not truncate the galaxy at the image boundary. Then, we measure the ellipticity as defined in equation 3.10. Since the model galaxy is intrinsically circular, the source ellipticity is entirely generated by the applied shear which is varied in a wide range such as to mimic the intrinsic ellipticity dispersion. The weight function has been chosen as Gaussian with $\sigma = 2R_e$. We repeated this test assuming a flat weight function ($W(x) = 1$) in order to estimate how much the different approximations in deriving $P^{\rm sh}$ affect the measurement. The results are shown in figure 4.1.

In absence of a weight function (left panel of figure 4.1), the performance of the four variants closely follows the analytic behaviour worked out in section 4.1 and 4.1.1: KSB severely overestimates the shear for large $\tilde{g}_1$, while KSBtr and KSB1 better approximate the shear. KSB3 returns the correct shear under this condition.

The weight function renders the image more circular and thus reduces the measured χ. This means that the high-order terms in χ contribute less to the shear estimate. Therefore, the deviation from the correct result is significantly lower for all the methods (right panel of figure 4.1). This is not true for KSB1, which allows only a first-order correction for the weight function.

We also investigate the behaviour of the four KSB variants for realistic pixel noise. The average result for 100 galaxies is shown in figure 4.2.

KSBtr is the only method for which no matrix inversion is required. It is thus not surprising that it exhibits the lowest standard deviation for all values of $\tilde{g}$. KSB and KSB3 have a comparable amount of noise even though KSB3 involves the computation of 6th and 8th moments of the light distribution. The reason is that these higher-order moments are computed using the second and third derivatives of the weight function. There is no price to be payed (in terms of measurement noise) in using KSB3 instead of the simple KSB description. We also investigate how much the measurement of one component of the shear is affected by the value of the other component. For this case, we also studied the case of unweighted and weighted moment measurements. The result is shown in figure 4.3. The obvious cross-talk between the two components is not surprising for KSB, KSBtr or KSB1 since all terms which mix $\tilde{g}_1$ and $\tilde{g}_2$ were neglected

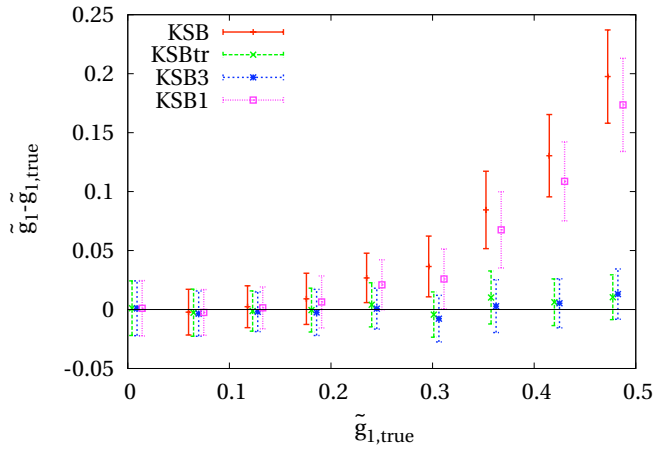

Figure 4.2: Shear estimate $\tilde{g}_1$ as a function of the applied shear for noisy but unconvolved Sérsic-type galaxy images as provided by KSB (red line), KSBtr (green line), and KSB3 (blue line). The total flux of the source was fixed to unity, the noise rms to 10^{-3}. The average is taken over 100 objects. Errorbars denote standard deviation of the mean.

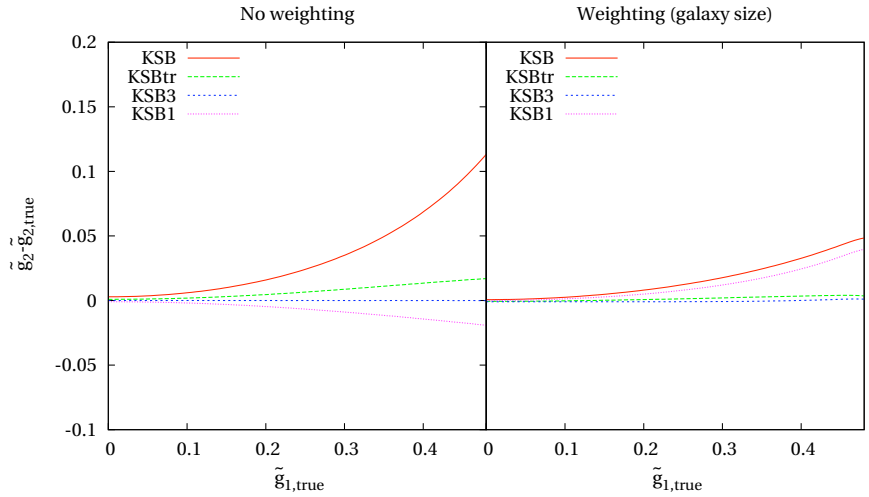

Figure 4.3: Shear estimation cross-talk for $\tilde{g}_2$ as a function of the applied shear $\tilde{g}_1$ for noise-free and unconvolved Sérsic-type galaxy images as provided by KSB (red line), KSBtr (green line), KSB3 (blue line), and KSB1 (magenta line). In the *left panel* no weighting function has been used to measure moments of the light distribution, while in the *right panel* a Gaussian weighting function has been employed with a width equal to the size of the object.

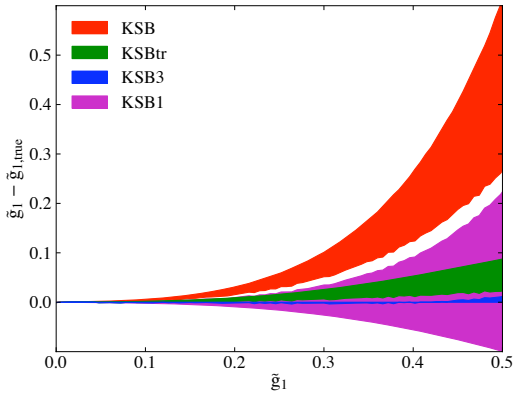

Figure 4.4: Dependence of the shear estimate $\tilde{g}_1$ on the size of the weighting function width as a function of the applied shear for noise-free and unconvolved Sérsic-type galaxy images as provided by KSB (red), KSBtr (green), KSB3 (blue), and KSB1 (magenta). We consider a Gaussian weighting function with width $\sigma = [2R_e, ..., \infty]$. The lower limits correspond to $\sigma = 2R_e$, and the upper limits are identical to the unweighted case shown in figure 4.1.

in the calculation. Introducing third-order corrections, the estimate of one shear component becomes almost independent of the other component.

Finally, we study how much the bias in the shear measurement depends on the width σ of the weight function W. We vary the width within $[2R_e, \infty)$. The result is shown in figure 4.4. KSB and KSB1 exhibit a strong dependence on σ, while KSBtr is more robust, and KSB3 is almost independent of σ. Due to the poor correction of the weight-induced change of χ, KSB1 performs poorest in this test. For KSB, the reduction of χ due to the weighting limits its strong non-linear response such that the bias decreases for narrow weight functions. As KSB3 employs the best description of the weighting, it performs excellently in this test.

In all tests carried out so far, we have assumed that the intrinsic ellipticity of the object vanishes, $\chi^s = 0$. This is of course idealised since galaxies have an intrinsic ellipticity dispersion. In order to test the performance of the four methods for an isotropic source-ellipticity distribution, we apply the so-called *ring test* (Nakajima and Bernstein, 2007). We construct an ensemble of test galaxies falling on a circle in the ellipticity plane, shear them, measure their shapes, and take the mean. We choose an intrinsic ellipticity $|\chi^s| = 0.3$ and apply the shear $g = (0.1, 0.05)$. The result is shown in figure 4.5. A perfect method would recover the correct shear after averaging over all test galaxies. Not surprisingly, we find that KSB is unable to recover the correct shear from the averaged individual shear

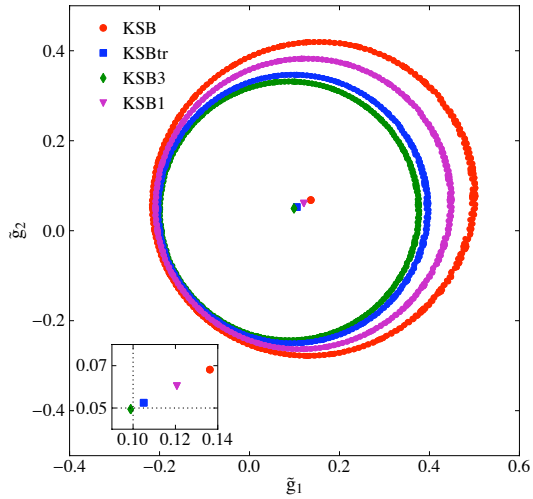

Figure 4.5: Shear estimates of a sample of Sérsic-type galaxies with $\chi^s = 0.3$ after shear $g = (0.1, 0.05)$ is applied. Red dots are the results from KSB, magenta dots from KSB1, blue dots from KSBtr, and green dots from KSB3. The dots in the centre show the position of the ensemble averages of the estimates. A zoom of the central region is shown in the small panel, where the intersection of the dotted lines indicates the outcome of a perfect measurement.

estimates since they depend non-linearly on χ. This leads to an average overestimate of $\approx 35\,\%$ if the shear is aligned with the intrinsic ellipticity. As the other variants have lower non-linear error in the χ-g relation, the mean values are biased by $\approx 20\,\%$ (KSB1), $\approx 5\,\%$ (KSBtr) and $\approx 1\,\%$ (KSB3).

4.2 PSF convolution

Any measured galaxy's ellipticity is the result of three distinct physical processes: intrinsic ellipticity, lensing, and PSF convolution. As discussed above, lensing maps the galaxy's light distribution from the source to the lens plane, distorting its shape. The relation between galaxy ellipticity and shear can be found solving equation 3.6 if there is no weight function, or equation 4.29 if weighted moments are used to define the ellipticity. In general, the equation one needs to solve to relate ellipticity to a shear estimator $\tilde{g}$ has the implicit form

$$\chi = f(\tilde{g}, \chi)\,. \tag{4.32}$$

On the other hand, PSF deconvolution maps the observed ellipticity from the image plane (on which the object is lensed and convolved with the PSF) to the lens plane (on which the object is lensed only)

$$\chi = h(\chi^{\rm obs}) \; . \tag{4.33}$$

Thus, the relation between observed ellipticity and the shear estimator in presence of PSF convolution is the solution of

$$\chi^{\rm obs} = h^{-1}[f(\tilde{g}, h(\chi^{\rm obs}))] \; . \tag{4.34}$$

If the PSF is perfectly circular, the only effect of h is a circularisation of the object, otherwise the PSF induces additional anisotropic distortions. Therefore, it is crucial to properly correct these two effects in order to reliably estimate the shear. We consider in the following the case of a spherical PSF and briefly discuss the case of an anisotropic PSF in Sect. 4.2.1.

Instead of carrying out a proper PSF deconvolution first and then estimating the shear using the unconvolved ellipticity, as summarised by equation 4.34, KSB links the observed ellipticity to the shear by the following approach:

$$\chi_\alpha^{\rm obs} = \chi_\alpha^{\rm sh} - \chi_\alpha^{\rm g}, \tag{4.35}$$

where $\chi_\alpha^{\rm sh}$ is given by equation 4.29, and $\chi^{\rm g}$ is

$$\chi_\alpha^{\rm g} = P_{\alpha\gamma}^{\rm sm} (P^{\rm sm,*})^{-1}_{\gamma\beta} \chi_\beta^{\rm sh,*}. \tag{4.36}$$

$P^{\rm sm}$ is the so-called "smear polarisability tensor" and has the form

$$P_{\alpha\beta}^{\rm sm} = \frac{1}{Tr(Q)} \left[\left(M + \frac{2Tr(Q')}{\sigma^2} \right) \delta_{\alpha\beta} + G_{\alpha\beta} - \chi_\alpha (2F_\beta + L'_\beta) \right], \tag{4.37}$$

where

$$\begin{aligned} M &= \int {\rm d}^2\theta I(\vec{\theta}) W \left(\frac{|\vec{\theta}|^2}{\sigma^2} \right), \\ F_\alpha &= \frac{1}{\sigma^2} \int {\rm d}^2\theta I(\vec{\theta}) W' \left(\frac{|\vec{\theta}|^2}{\sigma^2} \right) \eta_\alpha, \quad \text{and} \\ G_{\alpha\beta} &= \frac{1}{\sigma^4} \int {\rm d}^2\theta I(\vec{\theta}) W'' \left(\frac{|\vec{\theta}|^2}{\sigma^2} \right) \eta_\alpha \eta_\beta. \end{aligned} \tag{4.38}$$

L'_α has to be interpreted as L_α calculated with the second derivative of the weight function, while $Tr(Q')$ and $Tr(Q)$ are calculated with the first derivative of the weight function. We refer to Sect. 4.6.2 of Bartelmann and Schneider (2001) for a complete derivation of equation 4.35.

Since $\chi^{\rm sm}$ encodes the action of lensing (cf. last Section on the appropriate forms of this mapping), we can rewrite equation 4.35 as

$$\chi^{\rm obs} = f(\tilde{g}, \chi^{\rm obs}) - \chi^{\rm g}(\tilde{g}, \chi^{\rm obs}). \tag{4.39}$$

It is important to note that the lensing-induced mapping is now evaluated with the observed, i.e. convolved, ellipticity instead of the unconvolved ellipticity. This approach therefore requires the correction term $\chi^{\rm g}$, which corresponds to a correct treatment of the PSF convolution (equation 4.34) if and only if

$$\chi^{\rm g}(\tilde{g}, \chi^{\rm obs}) = f(\tilde{g}, \chi^{\rm obs}) - h^{-1}[f(\tilde{g}, h(\chi^{\rm obs})]. \tag{4.40}$$

We study now a very simple but instructive case. We assume a perfectly circular source, no weight function, an isotropic PSF, and shear oriented in a single direction. Then, $P^{\rm sm}_{\alpha\beta}$ becomes diagonal,

$$P^{\rm sm}_{\alpha\beta} = \frac{M}{TrQ}\delta_{\alpha\beta}\ . \tag{4.41}$$

In the next chapter we shall demonstrate how to do a proper PSF deconvolution, using the moments of the PSF and the convolved object, and show that the mapping h between the convolved ellipticity $\chi^{\rm obs}$ and the unconvolved ellipticity $\tilde{\chi}$ in the lens plane is given by[2]

$$h(\chi^{\rm obs}) = \tilde{\chi} = \frac{\chi^{\rm obs}}{1 - A(\chi^{\rm obs})}, \tag{4.42}$$

where

$$A = \frac{M}{TrQ}\frac{TrQ^*}{M^*} \tag{4.43}$$

is a function of the observed ellipticity (as shown in figure 4.6) and of the size of the PSF (as shown in figure 4.7), and is bound to $[0, 1]$. If the shear has a single component and there is no weight function involved in the measurement, $f(\tilde{g}, \chi^{\rm obs})$ is

$$f(\tilde{g}, \chi^{\rm obs}) = \frac{2\tilde{g} - 2(\chi^{\rm obs})^2\tilde{g}}{1 + \tilde{g}^2 - 2\tilde{g}\chi^{\rm obs}} \tag{4.44}$$

According to equation 4.36, in the KSB formalism $\chi^{\rm g}$ has the form:

$$\chi^{\rm g}(\tilde{g}, \chi^{\rm obs}) = A(\chi^{\rm obs}) f(\tilde{g}, 0). \tag{4.45}$$

In particular, in standard KSB, $\chi^{\rm g}(\tilde{g}, \chi^{\rm obs}) = 2\tilde{g}A(\chi^{\rm obs})$.

[2] In order to derive this equation have a look to Table 5.1

Substituting this expression for χ^g in the lhs of Eqs. (4.40), we can conclude that KSB gives a proper description of PSF deconvolution only if the function $f(\tilde{g}, \chi^{\rm obs})$ can be decomposed into a product of two functions, one depending on $\tilde{g}$ only and one on $\chi^{\rm obs}$ only. This is by no means guaranteed. A detailed analysis reveals that there are two limiting cases in which Eqs. (4.40) holds:

- The PSF width vanishes:
  $A(\chi^{\rm obs}) = \chi^g(\chi^{\rm obs}) = 0 \Rightarrow \chi^{\rm obs} = \chi$.
- The observed ellipticity vanishes.

While the first case is trivial (but irrelevant), the second case can only be realized – for any finite PSF width – by a conspiracy of intrinsic and lensing-induced ellipticity.

To study in detail the error commited by KSB in the attempts to correct for the PSF convolution, we solve equation 4.35 explicitly, employing the four variants $\chi^{\rm sh}$ of mapping χ onto $\tilde{g}$ presented in the previous Section,

$$\begin{aligned}
\tilde{g}^{\rm KSB} &\simeq \frac{\tilde{\chi}_0}{2} + \frac{\tilde{\chi}_0^2}{2}A'(0) + \\
&+ \frac{\tilde{\chi}_0^3}{2}[(1-A(0))(1+A''(0)/2) + A'(0)^2] \\
&+ \mathcal{O}(\tilde{\chi}_0^4) \\
\tilde{g}^{\rm KSB1} &= \frac{\tilde{\chi}}{2} \\
\tilde{g}^{\rm KSBtr} &\simeq \frac{\tilde{\chi}_0}{2} + \frac{\tilde{\chi}_0^2}{2}A'(0) + \\
&+ \frac{\tilde{\chi}_0^3}{4}[(1-A(0))(1+A''(0)) + 2A'(0)^2] \\
&+ \mathcal{O}(\tilde{\chi}_0^4) \\
\tilde{g}^{\rm KSB3} &\simeq \frac{\tilde{\chi}_0}{2} + \frac{\tilde{\chi}_0^2}{2}A'(0) + \\
&+ \frac{\tilde{\chi}_0^3}{8}[1 + 4A'(0)^2 + 2A''(0) - 2A(0)(2+A''(0))] \\
&+ \mathcal{O}(\tilde{\chi}_0^4)
\end{aligned} \tag{4.46}$$

where

$$\tilde{\chi}_0 \equiv \frac{\chi^{\rm obs}}{1-A(0)} \tag{4.47}$$

and $A'(0)$ and $A''(0)$ are the first and the second derivatives of $A(\chi^{\rm obs})$ computed for $\chi^{\rm obs} = 0$. If the PSF correction works perfectly, the relation

between $\tilde{\chi}$ and $\tilde{g}$ has the same form as the exact unconvolved solution of equation 3.13,

$$\tilde{g} \simeq \frac{\tilde{\chi}}{2} + \frac{\tilde{\chi}^3}{8} + \mathcal{O}(\tilde{\chi}^5). \tag{4.48}$$

We note first of all that equation 4.46 is written in terms of $\tilde{\chi}_0$, while equation 4.48 is written in terms of $\tilde{\chi}$, meaning that in general the solutions are different already at first order. However the error at first order ($\chi^{\rm obs} \ll 1$) is mostly of order 10^{-4} and therefore negligible. In the limit of a very wide PSF $A(\chi) \simeq A(0)$ we find the deviations from the exact solution $b = \tilde{g} - \tilde{g}^{\rm KSB...}$,

$$\begin{aligned} b^{\rm KSB} &= \frac{3-4A}{8}\tilde{\chi}^3 + \mathcal{O}(\tilde{\chi}^5) \\ b^{\rm KSB1} &= -\frac{\tilde{\chi}^3}{8} + \mathcal{O}(\tilde{\chi}^5) \\ b^{\rm KSBtr} &= \frac{1-2A}{8}\tilde{\chi}^3 + \mathcal{O}(\tilde{\chi}^5) \\ b^{\rm KSB3} &= -\frac{A}{2}\tilde{\chi}^3 + \mathcal{O}(\tilde{\chi}^5) \end{aligned} \tag{4.49}$$

It is worth noting that the PSF correction introduces a bias with preferred direction: Shear estimates decrease as the PSF width increases.

4.2.1 PSF anisotropy

An anisotropic PSF introduces spurious ellipticity in the image plane which must be corrected. The appropriate correction in KSB relies on the hypothesis that the PSF can be considered almost isotropic. This enables its decomposition into an isotropic part P^{iso} and an anisotropic part q,

$$P(\vec{\theta}) = \int \mathrm{d}^2\phi q(\vec{\phi}) P^{\rm iso}(\vec{\theta} - \vec{\phi}) \tag{4.50}$$

Even this decomposition can be problematic for certain PSFs (Kuijken, 1999b). For example, a PSF given by the sum of two Gaussians with constant ellipticity does not fulfill the equation above. Assuming that equation 4.50 is valid, one can find a relation, valid to first order in q, between the observed and the isotropic ellipticity,

$$\chi_\alpha^{\rm iso} = \chi_\alpha^{\rm obs} - (P_{\alpha\beta}^{\rm sm}) q^\beta \tag{4.51}$$

The term q_α, carrying information on anisotropies in the PSF, can be determined from the shape of stars using the fact that their isotropically smeared images have zero ellipticity ($\chi^{*,\rm iso} = 0$),

$$q_\alpha = (P^{*,\rm sm})^{-1}_{\alpha\beta} \chi^{*,\rm obs}_\beta \tag{4.52}$$

Once q has been determined, we can use equation 4.51 to compute the *isotropic* from the *observed* ellipticity. For a detailed calculation we refer again to (Bartelmann and Schneider, 2001). In the derivation, all the terms containing moments of q higher than the second have been neglected as well as quadratic and higher-order terms in q_{ij}. If one wants to extend this calculation to higher orders in q, derivatives of the observed surface brightness $I^{\rm obs}$ would appear in the calculation because the assumed equality to $I^{\rm iso}$ (hypothetical surface brightness for vanishing q) does not hold any more. The fact that derivatives of the observed profile need to be considered renders it practically impossible to incorporate higher-order corrections for q, since $I^{\rm obs}$ is a noisy quantity. This means that within the KSB framework it is not possible to correct properly for highly elliptical PSFs.

If the determination of q is wrong, so is the estimate of $\chi^{\rm iso}$ (the ellipticity of $I^{\rm iso}$), and the error will propagate to the final shear measurement in an almost unpredictable way (Erben et al., 2001; Kuijken, 1999b). This could happen if the anisotropy of the PSF is too large for a linear treatment, or if the PSF cannot be decomposed into an isotropic and an anisotropic part.

4.2.2 Tests

We perform the same tests as in the previous Section, but with an additional convolution with a Moffat-shaped PSF,

$$P(r) = (1 + \alpha r^2)^{-\beta}, \tag{4.53}$$

where

$$\alpha = \frac{2^{1/\beta - 1}}{(\mathrm{FWHM}/2)^2} \tag{4.54}$$

controls the size of the PSF and β regulates its steepness. In order to ensure vanishing flux at large radii, the PSF is truncated at 5 FWHM, and the appropriate value at that position is subtracted from $P(r)$.

We begin studying the case of a flat weight function, $W(x) = 1$, for which we derive the behaviour of the four KSB variants in equation 4.46. The key quantity for describing a spherical PSF is given by A as defined in equation 4.43, which is a function mainly of the PSF width and mildly of its steepness for a given galaxy (see figure 4.7). We investigate the performance of the four methods as a function of the shear for a fixed PSF width. We choose FWHM $= 0.5\ R_e$ and $\beta = 2$ to mimic a space-based observation, and FWHM $= 5\ R_e$ and $\beta = 5$ to mimic a ground-based observation. The results are shown in figure 4.9. In the first case, KSB3 gives the best result, while KSBtr is the best approximation in the second case, as expected from equation 4.49.

We next investigate the response of the four methods to the size of the PSF for a given $\tilde{g}$ (figure 4.8). We choose $\tilde{g}_1 = 0.4$ and $\tilde{g}_2 = 0.1$. As expected from equation 4.49, KSB, KSBtr and KSB1 have the same limit for large PSF ($A \to 1$), while the bias for KSB3 is the largest in the limit of a very wide PSF. As noted before, the PSF correction in all KSB variants introduces a negative bias which partly compensates (or even overcompensates) the overestimate by KSB and KSBtr from the lens mapping. Since KSB3 is essentially unbiased for unconvolved ellipticities, any PSF correction necessarily lowers the shear estimate.

Finally, we introduce the weight function into the moment measurement and study the response of the four methods in this situation. The result is shown in figure 4.10 for a space-based (left panel) and a ground-based observation (right panel). For narrow PSFs, the methods react on weighting as in the previous Section, where the PSF was neglected (see figure 4.4), while the response is milder for a wider PSF. For a narrow PSF, KSBtr and KSB3 are essentially unbiased, and KSBtr remains fairly unbiased when the PSF width increases. From the comparison between Figs. 4.9 and 4.10 we can infer the effect of weighting on the shear estimates. The biases of most methods are lowered because the ellipticity of the convolved source is lower, hence a circular weight function does not significantly affect the ellipticity measurement. However, in particular KSB1 shows concerning dependence on both the presence of a weighting function and the width of the PSF: Even though KSB1 seems fairly unbiased in the right panel of figure 4.10, other values of the width of the weight function would lead to less optimal results.

We are aware that our tests are of somewhat approximate nature in the sense that the characteristics of the simulated images only coarsely resemble that of realistic survey data. The real-life performance of all KSB variants will depend on peculiar properties of the surveys to be analyzed, such as the shape of the PSF, the depth of the observation, etc. However, two findings from our result can be considered robust: KSB3 shows the least amount of bias and the weakest dependence on the width of the weighting function, as long as the PSF remains narrow with respect to the galaxy size. KSBtr has a more pronounced dependence on the weighting function, but reacts only weakly on changes of the PSF width.

4.3 Conclusions

We have assessed the assumptions underlying the KSB method for measuring gravitational shear from the images of ensembles of lensed galaxies. KSB has the great advantage of being model-independent since it ex-

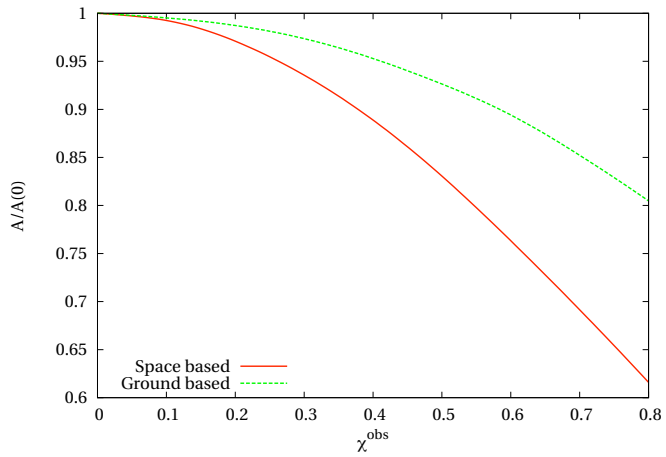

Figure 4.6: Dependence of A as defined in equation 4.43 on the observed ellipticity. Red line represents the case of PSF with FWHM $= 0.5R_e$ and $\beta = 2$ to mimic a space-based observation and the green line the case of a PSF with FWHM $= 5R_e$ and $\beta = 5$ to mimic a ground-based observation. In the case of a infinitely wide PSF we would have $A/A(0) = 1$ independently on the ellipticity.

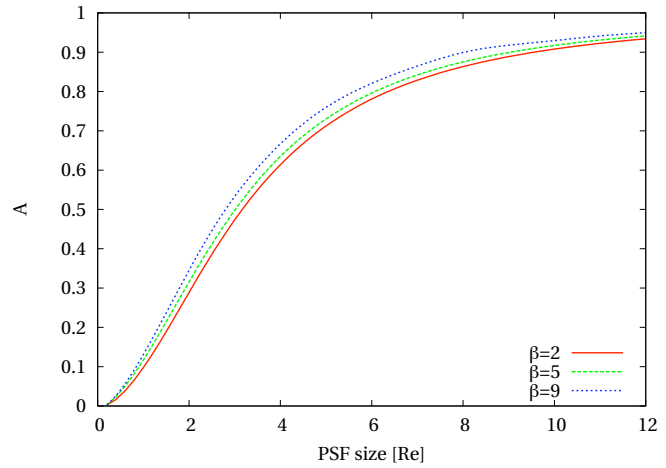

Figure 4.7: Dependence of A as defined in equation 4.43 on the size of the PSF for a fixed value of the observed ellipticity.

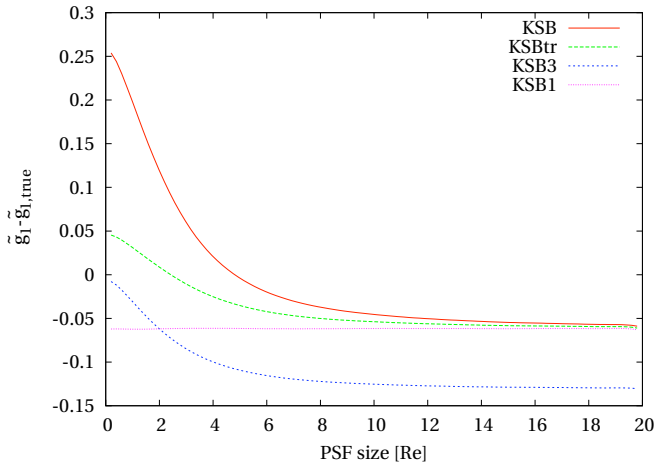

Figure 4.8: Shear estimate $\tilde{g}_1$ as a function of the PSF size for a Sérsic-type galaxy image as provided by KSB (red line), KSBtr (green line), KSB3 (blue line), and KSB1 (magenta line) for a fixed value of the pre-convolved ellipticity corresponding to $\tilde{g} = (0.4, 0.1)$).

presses the lensing-induced shape change by a combination of moments of the surface-brightness distribution. However, several assumptions underlying the derivation of the method and its practical implementations turn out to be violated more or less severely in realistic situations. We can summarise our results as follows:

1. KSB defines a shear estimate for each individual galaxy, defined as the shear that would describe the observed ellipticity if the object was perfectly circular prior to lensing. In other words, it is assumed that the intrinsic ellipticity of the individual object vanishes. The true shear is then computed averaging these shear estimates within a region where g is assumed to be constant. This is in general not equivalent to averaging the ellipticities of each individual object and then computing the true shear: averaging observed galaxy ellipticities and measuring the shear do not commute because not the individual intrinsic ellipticities can be assumed to vanish, but only their average. We show that the difference between the two approaches is a function of the variance of the intrinsic ellipticity distribution. The error introduced this way depends on the variants of KSB used, the size of the PSF, and the width of the weight function. It is normally in the percent range.

2. The definition of the KSB shear estimate relies on the assumption that the shear is small. However, this is only true after averaging.

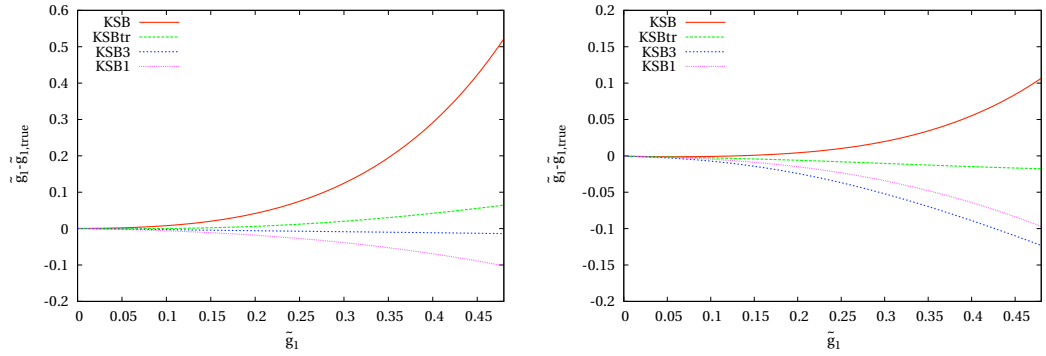

Figure 4.9: Shear estimate $\tilde{g}_1$ as a function of the applied shear for noise-free Sérsic-type galaxy images as provided by KSB (red line), KSBtr (green line), KSB3 (blue line), and KSB1 (magenta line). In the *left panel* we choose a PSF with FWHM $= 0.5R_e$ and $\beta = 2$ to mimic a space-based observation, while in the *right panel* we choose FWHM $= 5R_e$ and $\beta = 5$ to mimic a ground-based observation. No weight function has been used to compute moments.

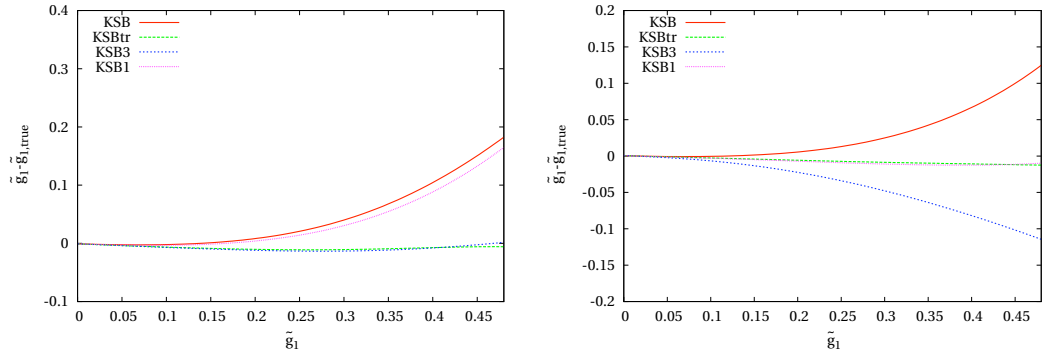

Figure 4.10: As in figure 4.9 but employing a weighting function in the moments computation. The width of the weighting function was set to the apparent size of the objects, $\sigma = \sqrt{Tr(Q)}$

For a single object, the reduced-shear estimate g is of the same order as the ellipticity χ. This leads to a relation between g and χ which is correct only to first order. This situation can be improved considering only linear terms in χg in the derivation of $P^{\rm sh}$ (KSB1), or considering consistently terms up to third order in χg (KSB3). We also show that the approximation of $P^{\rm sh}$ by half of its trace (KSBtr), although not mathematically justified, yields a better g-χ relation compared to KSB.

3. KSB, KSB1 and KSBtr in absence of PSF convolution tend to overestimate the shear, while KSB3 gives an almost perfect result.

4. KSB and KSB1 depend strongly on the width of the weight function used in the moment measurements, while KSBtr is more robust and KSB3 is almost independent of it.

5. KSB does not perform any PSF deconvolution, but gives only an approximate correction for the effects of the PSF. We show that this correction would be equivalent to a proper deconvolution from a circular PSF only in the case of a circular source, otherwise the improper PSF correction lowers the shear estimate.

6. The overestimate due to the wrong relation between g and χ and the underestimate due to the inappropriate PSF correction tend to compensate each other. For a narrow PSF (space-based observation), KSB3 is the variant with the least bias, while KSBtr is the best method for wider PSFs (ground-based observation).

7. The choice of the width σ of the weight function could be utilized to reduce the measurement bias. In principle, σ can be tuned according to the size of the PSF and to the galaxy ellipicities such that the shear estimate ends up to be almost unbiased. However, practically this is only feasible for the galaxy ensemble as a whole, whereas choosing σ such that shear estimates are unbiased for each individual galaxy is of similar difficulty as estimating the shear.

8. KSB can correct only small anisotropies in the PSF ($q \ll 1$). It is not possible to extend the formalism to allow more precise corrections since that would imply the calculation of derivatives of the observed surface brightness, which is not feasible since $I^{\rm obs}$ is a noisy quantity. An improper correction of the PSF anisotropy introduces a bias which propagates to the final measurement of the shear in an almost unpredictable way.

Per correr miglior acque alza le vele
omai la navicella del mio ingegno,
che lascia dietro a sé mar sì crudele [0]

Dante (1265-1321) Purgatorio I

5 Weak lensing with DEIMOS

We showed in the previous chapter how KSB relies on several assumptions concerning the relation between convolved and unconvolved ellipticity as well as the relation between ellipticity and shear, neither of which hold in practice. We proposed an extension of the original KSB method, namely KSB3, which gives more accurate shear estimations at least in the limit of small PSF. However we were not able to improve the KSB treatment of the PSF corrections. In this chapter we present a novel method, DEIMOS (DEconvolution In MOment Space), for shear (and flexion) estimation, which maintains the strengths of model-independent approaches by working with multipole moments, but does not suffer from the KSB-shortcomings mentioned above and in particular does not reley on any assumption about the shape of the PSF.

5.1 Notation

We introduce here a tensor-like notation to represent the moments of the brightness distribution $G(\vec{x})$ since it turns to be more convenient for the calculation we will present in this chapter:

$$\{G\}_{i,j} \equiv \int \mathrm{d}^2x \; G(\vec{x})\, x_1^i x_2^j, \tag{5.1}$$

The order of a moment is given by $n = i + j$. In this new notation the second moments Q_{11}, Q_{12}, Q_{22} reads as $\{G\}_{2,0}$, $\{G\}_{1,1}$, $\{G\}_{0,2}$.

[0] To course across more kindly waters now / my talent's little vessel lifts her sails / leaving behind herself a sea so cruel

5.2 The DEIMOS method

Any square-integrable one-dimensional function $G(x)$, has an exact representation in Fourier space,

$$G(x) \to \phi_G(k) = \int \mathrm{d}x\, G(x)\, e^{ikx}. \tag{5.2}$$

In the field of statistics, ϕ_G is often called the *characteristic function* of G and has a notable alternative form[1]

$$\phi_G(k) = \sum_n^\infty \{G\}_n \frac{(ik)^n}{n!}, \tag{5.3}$$

which provides a link between the Fourier-transform of G and its moments $\{G\}_n$, the one-dimensional pendants to Equation 5.1. We can now employ the convolution theorem, which allows us to replace the convolution by a product in Fourier-space, i.e. by a product of characteristic functions of G and of the PSF kernel P,

$$G^\star(x) \equiv \int \mathrm{d}x'\, G(x)\, P(x - x') \to \phi_{G^\star} = \phi_G \cdot \phi_P. \tag{5.4}$$

For convenience, we assume the PSF to be flux-normalized, $\{P\}_0 = 1$. Considering Equation 5.3, we get

$$\begin{aligned} \phi_{G^\star}(k) &= \Big[\sum_n^\infty \{G\}_n \frac{(ik)^n}{n!}\Big] \cdot \Big[\sum_n^\infty \{P\}_n \frac{(ik)^n}{n!}\Big] \\ &= \sum_n^\infty \sum_m^n \{G\}_m \frac{(ik)^m}{m!} \{P\}_{n-m} \frac{(ik)^{n-m}}{(n-m)!} \\ &= \sum_n^\infty \Big[\sum_m^n \binom{n}{m} \{G\}_m \{P\}_{n-m}\Big] \frac{(ik)^n}{n!}, \end{aligned} \tag{5.5}$$

where we applied the Cauchy product in the second step. The expression in square brackets on the last line is by definition the desired moment,

$$\{G^\star\}_n = \sum_m^n \binom{n}{m} \{G\}_m \{P\}_{n-m}. \tag{5.6}$$

Hence, we can now express a convolution of the function G with the kernel P entirely in moment space. Moreover, even though the series in Equation 5.3 is infinite, the order of the moments occurring in the computation of $\{G^\star\}_n$ is bound by n. This means, for calculating all moments

[1] The summation indices in this work all start with zero unless explicitly noted otherwise.

of $G^\star$ up to order n, the knowledge of the same set of moments of P and G is completely sufficient. This results holds for any shape of G and P as long as their moments do not diverge. For non-pathological distributions, this requirement does not pose a significant limitation.

In the case of two-dimensional functions the result presented in equation 5.6 can be generalised to:

$$\{G^\star\}_{i,j} = \sum_k^i \sum_l^j \binom{i}{k}\binom{j}{l}\{G\}_{k,l}\{P\}_{i-k,j-l}\,. \tag{5.7}$$

as also shown by Flusser and Suk (1998).

Deconvolution

To obtain the deconvolved moments required for the shear estimation via the ellipticity χ, we need to measure the moments up to second order of the convolved galaxy shape and of the PSF kernel shape. Then we can make use of a remarkable feature of Equation 5.7, which is already apparent from its form: Since $l + m = k < n$, the impact of convolution on a moment of order $i + j = n$ is only a function of moments of lower order. We can therefore start in zeroth order, the flux, which is not changed under convolution with a normalized kernel. With the accurate value of the zeroth order, we can infer the corrections to the first-order moments from the second line of Equation 5.7, and so on. The hierarchical build-up of the deconvolved moments is the heart of the DEIMOS method. For convenience, the set of equations, which need to be solved to obtain the deconvolved second-order moments, is shown in Table 5.1.

It is important to note and will turn out to be crucial for weak-lensing applications that with this deconvolution scheme we do not need to explicitly address the pixel noise, which hampers most other deconvolution approaches in the frequency domain, simply because we restrict ourselves to inferring the most robust low-order moments only.

5.3 Noise and weighting

In practice, the moments are measured from noisy image data,

$$I(\vec{x}) = G(\vec{x}) + N(\vec{x}), \tag{5.8}$$

where the noise N can be considered to be independently drawn from a Gaussian distribution with variance σ_n^2, i.e. $\langle N(\vec{x}_i)N(\vec{x}_j)\rangle = \sigma_n^2\delta_{ij}$ for any two positions $\vec{x}_i$ and $\vec{x}_j$. According to Equation 5.1, the image values at large distances from the galactic centre have the largest impact on the

Table 5.1: Equations for deconvolving all moments up to order $n = 2$. The shown equations are specializations of Equation 5.7 and obey all conditions on the summation indices.

$$\{G\}_{0,0} = \{G^\star\}_{0,0}$$
$$\{G\}_{0,1} = \{G^\star\}_{0,1} - \{G\}_{0,0}\ \{P\}_{0,1}$$
$$\{G\}_{1,0} = \{G^\star\}_{1,0} - \{G\}_{0,0}\ \{P\}_{1,0}$$
$$\{G\}_{0,2} = \{G^\star\}_{0,2} - \{G\}_{0,0}\ \{P\}_{0,2} - 2\{G\}_{0,1}\ \{P\}_{0,1}$$
$$\{G\}_{1,1} = \{G^\star\}_{1,1} - \{G\}_{0,0}\ \{P\}_{1,1} - \{G\}_{0,1}\ \{P\}_{1,0} - \{G\}_{1,0}\ \{P\}_{0,1}$$
$$\{G\}_{2,0} = \{G^\star\}_{2,0} - \{G\}_{0,0}\ \{P\}_{2,0} - 2\{G\}_{1,0}\ \{P\}_{1,0}$$

$\langle I \rangle_n$ if $n > 0$. For finite and compact brightness distributions G, these values are dominated by the noise process instead of the galaxy, whose moments we seek to measure. Consequently, centered weight functions W of finite width are typically introduced to limit the integration range in Equation 5.1 to regions in which I is mostly determined by G,

$$I_w(\vec{x}) \equiv W(\vec{x})\, I(\vec{x}). \tag{5.9}$$

A typical choice for W is a circular Gaussian centered at the galactic centroid,

$$W(\vec{x}) \equiv \exp\Big(-\frac{\vec{x}^2}{2s^2}\Big). \tag{5.10}$$

Alternatively, one can choose to optimize the weight function to the shape of the source to be measured. Bernstein and Jarvis (2002, see their section 3.1.2) proposed the usage of a Gaussian, whose centroid $\vec{x}_c$, size s, and ellipticity ϵ are matched to the source, such that the argument of the exponential in Equation 5.10 is modified according to

$$\vec{x} \to \vec{x}' = \begin{pmatrix} 1-\epsilon_1 & -\epsilon_2 \\ -\epsilon_2 & 1+\epsilon_1 \end{pmatrix} (\vec{x} - \vec{x}_c). \tag{5.11}$$

As such a weight function represents a matched spatial filter, it optimizes the significance and accuracy of the measurement if its parameters are close to their true values. This can, however, not be guaranteed in presence of pixel noise, but we found the iterative algorithm proposed by Bernstein and Jarvis (2002) to converge well in practice and therefore employ it to set the weight function within the DEIMOS method.

Unfortunately, a product in real space like the one in Equation 5.9 translates into a convolution in Fourier-space. We therefore have to expect some amount of mixing of the moments of I_w. Even worse, an attempt to relate the moments of I_w to those of I leads to diverging integrals. Hence,

Table 5.2: Correction terms for deweighting moments of order $n = i + j$. The deweighted moments $\{I_{dw}\}_{i,j}$ are given by the sum of the correction terms up to the limiting order n_w.

n_w	correction terms
0	$\{I_w\}_{i,j}$
2	$\frac{1}{2s^2}\Big[c_1\{I_w\}_{i+2,j} - 4\,\epsilon_2\{I_w\}_{i+1,j+1} + c_2\{I_w\}_{i.j+2}\Big]$
4	$\frac{1}{8s^4}\Big[c_1^2\{I_w\}_{i+4,j} - 8\,c_1\epsilon_2\{I_w\}_{i+3,j+1} + \big[2\,c_1c_2 + 16\,\epsilon_2^2\big], \{I_w\}_{i+2,j+2} - 8\,c_2\epsilon_2\{I_w\}_{i+1,j+3} + c_2^2\{I_w\}_{i,j+4}\Big]$
6	$\frac{1}{48s^6}\Big[c_1^3\{I_w\}_{i+6,j} - 12\,c_1^2\epsilon_2\{I_w\}_{i+5,j+1} + \big[3\,c_1^2c_2 + 48\,c_1\epsilon_2^2\big]\,\{I_w\}_{i+4,j+2} - \big[24\,c_1c_2\epsilon_2 + 64\,\epsilon_2^3\big]\,\{I_w\}_{i+3,j+3} + \big[3\,c_1c_2^2 + 48\,c_2\epsilon_2^2\big]\,\{I_w\}_{i+2,j+4} - 12\,c_2^2\epsilon_2\{I_w\}_{i+1,j+5} + c_2^3\{I_w\}_{i,j+6}\Big]$

there is no exact way of incorporating spatial weighting to the moment approach outlined above. On the other hand, we can invert Equation 5.9 for $I = I_w/W$ and expand $1/W$ in a Taylor series around the centre at $\vec{x} = \mathbf{0}$,

$$\begin{aligned} W^{-1}(\vec{x}) \;\approx\; & W^{-1}(\mathbf{0}) - W'(\mathbf{0})\Big[\sum_{k=1}^{2} c_k x_k^2 \;+ 4\epsilon_2 x_1 x_2\Big] + \\ & \frac{1}{2}W''(\mathbf{0})\Big[\sum_{k,l=1}^{2} c_k c_l x_k^2 x_l^2 - 8\epsilon_2 \sum_{k=1} c_k x_k^2 x_1 x_2 + (4\epsilon_2 x_1 x_2)^2\Big], \end{aligned} \tag{5.12}$$

where we employed $W'(\vec{x}) \equiv \frac{dW(\vec{x})}{d\vec{x}^2}$ and $c_{1,2} \equiv (1 \mp \epsilon_1)^2 + \epsilon_2^2$. We introduce the parameter n_w as the maximum order of the Tailor expansion, here $n_w = 4$. Inserting this expansion in Equation 5.1, we are able to approximate the moments of I by their *deweighted* counterparts $\{I_{dw}\}$. For convenience we give the correction terms for orders $n_w \leq 6$ in Table 5.2. This linear expansion allows us to correct for the weighting-induced change in the moments of a certain order n by considering the impact of the weight function on weighted moments up to order $n + n_w$.

5.3.1 Deweighting bias

The truncation of the Taylor expansion constitutes the first and only source of bias in the DEIMOS method. The direction of the bias is evident: As the weight function suppresses contributions to the moments from pixel far away from the centroid, its employment reduces the power in any moment by an amount, which depends on the shape – particularly on the radial

profile – of the source and the width s. Additionally, if the ellipticity ϵ was misestimated during the matching of W, the measured ellipticity of the source χ before and after deweighting will be biased towards ϵ. Luckily, the error of ϵ stems from pixel noise and has therefore a vanishing mean, such that the χ remains free of ϵ-bias.

We investigate now the systematic impact of a finite n_w on the recovery of the deweighted moments. For the experiments in this section we simulated simple galaxy models following the Sérsic profile, as defined in equation 3.38, while the PSFs are modeled from the Moffat profile (equation 4.53). Both model types acquire their ellipticity according to Equation 5.11

In the top panel of Figure 5.1 we show the error after deweighting a convolved galaxy image from a matched elliptical weight function as a function of its size s. As noted above, the bias is always negative and is clearly more prominent for the larger disk-type galaxy (circle markers). As the Taylor expansion becomes more accurate for $n_w \to \infty$ or $s \to \infty$, the bias of any moment decreases accordingly.

An important consequence of the employment of a weight function with matched ellipticity is that the bias after deweighting does only very weakly depend on the apparent ellipticity, i.e. all moments of the same order are biased by the same relative factor $\Delta(n, s)$. This means any ratio of such moments remains unbiased. This does not guarantee that the ellipticity is still unbiased after the moments have passed the deconvolution step, which is exact only for unweighted moments. On the other hand, the particular form of the equations in Table 5.1 becomes important here: If we assume well-centered images of the galaxy and the PSF and a negligible error of the source flux $\{G\}_{0,0}$, the deconvolution equations for the relevant second-order moments only mix second-order moments. If furthermore $\Delta_G(2, s) = \Delta_P(2, s)$, the ellipticity χ (cf. Equation 3.10) will remain unbiased after deconvolution even though the moments themselves were biased. The aforementioned condition holds if the radial profiles of PSF and galaxy are similar within the weight function, in other words: if the galaxy is small. This behavior can clearly be seen in the bottom panel of Figure 5.1, where the ellipticity estimate of the smaller elliptical galaxy (diamond markers) has sub-percent bias for $n_w \geq 2$ and $s \geq 3$. The estimates for the larger galaxy are slightly higher because $|\Delta_G(2, s)| > |\Delta_P(2, s)|$, i.e. the deconvolution procedure overcompensates the PSF-induced change of the moments. However, sub-percent bias is achieved for $n_w \geq 4$ and $s \geq 5$.

For large galaxies, it might be advantageous to adjust the sizes of galaxy and PSF independently as this would render $\Delta_G(2, s_G)$ more comparable to $\Delta_P(2, s_P)$. However, we found employing a common size s for

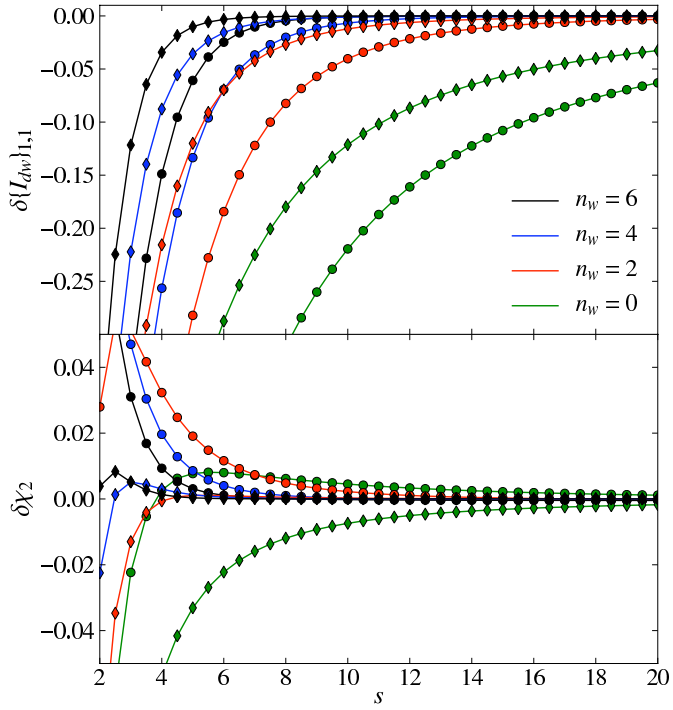

Figure 5.1: Weighting-induced bias. Relative error of the PSF-convolved and deweighted moment $\{I_{dw}\}_{1,1}$ (top) and of the estimated ellipticity after deconvolution (bottom) as a function of weight function size s. Colors indicate the correction order n_w, while markers denote the galaxy model (circles for model 1, diamonds for model 2). The galaxy models are simulated as Sérsic profiles with the following parameters: $\epsilon^s = (0.1, 0.4)$, $n_s = 1\,(4)$, $R_e = 3\,(1.5)$ for model 1 (2). The PSF was of Moffat-type with $\epsilon = (0.05, 0.05)$, $\beta = 3$, FWHM $= 3$. The weight functions of galaxy and PSF had the same size s, but individually matched ellipticities.

both objects to be more stable for the small and noisy galaxy images typically encountered in weak-lensing applications. We therefore adjust the size s such as to allow an optimal measurement of the deweighted PSF moments. Since the main purpose of the weighting is the reduction of noise in the measured moments, one could improve the presented scheme by increasing s for galaxies with larger surface brightness such as to reduce the bias when the data quality permits.

5.3.2 Deweighting variance

Being unbiased in a noise-free situation does not suffice for a practical weak-lensing application as the image quality is strongly degraded by pixel noise. We therefore investigate now the noise properties of the deweighted and deconvolved moments.

The variance of the weighted moments is given by

$$\sigma^2\left(\{I_w\}_{i,j}\right) = \sigma_n^2 \int \mathrm{d}\vec{x}\, W^2(\vec{x})\, x_i^2 x_j^2 \tag{5.13}$$

since the noise is uncorrelated and has a vanishing mean. It is evident from Table 5.2 that the variance of the deweighted moments increases with the number of contributing terms, i.e. with n_w. Less obvious is the response under changes of s. While each moment accumulates more noise with a wider weight function, the prefactors of the deweighting correction terms is proportional to s^{-n_w} such that their impact is reduced for larger s.

To quantitatively understand the impact of n_w and s in a fairly realistic scenario we simulated 10,000 images of the galaxy models 1 and 2 from the last section. We drew their intrinsic ellipticities from a Rayleigh distribution with $\sigma_{|\epsilon^s|} = 0.3$. Their flux was fixed at unity, and the images were degraded by Gaussian pixel noise with variance σ_n^2. We ran DEIMOS on each of these image sets with a fixed scale s. The results are presented in Figure 5.2, where we show the dispersion of the measured χ in units of the dispersion of χ^s. From the left panel it becomes evident that the attempt of measuring unbiased ellipticities (large n_w or s) comes at the price of increased noise in the estimates. Considering also Figure 5.1, we infer that in this bias-variance trade-off small values of s and large values of n_w should be favored since this provides estimates with high accuracy and a moderate amount of noise.

In the right panel of Figure 5.2 we show the estimator noise as function of the pixel noise. Equation 5.13 suggests that there should be a linear relation between these two quantities, which is roughly confirmed by the plot. Additional uncertainties in the moment measurement – caused by e.g. improper centroiding – and the non-linear combinations of second-

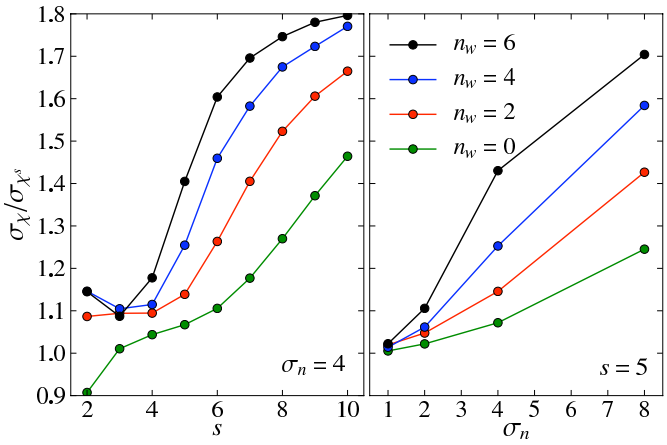

Figure 5.2: Noise of the deweighted and deconvolved ellipticity estimate as a function of the weight function size s (left) and of the standard deviation of the pixel noise σ_n (right). The color and marker code is explained in Figure 5.1. The pixel noise is given in units of 10^{-3} for flux-normalized sources. $\sigma_n = 8$ is close to the detection limit for this source model.

order moments to form χ lift the actual estimator uncertainty beyond the linear prediction.

Even though the true errors of χ may not exactly follow the linear theory, we will now exploit the fairly linear behavior to form error estimates. We can express the deweighting procedure as a matrix mapping, from which we can obtain the marginalized errors by

5.4 Shear accuracy tests

So far, we were concerned with the estimation of ellipticity. To test the ability of our new method to estimate the shear, we make use of the reference simulations with realistic noise levels from the GREAT08 challenge (Bridle et al., 2010). As the shear values in these simulations are fairly low, we employ the linearized version of 3.6, corrected by the shear responsivity of the source ensemble (equation 3.13), without any further weighting of individual galaxies, to translate DEIMOS ellipticity measures into shear estimates. The dispersion σ_χ^2 is measured from the lensed and noisy galaxy images and hence only coarsely describes the intrinsic shape dispersion (cf. Figure 5.2). We are aware of this limitation and verified with additional simulations that it introduces sub-percent biases for the range of shears and pixel noise levels we expect from the GREAT08 images.

We inferred the weight function size $s = 4$ and the correction order

$n_w = 4$ from the optimal outcome for a set with known shears. The actual GREAT08 challenge data comprises 9 different image sets, which differ in the shape of the PSF, the signal-to-noise ratio, the size, and the model-type of galaxies. For each of these branches, there are 300 images with different values of shear. We performed the DEIMOS analysis of all images keeping the weighting parameters fixed to the values inferred before. The results are shown in 5.3 in terms of:

- The GREAT08 quality metric Q:

$$Q = \frac{10^{-4}}{\langle(\langle g_{ij}^m - g_{ij}^t\rangle_{j\in k})^2\rangle_{ikl}} \tag{5.14}$$

  where g_{ij}^m is the ith component of the measured shear for simulation j, g_{ij}^t is the corresponding true shear component, the inner angle brackets denote an average over sets with similar shear value and observing conditions $j \in k$ and the outer angle brackets denote an average over simulations with different true shears k, observing conditions l and shear components i (Bridle et al., 2010). A Q value is defined also for each simulation branch:

$$Q = \frac{10^{-4}}{\langle(\langle g_{ij}^m - g_{ij}^t\rangle_{j\in k})^2\rangle_{ikl}} \tag{5.15}$$

  In this case, the average over different observing conditions l is omitted.

- The multiplicative shear accuracy parameters m_i obtained from a linear fit of the shear estimates $\tilde{g}_i$ to the true shear values g_i as defined in the STEP shear testing program (Heymans et al., 2006; Massey et al., 2007b),

$$\tilde{g}_i - g_i = m_i\, g_i + c_i. \tag{5.16}$$

From 5.3 we clearly see the highly competitive performance of DEIMOS with a typical $Q > 200$ in all but two branches. Single-component galaxy models yield a particularly large Q-value, probably because the bulge-only models are the most compact ones and thus favor the setting of a constant s for PSF and galaxies. In terms of Q, there is no change between the centered and the off-centered double-component galaxy models, but both m_i drop for the off-centered ones. As such galaxy shapes have variable ellipticity with radius and DEIMOS measures them with a fixed weight function size, we interpret this as a small but noticeable ellipticity-gradient bias (Bernstein, 2010).

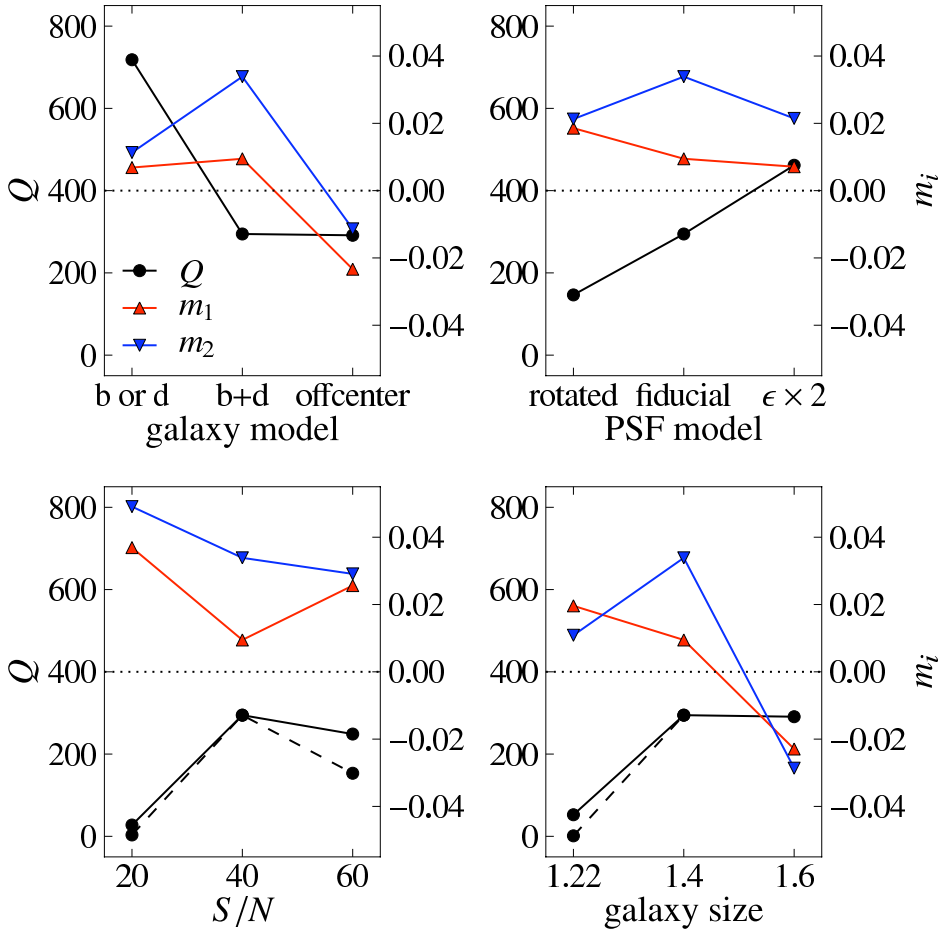

Figure 5.3: GREAT08 Q metric and multiplicative shear accuracy m_i for the nine different branches of the GREAT08 challenge data with realistic noise levels. In each panel, the scale on the left describes the values of Q and the scale on the right the values of m_i. The dotted line denotes $m_i = 0$. The dashed lines show the Q-value before we adjusted the weight-function matching and deweighting parameters to the source characteristics of the branch.

The response to changes in the PSF shape is a bit more worrisome and requires explanation. The fiducial PSF had $\epsilon_1 > \epsilon_2$, and the opposite is true for the rotated one. From all panels of 5.3 we can see that typically $|m_1| < |m_2|$. Such a behavior has already been noted by Massey et al. (2007b): Because a square pixel appears larger in diagonal direction than along the pixel edges, the moment $\{I\}_{11}$ and hence ϵ_2 suffer more strongly from the finite size of pixels. From the discussion in 5.3.1, we expect a certain amount of PSF-overcompensation for small weighting function sizes. As the PSF shape is most strongly affected by pixelation, the overcompensation boosts preferentially those galaxy moments, which align with the semi-minor axis of the PSF. In general, a larger PSF – or a larger PSF ellipticity – improves the shear estimates. It is important to note, that, as in all other panels, the residual additive term c_i was negligible for all PSF models.

The response to changes in S/N or galaxy size is more dramatic: Particularly the branches 7 (low S/N) and 9 (small galaxies) suffer from a considerable shear underestimation. This is not surprising as also most methods from Bridle et al. (2010) showed their poorest performance in these two sets. Since the Q metric strongly penalizes poor performance in single GREAT08 branches, the overall $Q = 7.7$ for this initial analysis.

As this is the first application of DEIMOS to a weak-lensing test case, we allowed ourselves to continue in a non-blind fashion in order to work out how the DEIMOS estimates could be improved. Apparently, problems arise when the galaxies are small or faint. The obvious solution is to shrink the weight function size. As discussed in section 5.3.2, improper centroiding plays an increasing role in deteriorating shear estimates for fainter galaxies. We therefore split the weight-function matching into two parts: centroid determinations with a small weight function of size s_c, and ellipticity determination with $s > s_c$. By choosing $s_c = 1.5$ and $s = 2.5$, we could strongly improve the performance for branches 7 and 9. Given the high S/N of branch 6, we decided to rerun these images with $n_w = 6$, which yielded another considerable improvement. With these modifications to the weight-function matching and the deweighting parameters, DEIMOS estimates achieve $Q = 112$, similarly to LENSFIT with $Q = 119$, at a fraction of the runtime (0.015 seconds per GREAT08 galaxy). We emphasize that this is a somewhat skewed comparison as we had full knowledge of the simulation characteristics. However, the changes to the initial analysis are modest and straightforward. In particular, they depend on galactic size and magnitude only, and not on the true shears.

Given the bias-variance trade-off from the deweighting procedure, the outcome of this section also clearly indicates that a simple *one size fits all*

approach is not sufficient to obtain highly accurate shear estimates from DEIMOS. For a practical application, a scheme to decide on n_w, s_c, and s for each galaxy needs to be incorporated. Such a scheme can easily be learned from a small set of dedicated simulations, foremost because the DEIMOS results depend only weakly on PSF and intrinsic galaxy shape.

5.5 Comparison to other methods

Because of the measurement of image moments subject to a weighting function, DEIMOS shares basic ideas and the computational performance with the traditional KSB-approach. In contrast to it, DEIMOS does not attempt to estimate the shear based on the ellipticity of single galaxies[2], nor does it need to assume that the PSF can be decomposed into an isotropic and an anisotropic part, which introduces residual systematics into the shear estimation if the anisotropic part is not small (Kuijken, 1999a). DEIMOS rather offers a mathematically exact way of deconvolving the galaxy moments from any PSF, thereby circumventing the problems known to affect KSB (see previous chapter). Its only source of bias stems from the inevitably approximate treatment of the weight function, which requires the measurement of higher-order image moments. Since DEIMOS measures all moments with the same weight function (instead of with increasingly narrower higher derivatives of the weight function), these higher-order correction terms suffer less from pixelation than those applied in KSB. However, as we could see in 5.4, pixelation affects the DEIMOS measurements, and an analytic treatment of it is not obvious.

The treatment of the convolution with the PSF on the basis of moments is very close to the one known from shapelets (Refregier and Bacon, 2003; Melchior et al., 2009). However, DEIMOS does not require the time-consuming modeling process of galaxy and PSF, and hence is not subject to problems related with insufficient modeling of sources, whose apparent shape is not well matched by a shapelet model of finite complexity (Melchior et al., 2010a).

In the RRG method (Rhodes et al., 2000), the effect of the PSF convolution is also treated in moment space. Furthermore, an approximate relation between weighted and unweighted moments is employed, which renders this approach very similar to the one of DEIMOS. The former differs in the employment of the KSB-like anisotropy decomposition of the PSF shape.

As mentioned in 5.3, DEIMOS makes use of the same iterative algo-

[2]This demands setting $\chi^s = 0$ in the non-linear Equation 3.6, which is only true on average but not individually.

rithm as ELLIPTO (Bernstein and Jarvis, 2002) to define the centroid and ellipticity of the weight function. The latter additionally removes any PSF anisotropy by applying another convolution to render the stellar shapes circular, which is not necessary for DEIMOS.

The recently proposed FDNT method (Bernstein, 2010) deconvolves the galaxy shape from the PSF in the Fourier domain, and then adjusts centroid and ellipticity of the coordinate frame such that the first-order moments and the components of the ellipticity – formed from second-order moments – vanish in the new frame. FDNT restricts the frequencies considered during the moment measurement to the regime, which is not suppressed by PSF convolution. Because of the shearing of the coordinate frame, additional frequencies need to be excluded, whereby the allowed frequency regime further shrinks. This leads to reduced significance of the shear estimates for galaxies with larger ellipticities. Furthermore, FDNT requires complete knowledge of the PSF shape. In contrast, DEIMOS does not need to filter the data, it extracts the lensing-relevant information from the low-order moments of the galaxy and PSF instead. These differing aspects indicate that DEIMOS should be more robust against pixel noise. It should also be possible to incorporate the correction for ellipticity-gradient bias suggested by Bernstein (2010) in the DEIMOS method.

5.6 Conclusions

For the presented work, we considered the most natural way of describing the effects of gravitational lensing to be given by the change of the multipole moments of background galaxies. We directly estimate the lensed moments from the measured moments, which are affected by PSF convolution and the application of a weighting function. For the PSF convolution we derive an analytic relation between the convolved and the unconvolved moments, which allows an exact deconvolution and requires only the knowledge of PSF moments of the same order as the galaxy moments to be corrected. The weighting-induced changes of moments cannot be described analytically, but for smooth weight functions a Taylor expansion yields approximate correction terms involving higher-order moments.

We showed that the residual bias of the deweighted moments stemming from an incomplete weighting correction is modest. Moreover, choosing a weight function with matched ellipticities but same size for measuring stellar and galactic moments yields ellipticity estimates with very small bias even for rather small weighting function sizes, which are required to reduce the impact of pixel noise to a tolerable level. In this bias-variance trade-off, DEIMOS normally performs best with high correction orders n_w

at small sizes s, but data with high significance may need a different setup. The choice of these two parameters is the trickiest task for a DEIMOS application, but can be easily addressed with a dedicated simulation, which should resemble the size and brightness distribution of sources to be expected in the actual data. Other properties of the sources, like their ellipticity distribution or, more generally, their intrinsic morphology, do not need to be considered as the measurement of moments does neither imply nor require the knowledge of the true source model.

There are certain restrictions of the method to bear in mind:

1. Setting s to be the same for galaxies and the PSF works best for small galaxies, whose shape is dominated by the PSF shape.

2. Changes of the shape at large radii would fall outside of the weight function and hence be ignored. When present in the PSF shape, this could lead to a residual PSF contamination, but can be cured by increasing the scale of the weight function at the expense of larger noise in the galaxy moments. When present in galactic shapes, the results become susceptible to ellipticity-gradient bias.

3. Direct measurement of the moments from the pixel values is inevitably affected by pixelation. For small, potentially undersampled shapes this leads to biased moment and ellipticity measures and acts more strongly in diagonal direction, i.e. on ϵ_2.

4. The noise on the ellipticity estimates based on image moments is not Gaussian, nor does it propagate easily into the shear estimate. When dominant, it can create substantial biases of its own.

Only the first of these restrictions exclusively applies to DEIMOS, the others are present in all non-parametric methods, which work directly on the pixelated image. Model-based approaches could replace the coarsely sampled moment measurements by ones obtained from the smooth models.

5.7 Outlook

We showed in this chapter how DEIMOS can be used to measure ellipticities of galaxies. It is clear, looking at equation 5.9, that the method can be easily extended for flexion measurements. Measuring flexion requires measuring third and fourth moments of the light distribution (see equation 3.23 and 3.24) for which deconvolving equations (as the ones presented in Table 5.1) can be easily derived. Moreover, in order to optimise the weighting function to the shape of the object, which we expect

to show additional deformations induced by flexion, one have to modify the exponential of the gaussian allowing for spin-1 and spin-3 distortion, as was done in equation 5.13 for the spin-2 distortion. Extensive tests are planned to investigate the noise properties of the 3rd and 4th moments and the noise in $\mathcal{F}$ and $\mathcal{G}$ flexion measurements against the size of the weighting function and against the standard deviation of pixel noise. We are convinced, based on the results achieved so far, that DEIMOS is a very promising method also for flexion estimation, specially if compared with the extension of KSB to the HOLICs, which relies, as shown in the previous chapter, on very strong assumption specially on the PSF shape.

Noi divenimmo intanto a piè del monte;
quivi trovammo la roccia sì erta,
che 'ndarno vi sarien le gambe pronte.[0]

Dante (1265-1321) Purgatorio III

6

Inner density profile of dark matter halos

In this last chapter we want to discuss a possible application of shear measurements for studying properties of galaxy clusters. Numerical simulations of non-linear structure formation reveal a typical shape for the density profile of dark matter halos. In section 1.5.1 we showed how the density profile is generally described by the so-called generalised NFW profile. Do real halos behave in the same way as theory predicts?

Gravitational lensing should in principle be able to give the cleanest answer to this question. Density profiles in galaxy-sized objects are expected to be modified on small scales by baryonic physics, where they are likely to approach the isothermal density slope $\propto r^{-2}$ instead of the generic dark matter behaviour. On the mass scale of galaxy groups or clusters, however, baryonic physics should be constrained to the innermost region, leaving the dark matter density profile almost intact. Galaxy-galaxy lensing seems to show tentative evidence for this expectation (Mandelbaum et al., 2006) : while the shear profile around low-mass halos is consistent with an isothermal density profile, it seems to flatten towards the theoretical expectation for dark matter halos around high-mass halos.

The question is important because it aims at a central prediction of non-linear cosmological structure formation. Answering it is complicated by the angular resolution limit of 20 arcsec of weak gravitational lensing, set by the number density of background galaxies, and by the high non-linearity of strong gravitational lensing. In fact, claims that strong gravitational lensing, when combined with stellar dynamics, requires flat halo cores have been made (Sand et al., 2004) and doubted. In particular (Meneghetti et al., 2007) showed how the measurement of the inner slope can be systematically underestimated if halo's substructure are not taken into account. A weak lensing analysis, even if observationally more

[0]By this time we had reached the mountain's base/discovering a wall of rock so sheer/that even agile legs are useless there.

challenging, has the advantage to be almost insensitive to cluster's substructures because of the intrinsic nature of the signal.

Previous studies based on weak lensing have followed an approach where a shear profile was first measured and then fit to the shear profile expected from certain three-dimensional density profiles, thus indirectly constraining the density-profile models. Given the sparseness of lensing information near the core of galaxy groups and clusters, we develop a different approach here. Instead of constraining the shear profile, we only wish to derive a single number from the shear data, namely the slope α of the density profile within the characteristic radius, assuming that the asymptotic outer slope is -3.

We pursue this approach with two linear filtering techniques. One of them is specifically constructed below to return α as its only result. It is thus made to combine all available information into its estimate and should thus optimise the significance of the measurement. The other varies the inner slope of the density profile until it finds the maximum signal-to-noise ratio in a given sample of halos.

6.1 Methods to characterize the shear profile

In this section we describe two methods, based on optimal linear filters (Sanz et al., 2001; Maturi et al., 2005), to estimate the inner slope of dark matter halos using weak-lensing observations. The advantage of linear filtering as opposed to standard profile fitting is that filters can be constructed such as to minimise noise caused by intervening structures along the line-of-sight.

6.1.1 Optimal linear filtering

For a generic optimal linear filter, the data $D(\vec{\theta})$ is modelled as the sum of the signal to be measured and the noise

$$D(\vec{\theta}) = S(\vec{\theta}) + N(\vec{\theta}), \tag{6.1}$$

where $S(\vec{\theta}) = A\tau(\vec{\theta})$, A is the signal amplitude and $\tau(\vec{\theta})$ is a model for its angular shape. In our application, the signal is the lensing shear of the intervening dark matter halo (modelled with a generalised NFW profile) and the noise is given by the intrinsic ellipticity of the background galaxies, their finite number and the contamination due to large-scale structures. The noise components are assumed to be Gaussian, random with zero mean and isotropic since their statistical properties are independent of the position in the sky (for further detail see (Maturi et al., 2005)). We

now define a linear filter $\Psi(\vec{\theta}, \alpha, \vec{w})$ which, when convolved with the data, yields an estimate for the amplitude of the signal at the position $\vec{\theta}$:

$$A_{\rm est}(\vec{\theta}) = \int D(\vec{\theta}')\Psi(\vec{\theta} - \vec{\theta}', \alpha, \vec{w})\mathrm{d}^2\theta', \tag{6.2}$$

which is unbiased

$$b = A\left[\int \Psi(\vec{\theta}, \alpha, \vec{w})\tau(\vec{\theta}, \alpha, \vec{w})\mathrm{d}^2\theta - 1\right] = 0 \tag{6.3}$$

and whose variance σ^2

$$\sigma^2 = b^2 + \frac{1}{2\pi}\left[\int |\Psi(\vec{k}, \alpha, \vec{w})|^2 P_N(k)\mathrm{d}^2k\right], \tag{6.4}$$

is minimal. The filter Ψ satisfying these two conditions minimises the Lagrangian $L = \sigma^2 + \lambda b$. It reads

$$\Psi(k) = \frac{1}{2\pi}\left[\int \frac{|\tau(\vec{k}, \alpha, \vec{w})|^2}{P_N(k)}\mathrm{d}^2k\right]^{-1} \frac{\tau(\vec{k}, \alpha, \vec{w})}{P_N(k)}. \tag{6.5}$$

where $\vec{w} = (c, M, z)$ and $\hat{\Psi}$ and $\hat{\tau}$ are the Fourier transforms of the filter and the signal shape, respectively. Note that we have assumed in the previous derivation that the mean values of the halo parameters ($\vec{w}$) are well known. This is an idealising assumption and we refer to Sect. 6.2.1 for a more detailed discussion. The filter depends only on the angular shape of the signal $\tau(\vec{k}, \alpha, \vec{w})$ and the noise power spectrum P_N. In particular it is most sensitive to those spatial frequencies for which the signal τ is large and the noise power spectrum is small. This filter is optimal in the sense that it maximises the signal-to-noise ratio for the a given assumed signal shape.

The left panel of figure 6.1 shows the filter's shape calculated using three different values of the inner slope, $\alpha = 0.7, 1.0, 1.3$.

Dealing with non-linear signals

The filter described in the previous section can be used to measure quantities which appear linearly in equation 6.1 (e.g. the amplitude of the shear signal). This is not the case for the inner slope α breaking the main assumption on which the linear filter is based on. However, if we expand the halo's shear profile around a fiducial value of the inner slope, α_0,

$$\gamma(x, \alpha, \vec{w}) = \gamma(x, \alpha_0, \vec{w}) + \left.\frac{\partial\gamma(x, \alpha, \vec{w})}{\partial\alpha}\right|_{\alpha_0} \Delta\alpha, \tag{6.6}$$

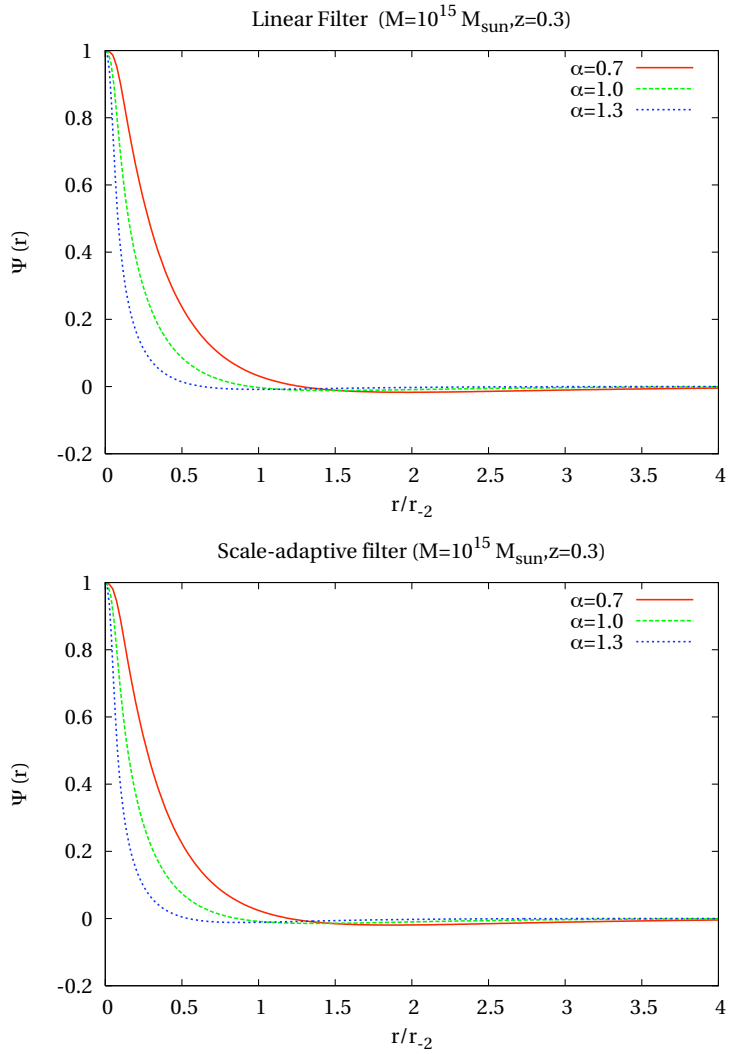

Figure 6.1: Optimal linear filter (*left panel*) and scale-adaptive filter (*right panels*) shapes calculated for three different values of α. All filters are normalised to unity.

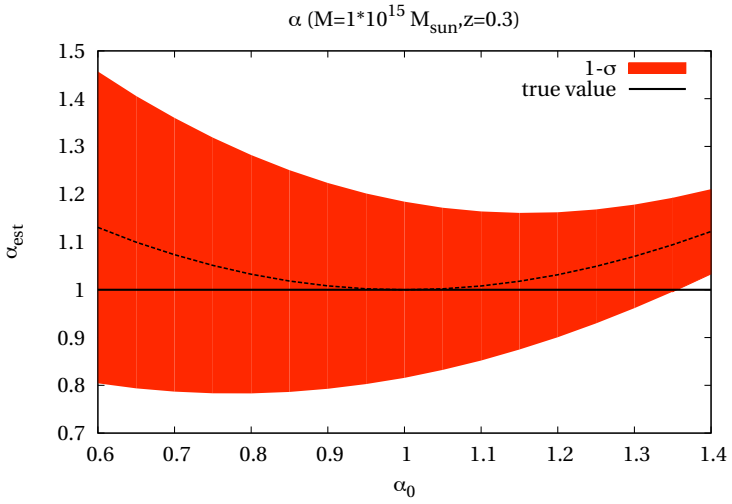

Figure 6.2: Estimated inner slope $\alpha_{\rm est}$ as a function of the fiducial inner slope α_0 used in the linear filter with the 1-σ error bars calculated via equation 6.4. The black line shows the real value of the halo's inner slope.

equation 6.1 reads

$$D(x) - \gamma(x, \alpha_0, \vec{w}) = \left.\frac{\partial \gamma(x, \alpha, \vec{w})}{\partial \alpha}\right|_{\alpha_0} \Delta\alpha + N(x), \tag{6.7}$$

such that $\Delta\alpha$ appears linearly and the linear filtering scheme can be applied. The shear derivative with respect to α plays the role of the signal shape, τ, and $\Delta\alpha$ that of the amplitude A to be measured. This allows the definition of the following estimator for the inner slope,

$$\alpha^{\rm est} = \int \Delta\gamma(\vec{x}, \alpha, \alpha_0, \vec{w}) \Psi(\vec{x}, (\alpha_0, \vec{w}) {\rm d}^2x + \alpha_0, \tag{6.8}$$

where

$$\Delta\gamma(\vec{x}, \alpha, \alpha_0, \vec{w})) = \gamma(\vec{x}, \alpha, \vec{w}) - \gamma(\vec{x}, \alpha_0, \vec{w}). \tag{6.9}$$

The approximation applied in equation 6.7 implies that $\alpha^{\rm est}$ is a good estimator of the inner slope only when α_0 is close to the real value of α. If this is not the case, the value of the inner slope tends to be overestimated as we show in figure 6.2. If a single halo is considered, the error bars associated to $\alpha_{\rm est}$ are so large that the overestimation can be neglected for a large range of α_0. However, if several halos are stacked, the error bars shrink and the overestimation becomes important. In order to avoid this problem, more measurements of the same halo have to be carried

out sequentially: the first measurement starting with an arbitrary value of α_0, and the second using the estimate $\alpha_{\rm est}$ found previously as a fiducial value. We tested that, for a reasonable guess of the first fiducial value, 2-3 measurements suffice to recover the correct slope.

6.1.2 Scale-adaptive filter

The linear expansion used in the previous section can be avoided by defining a scale-adaptive filter. Such a filter is defined similarly as the linear filter from Sect. 6.1.1 with an additional constraint on the amplitude of the signal $A_{\rm est}$ which must be maximised when the adopted inner slope fits the data best,

$$\xi = \left.\frac{\partial A_{\rm est}}{\partial \alpha}\right|_{\alpha_0} = 0. \tag{6.10}$$

The minimisation of $L = \sigma^2 + \lambda_1 b + \lambda_2 \xi$ leads to the filter

$$\Psi(k,\alpha) = \frac{1}{2\pi}\frac{\tau(k,\alpha)}{P_N(k)}\frac{1}{\Delta}\left[2b + c - (2a+b)\frac{{\rm d}\ln\tau(k,\alpha)}{{\rm d}\ln\alpha}\right] \tag{6.11}$$

with the constants

$$a = \frac{1}{2\pi}\int {\rm d}k k \frac{\tau(k,\alpha)}{P_N(k)} \tag{6.12}$$

$$b = \frac{1}{2\pi}\int {\rm d}k k \frac{k}{P_N(k)}\frac{{\rm d}\tau(k,\alpha)}{{\rm d}\ln\alpha} \tag{6.13}$$

$$c = \frac{1}{2\pi}\int {\rm d}k k \frac{1}{P_N(k)}\left(\frac{{\rm d}\tau(k,\alpha)}{{\rm d}\ln\alpha}\right)^2 \tag{6.14}$$

$$\Delta = ac - b^2\ . \tag{6.15}$$

Its defining property is thus to maximise the signal-to-noise ratio when the correct inner slope is adopted. This implies that the inner slope can only be determined indirectly from a sequence of measurements of the shear amplitude $A_{\rm est}$, searching for that value of α that maximises $A_{\rm est}$.

The filter shape is plotted in the right panel of figure 6.1.

6.1.3 Dealing with parameters degeneracy

The two methods presented in Sects. 6.1.1 and 6.1.2 assume a cluster model with known mass, redshift and concentration. In a realistic situation, we can assume to have sufficiently precise redshifts. Mass estimates would have to be obtained from optical richness, kinematics of the cluster galaxies or X-ray scaling relations. Then, estimates for the concentration could

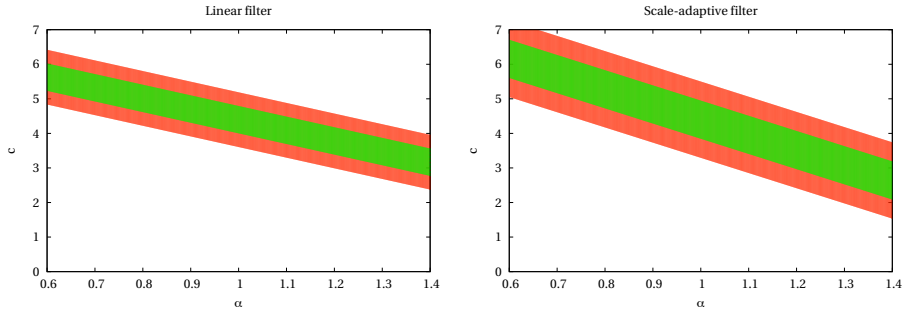

Figure 6.3: 1-σ and 2-σ likelihood regions in the plane (α, c) computed using the linear filter (*left panel*) and the scale-adaptive filter (*right panel*) for a halo of $M = 5 \times 10^{14} M_{\odot}$ at $z = 0.3$. The fiducial value is $(1.0, 4.4)$.

be derived from the mass-concentration relation found in numerical simulations, albeit with a considerable scatter. The concentration depends only very weakly on the mass, hence uncertainties in the mass estimate do not strongly affect the concentration estimate, and thus the mass does not need to be precisely known. However, numerical simulations suggest a log-normal distribution of the concentration around its mean with a standard deviation of ~ 0.2, which implies that concentration parameters of real clusters can only be very poorly guessed.

Moreover, the inner slope, as the parameter we are aiming to measure, is degenerate with the concentration. In fact, it is possible to describe a halo with high central density with a large value of α and a small value of c or vice versa, and so the problem is not well defined (Wyithe et al., 2001). Thus, any attempt at measuring the profile's inner slope depends critically on the assumed halo concentration, which is uncertain in reality.

To cope with this problem, it is convenient to re-parametrise the profile accounting for this model degeneracy, defining new parameters which can be more precisely measured. In short, the logic behind the procedure described below is as follows. In a realistic situation, we have no chance to break the degeneracy between c and α. Rather, we can rotate the parameter space such that one of its axes becomes parallel to the degeneracy direction and the other perpendicular to it. The latter will define a new parameter as a linear combination of c and α which observations can constrain best. Comparisons with theory should then be performed on the basis of this parameter rather than through c and α separately.

This is achieved by a Fisher-matrix analysis. The Fisher matrix is

$$F_{ij} = \left\langle \frac{-\partial^2 L}{\partial\theta_i \partial\theta_j} \right\rangle, \tag{6.16}$$

where L is the logarithm of the likelihood function and $\vec{\theta} = (\alpha, c)$ are the free model parameters. In case of a Gaussian probability distribution, the Fisher matrix can be written as

$$F_{ij} = \frac{1}{2} Tr[A_i A_j + C^{-1} M_{ij}] \tag{6.17}$$

where C is the covariance matrix, $A_i = C^{-1} C_{,i}$ and $M_{ij} = 2\frac{\partial\mu}{\partial\theta_i}\frac{\partial\mu}{\partial\theta_j}$ and μ is the assumed model. Since C does not depend on the inner slope and on the concentration, the first term in equation 6.17 vanishes. We evaluate the Fisher matrix at a fiducial point (α_0, c_0). In particular, we assume $\alpha_0 = 1$ and we calculate c_0 using the prescription by (Eke et al., 2001). We truncate the shear profile at an inner radius $R_{\rm min} = 1/\sqrt{n_{\rm gal}}$, which is the minimum achievable resolution for a given number density $n_{\rm gal}$ of background galaxies and at an outer radius $R_{\rm out} = R_{\rm vir}$. Once $R_{\rm out} > R_{\rm s}$ the Fisher matrix depends negligibly on $R_{\rm out}$ since the derivative of the shear profile with respect to alpha is zero and the derivative with respect to the concentration is very small.

The eigenvectors (v_1, v_2) and (v_3, v_4), of the Fisher matrix, determining the directions of largest and smallest degeneracy between the parameters α and c, define a rotation of the parameter space and thus two new parameters

$$P_1 = v_1\alpha + v_2 c \tag{6.18}$$

$$P_2 = v_3\alpha + v_4 c \tag{6.19}$$

which are linear combinations of α and c. The two new parameters are those which can be constrained best and worst, respectively, given the model adopted in the Fisher-matrix estimate.

If the linear filter is used to measure the inner slope, the model μ is

$$\mu = \alpha_{est}(\alpha, c) = \int [\gamma(\alpha, c) - \gamma(\alpha_0, c_0)]\Psi(\alpha_0, c_0)\mathrm{d}^2 x \tag{6.20}$$

and thus

$$\frac{\partial\mu}{\partial\theta_i} = \int \frac{\partial\gamma(\vec{x}, \vec{\theta})}{\partial\theta_i}\Psi(\vec{x}, \vec{\theta}_0)\mathrm{d}^2 x. \tag{6.21}$$

The covariance matrix reduces in this case to the variance of the measurement obtained from equation 6.4.

Note that the Fisher matrix defined above is singular, i.e. its determinant vanishes. The errors on the new parameters are given by $1/\sqrt{\lambda_i}$, where λ_i are the eigenvalues of the Fisher matrix. Since one of them is vanishing the error on one parameter (taken to be P_2) is infinite. This means that the likelihood region in the plane (α, c) is an ellipse infinitely elongated in the degeneracy direction. This is because there is more than one way of fitting a single data set ($\Delta\alpha$) by varying the two parameters. In the right panel of figure 6.3 we show the result for a halo of $M = 5 \times 10^{14} M_\odot/h$ at redshift $z = 0.3$ with concentration $c = 4.4$. The corresponding eigenvector components are $v_1 = v_4 = 0.95$ and $v_2 = -v_3 = 0.30$.

When the scale-adaptive filter is used, the measurable quantity is the shear amplitude

$$A(\alpha, c) = \int D(\alpha_{\rm H}, c_{\rm H}; \vec{x}) \Psi(\alpha, c_0; \vec{x}) {\rm d}^2 x, \tag{6.22}$$

and the value of the inner slope ($\alpha_{\rm est}$) is then estimated looking for the value of α maximising the amplitude. It is clear that it depends only on the halo's concentration c_0 assumed in the filter. To find the degeneracy direction between the inner slope and the concentration in this case, we analyse the relation between $\alpha_{\rm est}$ and c around a fiducial point in the (α, c) plane. The result is shown in the left panel of figure 6.3 for the same halo as considered before. Here, too, we define two new parameters $P_1 = 0.97\alpha + 0.22c$ and $P_2 = -0.22\alpha + 0.97c$. In this case, the error cannot be calculated analytically since the measurement is indirect. Instead, we have performed a Monte-Carlo simulation (see Sect. 6.2).

Since the shapes of the filters are different, so are the degeneracy directions we find.

The probability distributions of P_1 and P_2 can be found convolving the probability distributions of the concentration and the inner slope. Using the degeneracy direction found for the linear filter and assuming a log-normal distribution for the concentration with $\sigma_c = 0.2$ (Bullock et al., 2001b) and a Gaussian distribution for the inner slope with $\sigma_\alpha = 0.15$ (Diemand et al., 2004), we find that both probability distributions of P_1 and P_2 can be approximated as log-normal distributions with standard deviations $\sigma_{\rm P_1} = 0.29$ and $\sigma_{\rm P_2} = 0.33$ respectively, as shown in figure 6.4.

6.2 Method uncertainties

Here, we discuss in detail possible error sources affecting the measurement of the inner slope using the methods described in Sects. 6.1.1 and 6.1.2. We

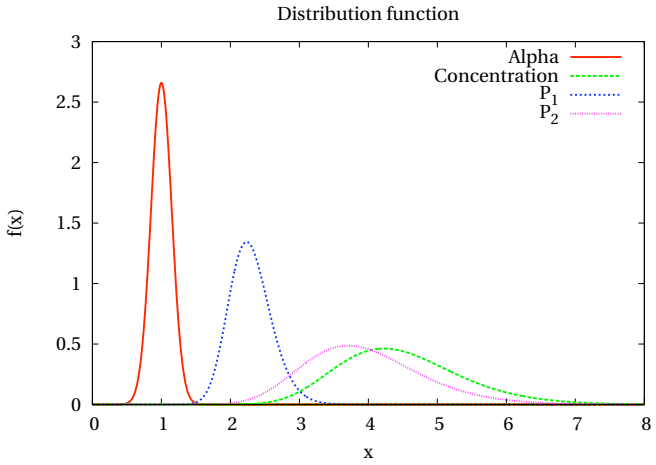

Figure 6.4: Probability distributions for α, c, P_1 and P_2. A normal distribution with $\sigma_\alpha = 0.15$ for the inner slope (Diemand et al., 2004) and a log-normal distribution with $\sigma_c = 0.2$ for the concentration (Bullock et al., 2001b) are assumed. The probability distribution for P_1 is given by the convolution of the probability distribution of α and c, while the probability distribution for P_2 is given by their cross correlation.

will show the error calculation for a halo of $M = 5 \times 10^{14} M_\odot/h$, $z = 0.3$, $c = 4.4$.

The statistical uncertainties arising from the data noise component N are given by the intrinsic ellipticity of the background galaxies, their finite number and from the contamination due to the intervening large-scale structures. The filters we have defined minimise these uncertainties. They are quantified by equation 6.4 for the linear filter and by a Monte-Carlo analysis for the scale-adaptive filter since in this case α is measured indirectly by estimating the location of the maximum in the estimated signal, and an analytical computation of its variance is impossible.

The Monte-Carlo analysis has been performed generating 1000 realisations of a shear catalogue using randomly distributed background galaxies with a density $n_{\rm gal} = 30/\mathrm{arcmin}^2$, placed at redshift $z_s = 1.0$, on a 0.01 degree field. The halo has been placed in the field centre. The noise due to the intrinsic galaxy ellipticities ($\sigma_\epsilon = 0.3$) and the lensing effect due to the intervening large-scale structure have been added. The latter noise is calculated assuming that the large-scale structure can be described by a Gaussian random field with a power spectrum determined by the linear theory of structure growth.

We assume in our analysis that the magnification bias can be neglected, allowing us to leave the effective number $n_{\rm gal}$ of available galaxies un-

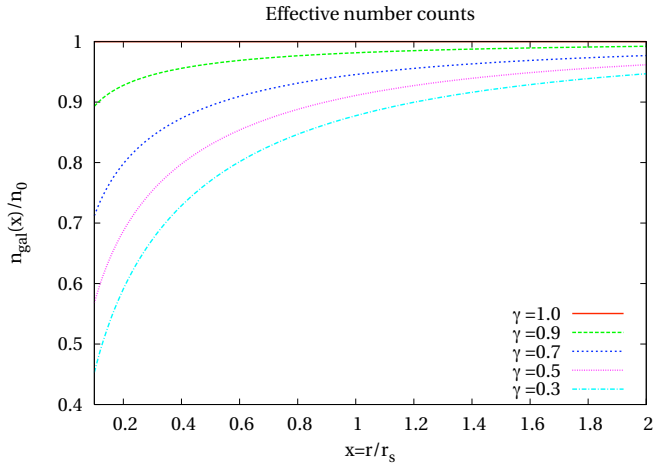

Figure 6.5: Magnification bias expected for an halo of $5 \times 10^{14} M_{\odot}/h$ at redshfit $z = 0.3$ lensing galaxies at $z = 1.0$. γ is the exponent of the power low in equation 6.23.

changed. This is justified only if the slope γ of the flux distribution of faint galaxies

$$n_0(> S) = aS^{-\gamma} \tag{6.23}$$

is unity as discussed by Bartelmann and Schneider (2001). The effective number of galaxies $n_{\rm eff}$ scales with γ as

$$\frac{n_{\rm eff}(> S)}{n_{\rm gal}(> S)} = \mu^{\gamma - 1} \tag{6.24}$$

where μ is the magnification. Specifically, $n_{\rm eff}$ is lowered by at most 40% compared to $n_{\rm gal}$ near $r = 0.2 r_{\rm s}$ if γ is 0.5, as shown in figure 6.5. For galaxies in the Hubble Ultra Deep Field (Beckwith et al., 2006) we estimate $\gamma \simeq 0.8$ causing a magnfication bias of around 10%.

For each realisation we use equation 6.2 to estimate the shear amplitude in the position corresponding to the halo's centre using filters initialised with an inner slope in the range $[0.6 - 1.4]$. The estimated inner slope value is then defined as the value of α giving the maximum value of the shear amplitude. We finally calculate their distribution and the dispersion around the mean value (the results are summarised in the fourth column of Table 1).

We find that the standard deviation associated with the inner slope, measured by the scale-adaptive filter, is 0.19. The analytical calculation done for the linear filter gives a value of 0.14.

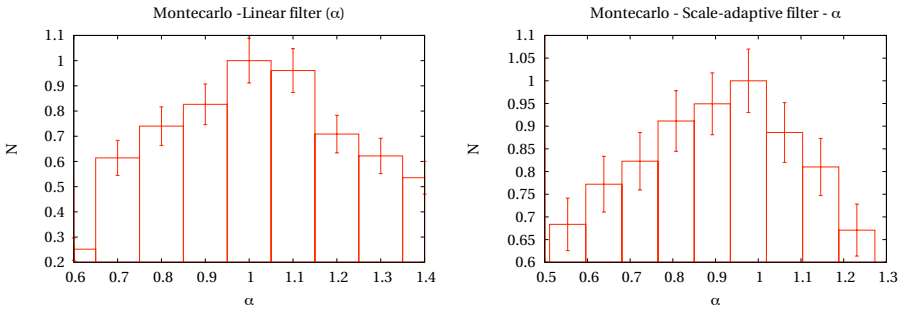

Figure 6.6: Normalised distributions of the value of the inner slope computed using the linear filter (*left panel*) and scale-adaptive filter (*right panel*). A Gaussian distribution has been assumed for the mass and the redshift, while a log-normal distribution has been adopted for the concentration.

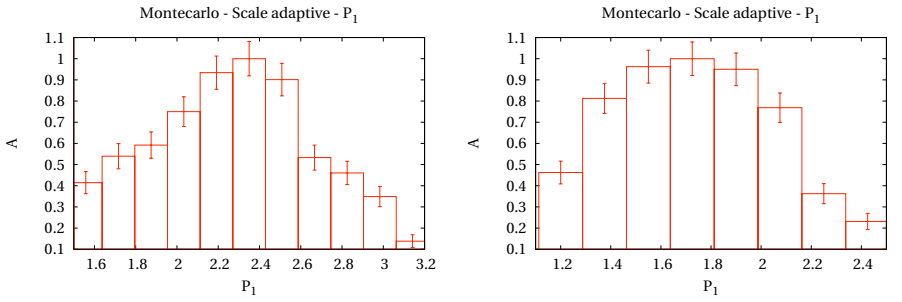

Figure 6.7: As figure 6.6, but using the new parameters P_1 and P_2 instead of α and c.

Filter	Parameter	Fiducial value	σ (stat.)	σ (stat.+model)	Percentage error
SAF	α	1.00	0.19	0.26	0.26
SAF	$P1$	1.95	0.21	0.29	0.15
LF	α	1.00	0.14	0.28	0.28
LF	P_1	2.31	0.15	0.30	0.13

Table 6.1: Statistical errors in the parameters measurement for a halo of $5 \times 10^{14} M_{\odot}$ at redshift $z = 0.3$. In the *first column* we indicate the used filter, in the *second column* the parameter we constrain and in the *third column* its fiducial value. In the *fourth column* are shown the expected errors assuming randomly distributed background galaxies with intrinsic ellipticity $\sigma_\epsilon = 0.3$ and random noise due to the large-scale structures. The errors presented in the *fifth column* take also into account Gaussian errors in the halo mass and redshift with standard deviations $\sigma_{\rm M} = 1.5 \times 10^{14}$ and $\sigma_{\rm z} = 0.03$, respectively, and a log-normal distribution for the concentration with standard deviation $\sigma_{\rm c} = 0.2$. When P_1 is estimated the probability distribution of P_2 is calculated from the probability distribution of the concentration assuming a Gaussian probability distribution for the inner slope with $\sigma_\alpha = 0.15$. In the *sixth column* we show the percentage error on the parameter estimation.

The same calculation has been done considering halos of different masses and at different redshifts. As shown in figure 6.8, the standard deviation increases with respect to the redshift and decreases when the mass is increasing. In particular for a halo placed at intermediate redshift between the background sources and the observer, the standard deviation varies in the range $[0.2 - 1.0]$ for a mass range $[10^{15} - 5 \times 10^{13}]$.

The preceding calculations show that errors on the inner slope due to intrinsic ellipticities of background galaxies and due to contamination by large-scale structures are large when computed for a single halo. However stacking a large number of halos (10-100), it is possible to measure an average value of α with a few percent accuracy.

A more accurate error evaluation has to consider also the scatter around the fiducial value of the halo's mass, redshift and concentration used in the filter definition. For both methods, we perform a Monte-Carlo simulation, following the procedure described above, assuming a Gaussian distribution for the halo mass ($\sigma_{\rm M} = 1.5 \times 10^{14}$) and redshift ($\sigma_{\rm z} = 0.03$) and a log-normal distribution for the concentration ($\sigma_{\rm c} = 0.2$) following numerical simulations. The result is shown in figure 6.6.

One critical point that we have avoided so far concerns the choice of the fiducial values for the halos parameter. We discuss this point in the following section.

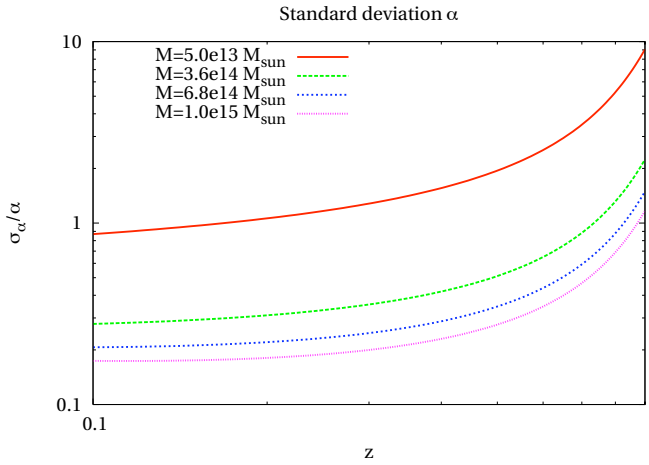

Figure 6.8: Standard deviation for α as a function of the halo's redshift and mass.

6.2.1 Model sensitivity

Defining the filter requires the specification of a model. The estimator (equation 6.2) we defined for the inner slope is unbiased only if the model is correct. We investigate here what happens if the filter is defined using a generalised NFW profile with wrong fiducial values of mass, redshift and concentration. We study in particular the case in which the fiducial redshift used in the filter differs from the real redshift by about 10 %, the mass by about 30 %, and the concentration by about 20 %. We show the results in the first three panels of figures 6.11 and 6.12 (blue lines) for the linear and the scale-adaptive filter, respectively.

As expected, the inner-slope estimate is biased. This reflects the degeneracy between the parameters, in particular between the scale radius $r_{-2} = r_{200}(M,z)/c_{-2}$ and the inner slope. The scale radius depends only slightly on the halo mass and redshift, while it is strongly affected by a variation in the concentration.

This bias has to be compared with the statistical errors associated with the measurement in order to assess whether uncertainties in the fiducial halo parameters are important or not. If a single halo is considered, a wrong assumption on the concentration (the most critical parameter) introduces a bias that is on the same order as the statistical error. However, if several halos are stacked (we show in figure 6.11 results after stacking 10 and 100 halos), the bias is a factor of 10 larger than the statistical uncer-

tainty.

In Sect. 6.1.3, we discussed how it is possible to deal with degeneracies between inner slope and concentration, defining two new parameters (P_1, P_2), linear combinations of c and α, which are respectively the best and the worst constrained parameters given our model. The measurement of the new parameter P_1 is almost unaffected by the choice of the other parameter P_2 as we show in the right panel of figure 6.11 and 6.12, while the effect of a wrong assumption of halo mass and redshift produces a similar bias. We recall that these latter quantities can be measured by means of other observables, as discussed before.

Once the model had been re-parametrised in term of P_1 and P_2, we estimated the error on P_1 using a Monte-Carlo simulation in the same way we have done before for α. The result is shown in figure 6.7.

6.3 Potential problems

We now want to point out the conditions under which the two methods described can be successfully applied.

First of all, the reduced shear must be measurable at relatively small angular scales (smaller than the scale radius of the halo) where the density profile is sensitive to a change of the inner slope.

Towards the halo's centre, the image distortion becomes non-linear such that the galaxy ellipticities are no longer an unbiased estimator of the shear. We quantify the expected deviation by a simple test: We use the deflection-angle map of an NFW halo to lens a circular source (for which we assumed a Sersic profile with $n = 1.5$ and $r = 0.35$arcsec) moving radially towards the halo centre. We measure the ellipticity of its image (using quadrupole moments) as a function of cluster-centric distance and compare it to the true reduced shear. Figure 6.9 shows the result for three different haloes ($M = 10^{14}, 5 \times 10^{14}, 10^{15} M_{\odot}/h$). The conclusion is that up to $r = 0.2 r_{\rm s}$ the measured ellipticity of galaxies is still an unbiased estimator of the (reduced) shear while at smaller scales the contribution from higher order terms start to be dominant. Therefore, $r \approx 0.2 r_{\rm s}$ should be taken as the minimum radius where the measured ellipticity can still be considered to faithfully represent the reduced shear.

However measuring shear at these scales can be tricky even with a high background galaxies density due to the possible dilution of the shear signal caused by cluster galaxies. In order to avoid this problem, accurate colour-magnitude information should be available so that it is possible to well separate cluster members from non-members (Broadhurst et al., 2005).

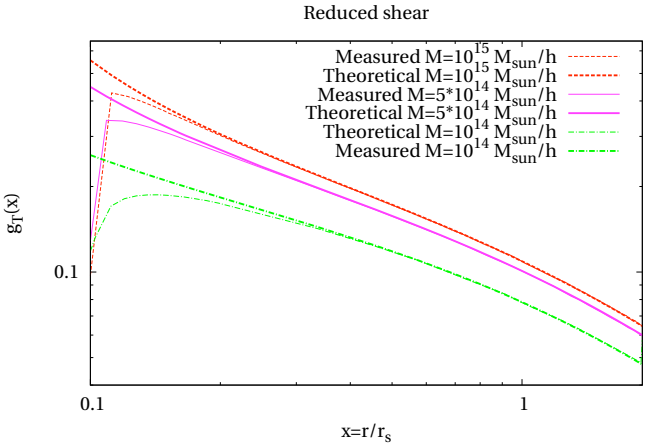

Figure 6.9: Comparison between the theoretical reduced tangential shear (*thick lines*) and the shear estimated from galaxy ellipticities (*thin lines*) for three different masses.

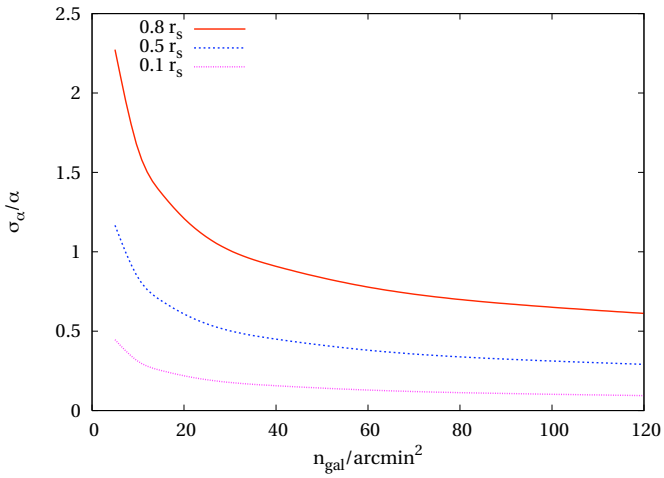

Figure 6.10: Standard deviation of the inner slope as a function of the background-galaxy number density and of the minimal radius where the shear can be detected. The calculation has been done for a halo of $M = 5 \times 10^{14} M_{\odot}/h$ at redshift $z = 0.3$ with $\alpha = 1.0$ using the linear filter.

We showed in the previous section that the error associated to the measurement of the inner slope is high when computed for a single halo. Thus several haloes need to be stacked together. The number of haloes to be stacked depends strongly on the minimal radius where the shear can be detected, and on the number of background galaxies. In Fig. 6.10, we plot the relative error on the measurement of α as a function of these two parameters for a halo of $M = 5 \times 10^{14} M_\odot/h$ at redshift $z = 0.3$. Assuming 30 galaxies per square arc minute, the number of haloes to be stacked to reach an accuracy of a few percent on the inner slope is between 10 and 100 going from $r_{\rm min} = 0.2 r_{\rm s}$ to $r_{\rm min} = 0.8 r_{\rm s}$. We emphasise that the stacking procedure can be affected by a wrong determination of the cluster centre that causes a circularisation of the average cluster profile in its central part (Kathinka Dalland Evans and Bridle, 2008).

Meneghetti et al. (2007) showed how the determination of the inner slope can be biased if the triaxiality structure of the haloes are not taken properly into account. However if many haloes are stacked together a direct comparison with the projected DM average profile found using stacked simulated clusters can be consistently done.

Moreover the effect of the baryons in shaping the density profile at this scale is not negligible. We plan to attack this problem using numerical simulation in order to study the effect of stacking and the presence of the baryons on our results.

6.4 Conclusion

Starting from the question how the central density profiles of group or cluster-sized, dark matter halos can best be constrained and compared to observations, we have developed two methods based on linear filtering of gravitational-shear data that aim at returning a single number, i.e. an estimate of the inner slope α of density profile. One filter is constructed to directly return this number, the other searches for the maximum of the signal-to-noise ratio as a function of α. Our results are as follows:

- When applied to a single halo of $5 \times 10^{14}\, M_\odot$ near $z = 0.3$, the inner slope of the density profile can be estimated with a 1-σ accuracy of $14\,\%$ with the linear filter and $19\,\%$ with the scale-adaptive filter, provided the halo concentration is known. Even though this situation is unrealistically idealised, it is promising because it is based on a single halo only.

- Taking the considerable uncertainty in halo concentrations into account increases the 1-σ error to between $25 \ldots 30\,\%$.

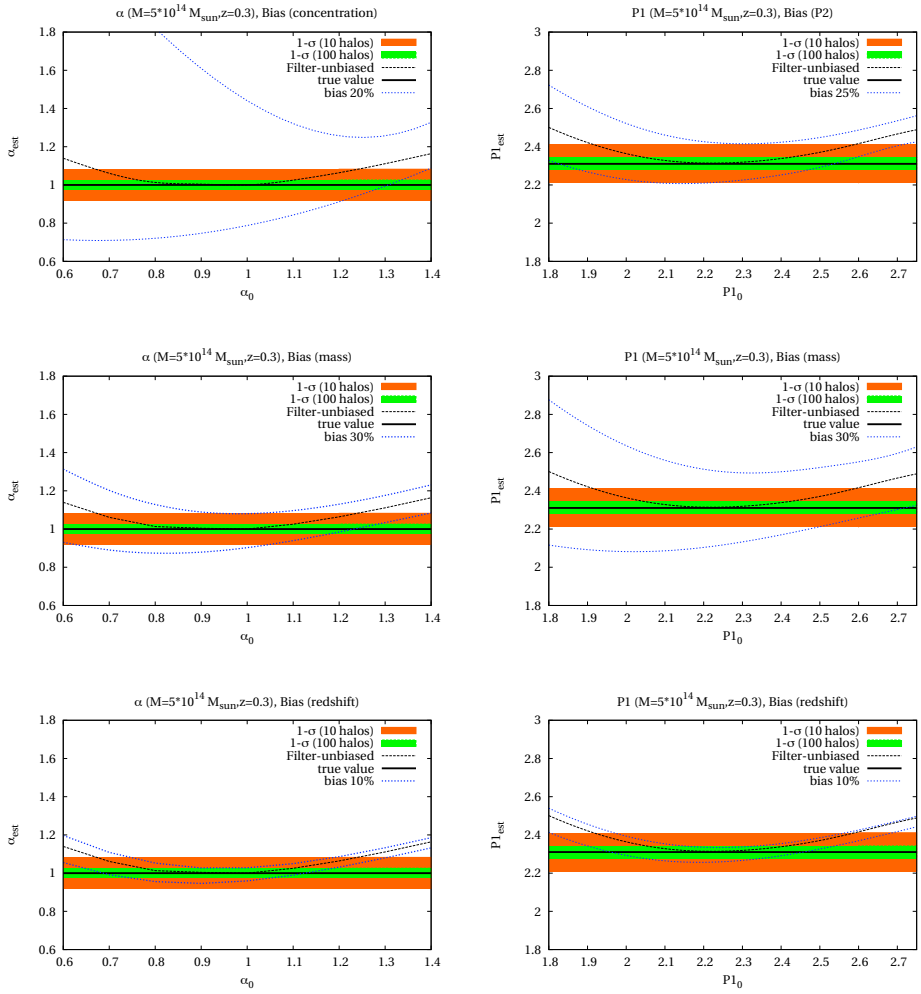

Figure 6.11: *Left panels:* Estimated inner slope of the halo ($\alpha_{\rm est}$) as a function of the fiducial inner slope used in the filter (α_0) with the $1-\sigma$ error calculated for 10 (orange) or 100 (green line) halos using the Monte-Carlo simulations described in Sect. 6.2. The black line shows the real value of the halo's inner slope. The *first panel* shows the bias caused by a fiducial concentration 20 % larger or smaller than the real concentration. The *second panel* shows the bias induced by a 50 % difference between the fiducial and the real halo's mass, while the *third panel* shows the bias caused by a difference of 10 % between the fiducial and the real halo's redshift. *Right panels:* As the left panels, but for the new pair of parameters P_1 and P_2.

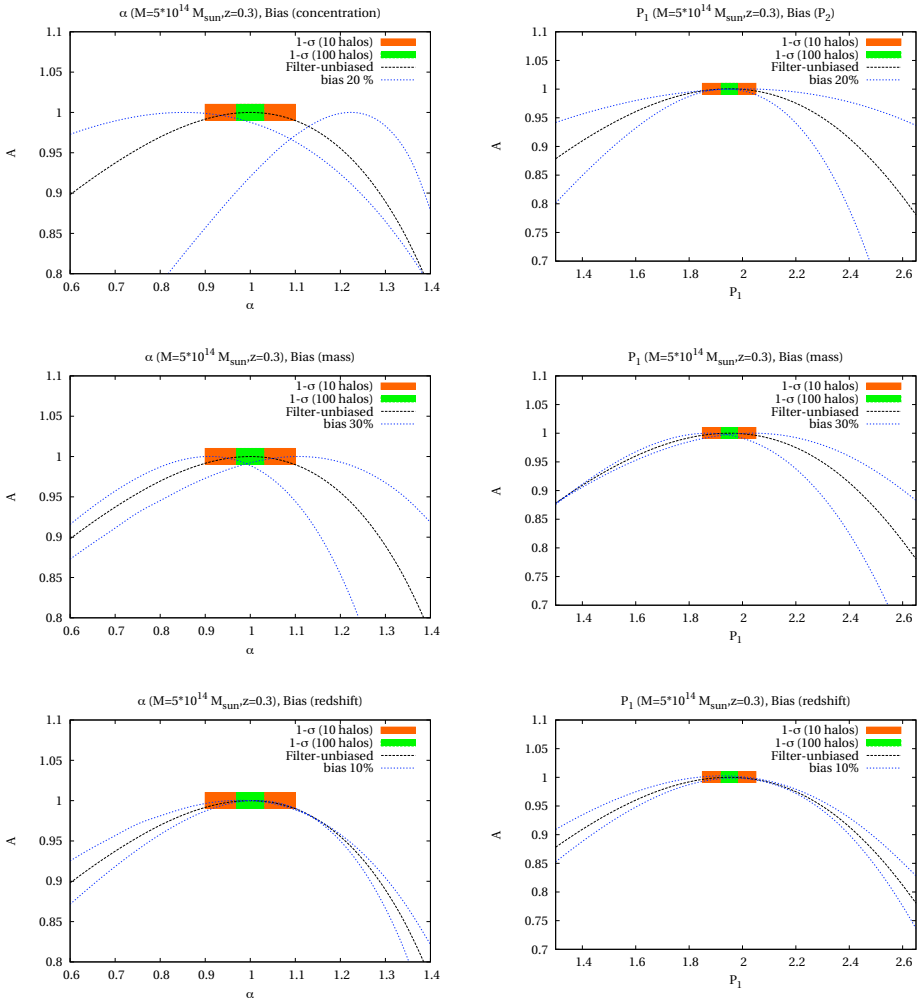

Figure 6.12: Estimated shear amplitude (equation 6.2) normalised to unity as a function of the inner slope (α) (*left panels*) and as a function of $P1$ used in the filter definition (*right panels*). The *black dashed curve* represents the case in which fiducial concentration, mass and redshift used in the filter are correct. The *blue curves* represent the effect of defining the filter with a wrong fiducial value for the concentration (first panel), the mass (second panel) and the redshift (third panel). The errors on the measurement of α were computed by Monte-Carlo simulation (see the text for details) and are rescaled for 10 and 100 halos.

- In reality, the halo concentration is at best roughly known. Based on real data, there is an almost perfect degeneracy between α and the halo-concentration parameter c: if c is assumed to be too large, α will be underestimated and vice versa. Based on lensing data only, this degeneracy cannot be lifted.

- To address this problem, we search for that combination of the parameters α and c that can best be constrained by observations. We set up the Fisher matrix, rotate the two-dimensional parameter space to diagonalise it and identify its smaller eigenvalue as that best-constrained parameter, called P_1. We find $P_1 = 0.95\alpha + 0.30c$ for the linear filter and $P_1 = 0.97\alpha + 0.22c$ for the scale-adaptive filter.

- This parameter P_1 is now constrained with a 1-σ relative accuracy of $\sim 14\,\%$ both with the linear and the scale-adaptive filters and the measurement is almost insensitive to the value of the other parameter P_2.

While these results seem highly promising, in particular when applications to cluster samples rather than individual clusters are envisaged, we consider our study as a first step. While we have taken into account that image ellipticities measure the reduced gravitational shear rather than the shear itself, measuring the reduced shear near the centres of galaxy groups or clusters is severely hampered by the cluster galaxies themselves. It thus appears necessary to stack the signal from several or many clusters to arrive at a reliable estimate for α. Then, clusters with different masses, redshifts and concentration parameters will inevitably be combined, with the tendency to blur the signal. However, the results derived and presented above indicate that the principle of our approach is promising, which consists in combining all available information into a single number, which is thus well constrained. Further studies are required to address the issue of stacking data in this context.

Salimmo sù, el primo e io secondo,
tanto ch'i' vidi de le cose belle
che porta 'l ciel, per un pertugio tondo.
E quindi uscimmo a riveder le stelle[0].

Dante (1265-1321) Inferno XXXIV

7 Conclusions

Weak gravitational lensing is a very powerful tool to study the distribution of matter in the universe and to understand the properties of dark matter halos, the building-blocks of non-linear structure formation. It has a very elegant mathematical treatment in terms of spinorial fields (convergence, shear and flexion), which are related to the derivatives of the lensing potential. Each of these fields can be ultimately related to a particular deformation of a lensed object. Measuring these deformations with high accuracy is one of the greatest challenge for any weak lensing application.

In this Thesis we analysed the KSB (Kaiser et al., 1995) method, which aims at estimating gravitational shear from surface-brightness moments of small and noisy galaxy images. In particular we investigated possible biases coming from the restrictive mathematical assumptions on which this method relies. We identified in particular four main problems:

1. While gravitational shear must be estimated from averaged galaxy images, KSB derives a shear estimate from each individual image and then takes the average. Since the two operations do not commute, KSB gives biased results.

2. KSB implicitly assumes that galaxy ellipticities are small, while weak gravitational lensing assures only that the change in ellipticity due to the shear is small.

3. KSB does not perform any PSF deconvolution, but gives only an approximate correction for the effect of the PSF. We demonstrated that this correction would be equivalent to a proper PSF deconvolution from a circular PSF only in the case of a circular source, otherwise the improper PSF correction lowers the shear estimate

[0] we climbed he first, I following until I saw/through a round opening, some of those things/of beauty Heaven bears. It was from there/that we emerged, to see once more the stars.

4. KSB assumes that the PSF can be described by the convolution of a compact anisotropic kernel and a large isotropic kernel. We showed that is not possible to extend the formalism to allow more precise corrections in case the PSF since that would imply calculation of the derivatives of the observed surface brightness, which is not feasible given the amount of noise in the data.

We showed that the effects of assumptions (2) and (3) partially counteract in a way dependent on the width of the weight function used to measure the moments and of the PSF. We quantitatively demonstrate the biases due to all assumptions, extend the KSB approach consistently to third order in the shear and ellipticity and show that this extension lowers the biases substantially.

The inability to improve the PSF deconvolution performed by KSB pushed towards a development of a new method, called DEIMOS. It maintains the strengths of a model independent approach by working with multipole moments of the apparent brightness distribution, but being based on a mathematically exact deconvolution of the moments of galaxies from the PSF, has the big advantage of not relying on any assumption about the shape of the PSF.

The (de)convolution equations we found out, are exact for unweighted moments only, while in practice a compact weight function needs to be applied to the noisy images to ensure that the moment measurement yields significant results. We showed that the change of the moments caused by the application of the weight function can then be corrected by considering higher-order weighted moments of the same source. Because of the form of the deconvolution equations, even an incomplete weighting correction leads to an excellent shear estimation if galaxies and PSF are measured with a weight function of identical size. We demonstrated the accuracy and capabilities of this new method in the context of weak gravitational lensing measurements with a set of specialized tests and show its competitive performance on the GREAT08 challenge data (Bridle et al., 2010).

The formalism on which DEIMOS is based can easily be extended to measure gravitational flexion (the next higher order distortion effects after shear and convergence). The accuracy and the precision that DEIMOS can achieve in the measurements of third (and fourth) moments, necessary to build up any flexion estimator are still unclear and further studies are planned in this direction.

We investigated in this Thesis some interesting theoretical aspects regarding flexion measurements in cluster environments. We showed in particular that close to cluster centres, where the shear and the convergence

are high, the $\mathcal{F}$-flexion and the $\mathcal{G}$-flexion fields can be contaminated by the appearance of other spin-1 and spin-3 fields caused by cross talk between (reduced) shear and flexion. We demonstrated that the contamination can be up to 50% and we showed how it depends on the morphological properties of the source population. Taking into account this effect is of extreme importance when the "measured flexion" is compared to the true flexion.

Having reliable shear (and flexion) estimation is crucial to predict the properties of dark matter halos. In this Thesis we investigate in particular how much gravitational shear is able to constrain their density profiles, as predicted by numerical simulations (Navarro et al., 1997; Moore et al., 1998).

We constructed two linear filtering techniques based on weak gravitational lensing to constrain the inner slope α of the density profile of dark-matter halos, assuming that the profile has an outer slope of r^{-3}. Both methods combine all available information into an estimate of this single number, without the necessity of measuring and then fitting the complete shear profile, which might be problematic given the sparseness of lensing information near the core of galaxy clusters. Furthermore the contamination of the cluster shear signal by the large scale structures can be naturally taken into account. We found that, under idealised assumptions, α is constrained to $\sim 15\%$ if the halo concentration c is known, and to $\lesssim 30\%$ if not. We argue that the inevitable degeneracy between density-profile slope and halo concentration cannot be lifted under realistic conditions, and showed by means of Fisher-matrix methods which linear combination of α and c is best constrained by our filtering of lensing data. This defines a new parameter, called P_1, which is then constrained to $\sim 15\%$ for a single massive halo. The achievable accuracy for a single cluster suggests that if the signals of many halos can be stacked, their density profiles should thus be well constrained by the linear filters proposed here with the advantage, in contrast with strong lensing analysis, to be insensitive to the cluster substructures.

It is however unclear which is the best way to stack data in this context. In particular the estimation of the biases that stacking can introduce in the final measurement has been left for further studies. The filtering techniques, developed in this Thesis for the shear, can be extended to include flexion with the aim to combine shear and flexion information in the inner part of galaxy clusters to constrain the inner slope of dark matter halo.

Appendix A

In this Appendix, we list expressions for the tensors defined in Chapter 4 in terms of moments of the light distribution:

$$P_{11} = -\frac{2\chi_1 L_1}{Tr(Q)} - 2\chi_1^2 + 2\frac{B_{11}}{Tr(Q)} + 2 \tag{7.1}$$

$$P_{12} = -2\frac{\chi_1 L_2}{Tr(Q)} - 2\chi_1\chi_2 + 4\frac{B_{11}}{Tr(Q)} \tag{7.2}$$

$$P_{22} = -2\frac{\chi_2 L_2}{Tr(Q)} - 2\chi_2^2 + 8\frac{Q'_{1122}}{Tr(Q)} + 2 \tag{7.3}$$

$$R_{111} = 2\frac{K_{11}\chi_1}{Tr(Q)} + 4\frac{B_{11}\chi_1}{Tr(Q)} - 2\frac{D_{111}}{Tr(Q)} - 4\frac{L_1}{Tr(Q)} \tag{7.4}$$

$$R_{112} = 2\frac{K_{12}\chi_1}{Tr(Q)} + 4\frac{B_{12}\chi_1}{Tr(Q)} - 2\frac{D_{112}}{Tr(Q)} \tag{7.5}$$

$$R_{121} = 2\frac{K_{12}\chi_1}{Tr(Q)} + 4\frac{B_{12}\chi_1}{Tr(Q)} - 2\frac{D_{112}}{Tr(Q)} - 4\frac{L_2}{Tr(Q)} \tag{7.6}$$

$$R_{211} = 2\frac{K_{11}\chi_2}{Tr(Q)} + 4\frac{B_{11}\chi_2}{Tr(Q)} - 2\frac{D_{112}}{Tr(Q)} \tag{7.7}$$

$$R_{122} = 2\frac{K_{22}\chi_1}{Tr(Q)} + 16\frac{Q'_{1122}\chi_1}{Tr(Q)} - 2\frac{D_{122}}{Tr(Q)} \tag{7.8}$$

$$R_{221} = 2\frac{K_{12}\chi_2}{Tr(Q)} + 4\frac{B_{12}\chi_2}{Tr(Q)} - 2\frac{D_{122}}{Tr(Q)} \tag{7.9}$$

$$R_{212} = 2\frac{K_{12}\chi_2}{Tr(Q)} + 4\frac{B_{12}\chi_2}{Tr(Q)} - 2\frac{D_{122}}{Tr(Q)} - 4\frac{L_1}{Tr(Q)} \tag{7.10}$$

$$R_{222} = 2\frac{K_{22}\chi_2}{tr(Q)} + 16\frac{Q'_{1122}\chi_2}{tr(Q)} - 16\frac{Q''_{111222}}{Tr(Q)} - 4\frac{L_2}{Tr(Q)} \tag{7.11}$$

$$L_1 = Q'_{1111} - Q'_{2222} \tag{7.12}$$

$$L_2 = 2(Q'_{1112} + Q'_{2221}) \tag{7.13}$$

$$B_{11} = Q'_{1111} - 2Q'_{1122} + Q'_{2222} \tag{7.14}$$

$$B_{12} = B_{21} = 2(Q'_{1112} - Q'_{1222}) \tag{7.15}$$

$$B_{22} = 4Q'_{1122} \tag{7.16}$$

$$K_{11} = (Q''_{111111} - Q''_{111122} - Q''_{112222} + Q''_{222222}) \tag{7.17}$$

$$K_{12} = K_{21} = 2(Q''_{111112} - Q''_{122222}) \tag{7.18}$$

$$K_{22} = 4(Q''_{111122} + Q''_{112222}) \tag{7.19}$$

$$D_{111} = Q''_{111111} - 3Q''_{111122} + 3Q''_{111122} - Q''_{222222} \tag{7.20}$$

$$\begin{aligned} D_{112} &= D_{121} = D_{211} = \\ &= 2(Q''_{111112} - 2Q''_{111222} + Q''_{222221}) \end{aligned} \tag{7.21}$$

$$D_{122} = D_{212} = D_{221} = 4(Q''_{111122} - Q''_{112222}) \tag{7.22}$$

$$D_{222} = 8Q''_{111222} \tag{7.23}$$

$$\begin{aligned} U_{1111} &= Q'''_{11111111} - 4Q'''_{11111122} + 6Q'''_{11112222} \\ &- 4Q'''_{11222222} + Q'''_{22222222} \end{aligned} \tag{7.24}$$

$$\begin{aligned} U_{2111} &= 2(Q'''_{11111112} - 3Q'''_{11111222} \\ &+ 3Q'''_{11122222} - Q'''_{12222222}) \end{aligned} \tag{7.25}$$

$$U_{1211} = U_{1121} = U_{1112} = U_{2111} \tag{7.26}$$

$$U_{2211} = 4(Q'''_{11111122} - 2Q'''_{11112222} + Q'''_{11222222}) \tag{7.27}$$

$$U_{2112} = U_{2121} = U_{1122} = U_{1221} = U_{1212} = U_{2211} \tag{7.28}$$

$$U_{2221} = 8(Q'''_{11111222} - Q'''_{11122222}) \tag{7.29}$$

$$U_{2122} = U_{2212} = U_{1222} = U_{2221} \tag{7.30}$$

$$U_{2222} = 16Q'''_{11112222} \tag{7.31}$$

Note that the moments $Q'_{ij..k}$ have to be computed using the first derivative of the weight function with respect to $\vec{\theta}^2$. Similarly, $Q''_{ij..k}$ must be computed using the second derivatives of the weight function.

Bibliography

Abazajian, K., Adelman-McCarthy, J. K., Agüeros, M. A., Allam, S. S., Anderson, S. F., Annis, J., Bahcall, N. A., Baldry, I. K., Bastian, S., Berlind, A., Bernardi, M., Blanton, M. R., Blythe, N., Bochanski, J. J., Jr., Boroski, W. N., Brewington, H., Briggs, J. W., Brinkmann, J., Brunner, R. J., Budavári, T., Carey, L. N., Carr, M. A., Castander, F. J., Chiu, K., Collinge, M. J., Connolly, A. J., Covey, K. R., Csabai, I., Dalcanton, J. J., Dodelson, S., Doi, M., Dong, F., Eisenstein, D. J., Evans, M. L., Fan, X., Feldman, P. D., Finkbeiner, D. P., Friedman, S. D., Frieman, J. A., Fukugita, M., Gal, R. R., Gillespie, B., Glazebrook, K., Gonzalez, C. F., Gray, J., Grebel, E. K., Grodnicki, L., Gunn, J. E., Gurbani, V. K., Hall, P. B., Hao, L., Harbeck, D., Harris, F. H., Harris, H. C., Harvanek, M., Hawley, S. L., Heckman, T. M., Helmboldt, J. F., Hendry, J. S., Hennessy, G. S., Hindsley, R. B., Hogg, D. W., Holmgren, D. J., Holtzman, J. A., Homer, L., Hui, L., Ichikawa, S.-i., Ichikawa, T., Inkmann, J. P., Ivezić, Ž., Jester, S., Johnston, D. E., Jordan, B., Jordan, W. P., Jorgensen, A. M., Jurić, M., Kauffmann, G., Kent, S. M., Kleinman, S. J., Knapp, G. R., Kniazev, A. Y., Kron, R. G., Krzesiński, J., Kunszt, P. Z., Kuropatkin, N., Lamb, D. Q., Lampeitl, H., Laubscher, B. E., Lee, B. C., Leger, R. F., Li, N., Lidz, A., Lin, H., Loh, Y.-S., Long, D. C., Loveday, J., Lupton, R. H., Malik, T., Margon, B., McGehee, P. M., McKay, T. A., Meiksin, A., Miknaitis, G. A., Moorthy, B. K., Munn, J. A., Murphy, T., Nakajima, R., Narayanan, V. K., Nash, T., Neilsen, E. H., Jr., Newberg, H. J., Newman, P. R., Nichol, R. C., Nicinski, T., Nieto-Santisteban, M., Nitta, A., Odenkirchen, M., Okamura, S., Ostriker, J. P., Owen, R., Padmanabhan, N., Peoples, J., Pier, J. R., Pindor, B., Pope, A. C., Quinn, T. R., Rafikov, R. R., Raymond, S. N., Richards, G. T., Richmond, M. W., Rix, H.-W., Rockosi, C. M., Schaye, J., Schlegel, D. J., Schneider, D. P., Schroeder, J., Scranton, R., Sekiguchi, M., Seljak, U., Sergey, G., Sesar, B., Sheldon, E., Shimasaku, K., Siegmund, W. A., Silvestri, N. M., Sinisgalli, A. J., Sirko, E., Smith, J. A., Smolčić, V., Snedden, S. A., Stebbins, A., Steinhardt, C., Stinson, G., Stoughton, C., Strateva, I. V., Strauss, M. A., SubbaRao, M., Szalay, A. S., Szapudi, I., Szkody, P., Tasca, L., Tegmark, M., Thakar, A. R., Tremonti, C., Tucker, D. L., Uomoto, A., Vanden Berk, D. E., Vandenberg, J., Vogeley, M. S., Voges, W., Vogt, N. P., Walkowicz, L. M., Weinberg, D. H., West, A. A., White, S. D. M., Wilhite, B. C., Willman, B., Xu, Y., Yanny, B., Yarger, J., Yasuda, N., Yip, C.-W., Yocum, D. R., York, D. G., Zakamska, N. L., Zehavi, I., Zheng, W., Zibetti, S., and Zucker, D. B. 2003. "The First Data Release of the Sloan Digital Sky Survey." *AJ* 126:2081–2086. doi:10.1086/378165.

Albrecht, A., Bernstein, G., Cahn, R., Freedman, W. L., Hewitt, J., Hu, W.,

Huth, J., Kamionkowski, M., Kolb, E. W., Knox, L., Mather, J. C., Staggs, S., and Suntzeff, N. B. 2006. "Report of the Dark Energy Task Force." *ArXiv Astrophysics e-prints* .

Amara, A. and Réfrégier, A. 2008. "Systematic bias in cosmic shear: extending the Fisher matrix." *MNRAS* 391:228–236. doi:10.1111/j.1365-2966.2008.13880.x.

Bacon, D. J., Goldberg, D. M., Rowe, B. T. P., and Taylor, A. N. 2006. "Weak gravitational flexion." *MNRAS* 365:414–428. doi:10.1111/j.1365-2966.2005.09624.x.

Bacon, D. J., Refregier, A. R., and Ellis, R. S. 2000. "Detection of weak gravitational lensing by large-scale structure." *MNRAS* 318:625–640. doi:10.1046/j.1365-8711.2000.t01-1-03851.x.

Bacon, D. J., Taylor, A. N., Brown, M. L., Gray, M. E., Wolf, C., Meisenheimer, K., Dye, S., Wisotzki, L., Borch, A., and Kleinheinrich, M. 2005. "Evolution of the dark matter distribution with three-dimensional weak lensing." *MNRAS* 363:723–733. doi:10.1111/j.1365-2966.2005.09420.x.

Bartelmann, M. 1996. "Arcs from a universal dark-matter halo profile." *A&A* 313:697–702.

—. 2010. "The dark Universe." *Reviews of Modern Physics* 82:331–382. doi:10.1103/RevModPhys.82.331.

Bartelmann, M., Narayan, R., Seitz, S., and Schneider, P. 1996. "Maximum-likelihood Cluster Reconstruction." *ApJ* 464:L115+. doi:10.1086/310114.

Bartelmann, M. and Schneider, P. 2001. "Weak gravitational lensing." *Phys. Rep.* 340:291–472.

Beckwith, S. V. W., Stiavelli, M., Koekemoer, A. M., Caldwell, J. A. R., Ferguson, H. C., Hook, R., Lucas, R. A., Bergeron, L. E., Corbin, M., Jogee, S., Panagia, N., Robberto, M., Royle, P., Somerville, R. S., and Sosey, M. 2006. "The Hubble Ultra Deep Field." *AJ* 132:1729–1755. doi:10.1086/507302.

Benjamin, J., Heymans, C., Semboloni, E., van Waerbeke, L., Hoekstra, H., Erben, T., Gladders, M. D., Hetterscheidt, M., Mellier, Y., and Yee, H. K. C. 2007. "Cosmological constraints from the $100 - deg^2$ weak-lensing survey." *MNRAS* 381:702–712. doi:10.1111/j.1365-2966.2007.12202.x.

Bernstein, G. M. 2010. "Shape measurement biases from underfitting and ellipticity gradients." *MNRAS* 406:2793–2804. doi:10.1111/j.1365-2966.2010.16883.x.

Bernstein, G. M. and Jarvis, M. 2002. "Shapes and Shears, Stars and Smears: Optimal Measurements for Weak Lensing." *AJ* 123:583–618. doi:10.1086/338085.

Borgani, S., Dolag, K., Murante, G., Cheng, L.-M., Springel, V., Diaferio, A., Moscardini, L., Tormen, G., Tornatore, L., and Tozzi, P. 2006. "Hot and cooled baryons in smoothed particle hydrodynamic simulations of galaxy clusters: physics and numerics." *MNRAS* 367:1641–1654. doi:10.1111/j.1365-2966.2006.10075.x.

Bridle, S., Balan, S. T., Bethge, M., Gentile, M., Harmeling, S., Heymans, C., Hirsch, M., Hosseini, R., Jarvis, M., and Kirk, D. 2009. "Results of the GREAT08 Challenge: An image analysis competition for cosmological lensing." *ArXiv e-prints 0908.0945* .

Bridle, S., Balan, S. T., Bethge, M., Gentile, M., Harmeling, S., Heymans, C., Hirsch, M., Hosseini, R., Jarvis, M., Kirk, D., Kitching, T., Kuijken, K., Lewis, A., Paulin-Henriksson, S., Schölkopf, B., Velander, M., Voigt, L., Witherick, D., Amara, A., Bernstein, G., Courbin, F., Gill, M., Heavens, A., Mandelbaum, R., Massey, R., Moghaddam, B., Rassat, A., Réfrégier, A., Rhodes, J., Schrabback, T., Shawe-Taylor, J., Shmakova, M., van Waerbeke, L., and Wittman, D. 2010. "Results of the GREAT08 Challenge: an image analysis competition for cosmological lensing." *MNRAS* 405:2044–2061. doi:10.1111/j.1365-2966.2010.16598.x.

Bridle, S. L., Crittenden, R., Melchiorri, A., Hobson, M. P., Kneissl, R., and Lasenby, A. N. 2002. "Analytic marginalization over CMB calibration and beam uncertainty." *MNRAS* 335:1193–1200. doi:10.1046/j.1365-8711.2002.05709.x.

Broadhurst, T., Benítez, N., Coe, D., Sharon, K., Zekser, K., White, R., Ford, H., and Bouwens, R. 2005. "Strong-Lensing Analysis of A1689 from Deep Advanced Camera Images." *ApJ* 621:53–88. doi:10.1086/426494.

Brown, M. L., Taylor, A. N., Bacon, D. J., Gray, M. E., Dye, S., Meisenheimer, K., and Wolf, C. 2003. "The shear power spectrum from the COMBO-17 survey." *MNRAS* 341:100–118. doi:10.1046/j.1365-8711.2003.06237.x.

Bullock, J. S., Dekel, A., Kolatt, T. S., Kravtsov, A. V., Klypin, A. A., Porciani, C., and Primack, J. R. 2001a. "A Universal Angular Momentum Profile for Galactic Halos." *ApJ* 555:240–257. doi:10.1086/321477.

Bullock, J. S., Kolatt, T. S., Sigad, Y., Somerville, R. S., Kravtsov, A. V., Klypin, A. A., Primack, J. R., and Dekel, A. 2001b. "Profiles of dark haloes: evolution, scatter and environment." *MNRAS* 321:559–575. doi:10.1046/j.1365-8711.2001.04068.x.

Cacciato, M., Bartelmann, M., Meneghetti, M., and Moscardini, L. 2006. "Combining weak and strong lensing in cluster potential reconstruction." *A&A* 458:349–356. doi:10.1051/0004-6361:20054582.

Carroll, S. M., Press, W. H., and Turner, E. L. 1992. "The cosmological constant." *ARAA* 30:499–542. doi:10.1146/annurev.aa.30.090192.002435.

Coles, P. and Lucchin, F. 2002. *Cosmology: The Origin and Evolution of Cosmic Structure, Second Edition*. Cosmology: The Origin and Evolution of Cosmic Structure, Second Edition, by Peter Coles, Francesco Lucchin, pp. 512. ISBN 0-471-48909-3. Wiley-VCH , July 2002.

Colless, M., Dalton, G., Maddox, S., Sutherland, W., Norberg, P., Cole, S., Bland-Hawthorn, J., Bridges, T., Cannon, R., Collins, C., Couch, W., Cross, N., Deeley, K., De Propris, R., Driver, S. P., Efstathiou, G., Ellis, R. S., Frenk, C. S., Glazebrook, K., Jackson, C., Lahav, O., Lewis, I., Lumsden, S., Madgwick, D., Peacock, J. A., Peterson, B. A., Price, I., Seaborne, M., and Taylor, K. 2001. "The 2dF Galaxy Redshift Survey: spectra and redshifts." *MNRAS* 328:1039–1063. doi:10.1046/j.1365-8711.2001.04902.x.

Crittenden, R. G., Natarajan, P., Pen, U.-L., and Theuns, T. 2001. "Spin-induced Galaxy Alignments and Their Implications for Weak-Lensing Measurements." *ApJ* 559:552–571. doi:10.1086/322370.

—. 2002. "Discriminating Weak Lensing from Intrinsic Spin Correlations Using the Curl-Gradient Decomposition." *ApJ* 568:20–27. doi:10.1086/338838.

Diemand, J., Moore, B., and Stadel, J. 2004. "Convergence and scatter of cluster density profiles." *MNRAS* 353:624–632. doi:10.1111/j.1365-2966.2004.08094.x.

Eifler, T., Schneider, P., and Hartlap, J. 2009. "Dependence of cosmic shear covariances on cosmology. Impact on parameter estimation." *A&A* 502:721–731. doi:10.1051/0004-6361/200811276.

Eke, V. R., Navarro, J. F., and Steinmetz, M. 2001. "The Power Spectrum Dependence of Dark Matter Halo Concentrations." *ApJ* 554:114–125. doi:10.1086/321345.

Erben, T., Van Waerbeke, L., Bertin, E., Mellier, Y., and Schneider, P. 2001. "How accurately can we measure weak gravitational shear?" *A&A* 366:717–735. doi:10.1051/0004-6361:20010013.

Etherington, I. M. H. 1933. "On the Definition of Distance in General Relativity." *Philosophical Magazine* 15:761–+.

Flusser, Jan and Suk, Tomáš. 1998. "Degraded Image Analysis: An Invariant Approach." *IEEE Trans. Pattern Anal. Mach. Intell.* 20:590–603. ISSN 0162-8828. doi:http://dx.doi.org/10.1109/34.683773.

Fu, L., Semboloni, E., Hoekstra, H., Kilbinger, M., van Waerbeke, L., Tereno, I., Mellier, Y., Heymans, C., Coupon, J., Benabed, K., Benjamin, J., Bertin, E., and Doré, O. 2008. "Very weak lensing in the CFHTLS wide: cosmology from cosmic shear in the linear regime." *A&A* 479:9–25. doi:10.1051/0004-6361:20078522.

Gottlöber, S., Yepes, G., Khalatyan, A., Sevilla, R., and Turchaninov, V. 2006. "Dark and baryonic matter in the MareNostrum Universe." In C. Manoz & G. Yepes (ed.), *The Dark Side of the Universe*, volume 878 of *American Institute of Physics Conference Series*, 3–9. doi:10.1063/1.2409061.

Hamana, T., Colombi, S. T., Thion, A., Devriendt, J. E. G. T., Mellier, Y., and Bernardeau, F. 2002. "Source-lens clustering effects on the skewness of the lensing convergence." *MNRAS* 330:365–377. doi:10.1046/j.1365-8711.2002.05103.x.

Hamilton, A. J. S. 2001. "Formulae for growth factors in expanding universes containing matter and a cosmological constant." *MNRAS* 322:419–425. doi:10.1046/j.1365-8711.2001.04137.x.

Harrison, E. R. 1970. "Fluctuations at the Threshold of Classical Cosmology." *Phys. Rev. D* 1:2726–2730. doi:10.1103/PhysRevD.1.2726.

Heavens, A. 2003. "3D weak lensing." *MNRAS* 343:1327–1334. doi:10.1046/j.1365-8711.2003.06780.x.

Heavens, A. and Peacock, J. 1988. "Tidal torques and local density maxima." *MNRAS* 232:339–360.

Heymans, C., Van Waerbeke, L., Bacon, D., Berge, J., Bernstein, G., Bertin, E., Bridle, S., Brown, M. L., Clowe, D., Dahle, H., Erben, T., Gray, M., Hetterscheidt, M., Hoekstra, H., Hudelot, P., Jarvis, M., Kuijken, K., Margoniner, V., Massey, R., Mellier, Y., Nakajima, R., Refregier, A., Rhodes, J., Schrabback, T., and Wittman, D. 2006. "The Shear Testing

Programme - I. Weak lensing analysis of simulated ground-based observations." *MNRAS* 368:1323–1339. doi:10.1111/j.1365-2966.2006.10198.x.

Hirata, C. M. and Seljak, U. 2004. "Intrinsic alignment-lensing interference as a contaminant of cosmic shear." *Phys. Rev. D* 70:063526–+. doi:10.1103/PhysRevD.70.063526.

Hoekstra, H. 2004. "The effect of imperfect models of point spread function anisotropy on cosmic shear measurements." *MNRAS* 347:1337–1344. doi:10.1111/j.1365-2966.2004.07327.x.

Hoekstra, H., Franx, M., Kuijken, K., and Squires, G. 1998. "Weak Lensing Analysis of CL 1358+62 Using Hubble Space Telescope Observations." *ApJ* 504:636–+. doi:10.1086/306102.

Hu, W. 1999. "Power Spectrum Tomography with Weak Lensing." *ApJ* 522:L21–L24. doi:10.1086/312210.

Hubble, E. 1929. "A Relation between Distance and Radial Velocity among Extra-Galactic Nebulae." *Proceedings of the National Academy of Science* 15:168–173. doi:10.1073/pnas.15.3.168.

Jain, B., Jarvis, M., and Bernstein, G. 2006. "PSF anisotropy and systematic errors in weak lensing surveys." *JCAP* 2:1–+. doi:10.1088/1475-7516/2006/02/001.

Jarvis, M., Bernstein, G. M., Fischer, P., Smith, D., Jain, B., Tyson, J. A., and Wittman, D. 2003. "Weak-Lensing Results from the 75 Square Degree Cerro Tololo Inter-American Observatory Survey." *AJ* 125:1014–1032. doi:10.1086/367799.

Jarvis, M. and Jain, B. 2004. "Principal Component Analysis of PSF Variation in Weak Lensing Surveys." *ArXiv Astrophysics e-prints* .

Kaiser, N. 1992. "Weak gravitational lensing of distant galaxies." *ApJ* 388:272–286. doi:10.1086/171151.

—. 2000. "A New Shear Estimator for Weak-Lensing Observations." *ApJ* 537:555–577. doi:10.1086/309041.

Kaiser, N., Squires, G., and Broadhurst, T. 1995. "A Method for Weak Lensing Observations." *ApJ* 449:460–+. doi:10.1086/176071.

Kathinka Dalland Evans, A. and Bridle, S. 2008. "A Detection of Dark Matter Halo Ellipticity using Galaxy Cluster Lensing in SDSS." *ApJ, submitted (arXiv:0806.2723)* .

Keeton, C. R. and Madau, P. 2001. "Lensing Constraints on the Cores of Massive Dark Matter Halos." *ApJ* 549:L25–L28. doi:10.1086/319136.

Kitching, T. D., Miller, L., Heymans, C. E., van Waerbeke, L., and Heavens, A. F. 2008. "Bayesian galaxy shape measurement for weak lensing surveys - II. Application to simulations." *MNRAS* 390:149–167. doi:10.1111/j.1365-2966.2008.13628.x.

Komatsu, E., Dunkley, J., Nolta, M. R., Bennett, C. L., Gold, B., Hinshaw, G., Jarosik, N., Larson, D., Limon, M., Page, L., Spergel, D. N., Halpern, M., Hill, R. S., Kogut, A., Meyer, S. S., Tucker, G. S., Weiland, J. L., Wollack, E., and Wright, E. L. 2009. "Five-Year Wilkinson Microwave Anisotropy Probe Observations: Cosmological Interpretation." *ApJS* 180:330–376. doi:10.1088/0067-0049/180/2/330.

Kowalski, M., Rubin, D., Aldering, G., Agostinho, R. J., Amadon, A., Amanullah, R., Balland, C., Barbary, K., Blanc, G., Challis, P. J., Conley, A., Connolly, N. V., Covarrubias, R., Dawson, K. S., Deustua, S. E., Ellis, R., Fabbro, S., Fadeyev, V., Fan, X., Farris, B., Folatelli, G., Frye, B. L., Garavini, G., Gates, E. L., Germany, L., Goldhaber, G., Goldman, B., Goobar, A., Groom, D. E., Haissinski, J., Hardin, D., Hook, I., Kent, S., Kim, A. G., Knop, R. A., Lidman, C., Linder, E. V., Mendez, J., Meyers, J., Miller, G. J., Moniez, M., Mourão, A. M., Newberg, H., Nobili, S., Nugent, P. E., Pain, R., Perdereau, O., Perlmutter, S., Phillips, M. M., Prasad, V., Quimby, R., Regnault, N., Rich, J., Rubenstein, E. P., Ruiz-Lapuente, P., Santos, F. D., Schaefer, B. E., Schommer, R. A., Smith, R. C., Soderberg, A. M., Spadafora, A. L., Strolger, L.-G., Strovink, M., Suntzeff, N. B., Suzuki, N., Thomas, R. C., Walton, N. A., Wang, L., Wood-Vasey, W. M., and Yun, J. L. 2008. "Improved Cosmological Constraints from New, Old, and Combined Supernova Data Sets." *ApJ* 686:749–778. doi:10.1086/589937.

Kuijken, K. 1999a. "Weak weak lensing: correcting weak shear measurements accurately for PSF anisotropy." *A&A* 352:355–362.

—. 1999b. "Weak weak lensing: correcting weak shear measurements accurately for PSF anisotropy." *A&A* 352:355–362.

Lee, J. and Lee, B. 2008. "The Variation of Galaxy Morphological Type with Environmental Shear." *ApJ* 688:78–84. doi:10.1086/592181.

Limber, D. N. 1953. "The Analysis of Counts of the Extragalactic Nebulae in Terms of a Fluctuating Density Field." *ApJ* 117:134–+. doi:10.1086/145672.

Luppino, G. A. and Kaiser, N. 1997. "Detection of Weak Lensing by a Cluster of Galaxies at Z = 0.83." *ApJ* 475:20–+. doi:10.1086/303508.

Lynds, R. and Petrosian, V. 1986. "Giant Luminous Arcs in Galaxy Clusters." In *Bulletin of the American Astronomical Society*, volume 18 of *Bulletin of the American Astronomical Society*, 1014–+.

Mandelbaum, R., Seljak, U., Cool, R. J., Blanton, M., Hirata, C. M., and Brinkmann, J. 2006. "Density profiles of galaxy groups and clusters from SDSS galaxy-galaxy weak lensing." *MNRAS* 372:758–776. doi:10.1111/j.1365-2966.2006.10906.x.

Massey, R., Heymans, C., Bergé, J., Bernstein, G., Bridle, S., Clowe, D., Dahle, H., Ellis, R., Erben, T., Hetterscheidt, M., High, F. W., Hirata, C., Hoekstra, H., Hudelot, P., Jarvis, M., Johnston, D., Kuijken, K., Margoniner, V., Mandelbaum, R., Mellier, Y., Nakajima, R., Paulin-Henriksson, S., Peeples, M., Roat, C., Refregier, A., Rhodes, J., Schrabback, T., Schirmer, M., Seljak, U., Semboloni, E., and van Waerbeke, L. 2007a. "The Shear Testing Programme 2: Factors affecting high-precision weak-lensing analyses." *MNRAS* 376:13–38. doi:10.1111/j.1365-2966.2006.11315.x.

Massey, R., Rowe, B., Refregier, A., Bacon, D. J., and Bergé, J. 2007b. "Weak gravitational shear and flexion with polar shapelets." *MNRAS* 380:229–245. doi:10.1111/j.1365-2966.2007.12072.x.

Maturi, M., Meneghetti, M., Bartelmann, M., Dolag, K., and Moscardini, L. 2005. "An optimal filter for the detection of galaxy clusters through weak lensing." *A&A* 442:851–860. doi:10.1051/0004-6361:20042600.

Melchior, P., Andrae, R., Maturi, M., and Bartelmann, M. 2009. "Deconvolution with shapelets." *A&A* 493:727–734. doi:10.1051/0004-6361:200810472.

Melchior, P., Böhnert, A., Lombardi, M., and Bartelmann, M. 2010a. "Limitations on shapelet-based weak-lensing measurements." *A&A* 510:A75+. doi:10.1051/0004-6361/200912785.

Melchior, P., Viola, M., Schäfer, B. M., and Bartelmann, M. 2010b. "Weak gravitational lensing with DEIMOS." *ArXiv e-prints* .

Meneghetti, M., Bartelmann, M., Jenkins, A., and Frenk, C. 2007. "The effects of ellipticity and substructure on estimates of cluster density profiles based on lensing and kinematics." *MNRAS* 381:171–186. doi:10.1111/j.1365-2966.2007.12225.x.

Merten, J., Cacciato, M., Meneghetti, M., Mignone, C., and Bartelmann, M. 2009. "Combining weak and strong cluster lensing: applications to simulations and MS 2137." *A&A* 500:681–691. doi:10.1051/0004-6361/200810372.

Miller, L., Kitching, T. D., Heymans, C., Heavens, A. F., and van Waerbeke, L. 2007. "Bayesian galaxy shape measurement for weak lensing surveys - I. Methodology and a fast-fitting algorithm." *MNRAS* 382:315–324. doi:10.1111/j.1365-2966.2007.12363.x.

Moore, B., Governato, F., Quinn, T., Stadel, J., and Lake, G. 1998. "Resolving the Structure of Cold Dark Matter Halos." *ApJ* 499:L5+. doi:10.1086/311333.

Munshi, D., Valageas, P., van Waerbeke, L., and Heavens, A. 2008. "Cosmology with weak lensing surveys." *Phys. Rep.* 462:67–121. doi:10.1016/j.physrep.2008.02.003.

Nakajima, R. and Bernstein, G. 2007. "Shear Recovery Accuracy in Weak-Lensing Analysis with the Elliptical Gauss-Laguerre Method." *AJ* 133:1763–1779. doi:10.1086/511957.

Navarro, J. F., Frenk, C. S., and White, S. D. M. 1997. "A Universal Density Profile from Hierarchical Clustering." *ApJ* 490:493–+. doi:10.1086/304888.

Neto, A. F., Gao, L., Bett, P., Cole, S., Navarro, J. F., Frenk, C. S., White, S. D. M., Springel, V., and Jenkins, A. 2007. "The statistics of Λ CDM halo concentrations." *MNRAS* 381:1450–1462. doi:10.1111/j.1365-2966.2007.12381.x.

Newman, E. and Penrose, R. 1962. "An Approach to Gravitational Radiation by a Method of Spin Coefficients." *Journal of Mathematical Physics* 3:566–578. doi:10.1063/1.1724257.

Okumura, T., Jing, Y. P., and Li, C. 2009. "Intrinsic Ellipticity Correlation of SDSS Luminous Red Galaxies and Misalignment with Their Host Dark Matter Halos." *ApJ* 694:214–221. doi:10.1088/0004-637X/694/1/214.

Okura, Y. and Futamase, T. 2009. "A New Method for Measuring Weak Gravitational Lensing Shear Using Higher Order Spin-2 HOLICs." *ApJ* 699:143–149. doi:10.1088/0004-637X/699/1/143.

Okura, Y., Umetsu, K., and Futamase, T. 2007. "A New Measure for Weak-Lensing Flexion." *ApJ* 660:995–1002. doi:10.1086/513135.

—. 2008. "A Method for Weak-Lensing Flexion Analysis by the HOLICs Moment Approach." *ApJ* 680:1–16. doi:10.1086/587676.

Paczynski, B. 1987. "Giant luminous arcs discovered in two clusters of galaxies." *Nature* 325:572–573. doi:10.1038/325572a0.

Peacock, J. and Murdin, P. 2002. "Cosmology: Standard Model." *Encyclopedia of Astronomy and Astrophysics* doi:10.1888/0333750888/1632.

Peacock, J. A. 1999. *Cosmological Physics*.

Peacock, J. A. and Dodds, S. J. 1996. "Non-linear evolution of cosmological power spectra." *MNRAS* 280:L19–L26.

Peacock, J. A., Schneider, P., Efstathiou, G., Ellis, J. R., Leibundgut, B., Lilly, S. J., and Mellier, Y. 2006. "ESA-ESO Working Group on "Fundamental Cosmology"." Technical report.

Peebles, P. J. E. 1970. "Structure of the Coma Cluster of Galaxies." *AJ* 75:13–+.

Penzias, A. A. and Wilson, R. W. 1965. "A Measurement of Excess Antenna Temperature at 4080 Mc/s." *ApJ* 142:419–421. doi:10.1086/148307.

Percival, W. J., Cole, S., Eisenstein, D. J., Nichol, R. C., Peacock, J. A., Pope, A. C., and Szalay, A. S. 2007. "Measuring the Baryon Acoustic Oscillation scale using the Sloan Digital Sky Survey and 2dF Galaxy Redshift Survey." *MNRAS* 381:1053–1066. doi:10.1111/j.1365-2966.2007.12268.x.

Porciani, C., Dekel, A., and Hoffman, Y. 2002. "Testing tidal-torque theory - II. Alignment of inertia and shear and the characteristics of protohaloes." *MNRAS* 332:339–351. doi:10.1046/j.1365-8711.2002.05306.x.

Press, W. H. and Schechter, P. 1974. "Formation of Galaxies and Clusters of Galaxies by Self-Similar Gravitational Condensation." *ApJ* 187:425–438.

Refregier, A. and Bacon, D. 2003. "Shapelets - II. A method for weak lensing measurements." *MNRAS* 338:48–56. doi:10.1046/j.1365-8711.2003.05902.x.

Rhodes, J., Refregier, A., and Groth, E. J. 2000. "Weak Lensing Measurements: A Revisited Method and Application toHubble Space Telescope Images." *ApJ* 536:79–100. doi:10.1086/308902.

Riess, A. G., Filippenko, A. V., Challis, P., Clocchiatti, A., Diercks, A., Garnavich, P. M., Gilliland, R. L., Hogan, C. J., Jha, S., Kirshner, R. P., Leibundgut, B., Phillips, M. M., Reiss, D., Schmidt, B. P., Schommer, R. A., Smith, R. C., Spyromilio, J., Stubbs, C., Suntzeff, N. B., and Tonry, J. 1998. "Observational Evidence from Supernovae for an Accelerating Universe and a Cosmological Constant." *AJ* 116:1009–1038. doi:10.1086/300499.

Riess, A. G., Macri, L., Casertano, S., Sosey, M., Lampeitl, H., Ferguson, H. C., Filippenko, A. V., Jha, S. W., Li, W., Chornock, R., and Sarkar, D. 2009. "A Redetermination of the Hubble Constant with the Hubble Space Telescope from a Differential Distance Ladder." *ApJ* 699:539–563. doi:10.1088/0004-637X/699/1/539.

Sand, D. J., Treu, T., Smith, G. P., and Ellis, R. S. 2004. "The Dark Matter Distribution in the Central Regions of Galaxy Clusters: Implications for Cold Dark Matter." *ApJ* 604:88–107. doi:10.1086/382146.

Sanz, J. L., Herranz, D., and Martínez-Gónzalez, E. 2001. "Optimal Detection of Sources on a Homogeneous and Isotropic Background." *ApJ* 552:484–492. doi:10.1086/320550.

Sargent, M. T., Carollo, C. M., Lilly, S. J., Scarlata, C., Feldmann, R., Kampczyk, P., Koekemoer, A. M., Scoville, N., Kneib, J.-P., and et al. 2007. "The Evolution of the Number Density of Large Disk Galaxies in COSMOS." *ApJS* 172:434–455. doi:10.1086/516584.

Schneider, M. D. and Bridle, S. 2010. "A halo model for intrinsic alignments of galaxy ellipticities." *MNRAS* 402:2127–2139. doi:10.1111/j.1365-2966.2009.15956.x.

Schneider, P. and Seitz, C. 1995. "Steps towards nonlinear cluster inversion through gravitational distortions. 1: Basic considerations and circular clusters." *A&A* 294:411–431.

Schneider, P., van Waerbeke, L., Kilbinger, M., and Mellier, Y. 2002. "Analysis of two-point statistics of cosmic shear. I. Estimators and covariances." *A&A* 396:1–19. doi:10.1051/0004-6361:20021341.

Schrabback, T., Hartlap, J., Joachimi, B., Kilbinger, M., Simon, P., Benabed, K., Bradač, M., Eifler, T., Erben, T., Fassnacht, C. D., High, F. W., Hilbert, S., Hildebrandt, H., Hoekstra, H., Kuijken, K., Marshall, P. J., Mellier, Y., Morganson, E., Schneider, P., Semboloni, E., van Waerbeke, L., and Velander, M. 2010. "Evidence of the accelerated expansion of the Universe from weak lensing tomography with COSMOS." *A&A* 516:A63+. doi:10.1051/0004-6361/200913577.

Scoville, N., Abraham, R. G., Aussel, H., Barnes, J. E., Benson, A., Blain, A. W., Calzetti, D., Comastri, A., Capak, P., Carilli, C., Carlstrom, J. E., Carollo, C. M., Colbert, J., Daddi, E., Ellis, R. S., Elvis, M., Ewald, S. P., Fall, M., Franceschini, A., Giavalisco, M., Green, W., Griffiths, R. E., Guzzo, L., Hasinger, G., Impey, C., Kneib, J.-P., Koda, J., Koekemoer, A., Lefevre, O., Lilly, S., Liu, C. T., McCracken, H. J., Massey, R., Mellier, Y., Miyazaki, S., Mobasher, B., Mould, J., Norman, C., Refregier, A., Renzini, A., Rhodes, J., Rich, M., Sanders, D. B., Schiminovich, D., Schinnerer, E., Scodeggio, M., Sheth, K., Shopbell, P. L., Taniguchi, Y., Tyson, N. D., Urry, C. M., Van Waerbeke, L., Vettolani, P., White, S. D. M., and Yan, L. 2007. "COSMOS: Hubble Space Telescope Observations." *ApJS* 172:38–45. doi:10.1086/516580.

Seitz, C. and Schneider, P. 1997. "Steps towards nonlinear cluster inversion through gravitational distortions. III. Including a redshift distribution of the sources." *A&A* 318:687–699.

Semboloni, E., Mellier, Y., van Waerbeke, L., Hoekstra, H., Tereno, I., Benabed, K., Gwyn, S. D. J., Fu, L., Hudson, M. J., Maoli, R., and Parker, L. C. 2006. "Cosmic shear analysis with CFHTLS deep data." *A&A* 452:51–61. doi:10.1051/0004-6361:20054479.

Simon, P. 2007. "How accurate is Limber's equation?" *A&A* 473:711–714. doi:10.1051/0004-6361:20066352.

Smith, R. E., Peacock, J. A., Jenkins, A., White, S. D. M., Frenk, C. S., Pearce, F. R., Thomas, P. A., Efstathiou, G., and Couchman, H. M. P. 2003. "Stable clustering, the halo model and non-linear cosmological power spectra." *MNRAS* 341:1311–1332. doi:10.1046/j.1365-8711.2003.06503.x.

Smoot, G. F., Bennett, C. L., Kogut, A., Wright, E. L., Aymon, J., Boggess, N. W., Cheng, E. S., de Amici, G., Gulkis, S., Hauser, M. G., Hinshaw, G., Jackson, P. D., Janssen, M., Kaita, E., Kelsall, T., Keegstra, P., Lineweaver, C., Loewenstein, K., Lubin, P., Mather, J., Meyer, S. S., Moseley, S. H., Murdock, T., Rokke, L., Silverberg, R. F., Tenorio, L., Weiss, R., and Wilkinson, D. T. 1992. "Structure in the COBE differential microwave radiometer first-year maps." *ApJ* 396:L1–L5. doi:10.1086/186504.

Soucail, G., Mellier, Y., Fort, B., Mathez, G., and Hammer, F. 1987. "Further data on the blue ring-like structure in A 370." *A&A* 184:L7–L9.

Springel, V. 2005. "The cosmological simulation code GADGET-2." *MNRAS* 364:1105–1134. doi:10.1111/j.1365-2966.2005.09655.x.

Springel, V., White, S. D. M., Jenkins, A., Frenk, C. S., Yoshida, N., Gao, L., Navarro, J., Thacker, R., Croton, D., Helly, J., Peacock, J. A., Cole, S., Thomas, P., Couchman, H., Evrard, A., Colberg, J., and Pearce, F. 2005. "Simulations of the formation, evolution and clustering of galaxies and quasars." *Nature* 435:629–636. doi:10.1038/nature03597.

Subramanian, K. and Cowling, S. A. 1986. "On local conditions for multiple imaging by bounded, smooth gravitational lenses." *MNRAS* 219:333–346.

Tyson, J. A., Wenk, R. A., and Valdes, F. 1990. "Detection of systematic gravitational lens galaxy image alignments - Mapping dark matter in galaxy clusters." *ApJ* 349:L1–L4. doi:10.1086/185636.

van Waerbeke, L. 2010. "Shear and magnification: cosmic complementarity." *MNRAS* 401:2093–2100. doi:10.1111/j.1365-2966.2009.15809.x.

Van Waerbeke, L., Mellier, Y., Erben, T., Cuillandre, J. C., Bernardeau, F., Maoli, R., Bertin, E., McCracken, H. J., Le Fèvre, O., Fort, B., Dantel-Fort, M., Jain, B., and Schneider, P. 2000. "Detection of correlated galaxy ellipticities from CFHT data: first evidence for gravitational lensing by large-scale structures." *A&A* 358:30–44.

Viola, M., Maturi, M., and Bartelmann, M. 2010a. "Constraints on the inner density profile of dark matter haloes from weak gravitational lensing." *MNRAS* 403:859–869. doi:10.1111/j.1365-2966.2009.16165.x.

Viola, M., Melchior, P., and Bartelmann, M. 2010b. "Biases in, and corrections to, KSB shear measurements." *ArXiv e-prints* .

Walsh, D., Carswell, R. F., and Weymann, R. J. 1979. "0957 + 561 A, B - Twin quasistellar objects or gravitational lens." *Nature* 279:381–384. doi:10.1038/279381a0.

White, S. D. M. 1976. "The dynamics of rich clusters of galaxies." *MNRAS* 177:717–733.

Will, C. M. 2006. "The Confrontation between General Relativity and Experiment." *Living Reviews in Relativity* 9:3–+.

Wittman, D. M., Tyson, J. A., Kirkman, D., Dell'Antonio, I., and Bernstein, G. 2000. "Detection of weak gravitational lensing distortions of distant galaxies by cosmic dark matter at large scales." *Nature* 405:143–148.

Wolf, C., Dye, S., Kleinheinrich, M., Meisenheimer, K., Rix, H.-W., and Wisotzki, L. 2001. "Deep BVR photometry of the Chandra Deep Field

South from the COMBO-17 survey." *A&A* 377:442–449. doi:10.1051/0004-6361:20011142.

Wolf, C., Meisenheimer, K., Kleinheinrich, M., Borch, A., Dye, S., Gray, M., Wisotzki, L., Bell, E. F., Rix, H.-W., Cimatti, A., Hasinger, G., and Szokoly, G. 2004. "A catalogue of the Chandra Deep Field South with multi-colour classification and photometric redshifts from COMBO-17." *A&A* 421:913–936. doi:10.1051/0004-6361:20040525.

Wu, K. K. S., Lahav, O., and Rees, M. J. 1999. "The large-scale smoothness of the Universe." *Nature* 397:225–230. doi:10.1038/16637.

Wyithe, J. S. B., Turner, E. L., and Spergel, D. N. 2001. "Gravitational Lens Statistics for Generalized NFW Profiles: Parameter Degeneracy and Implications for Self-Interacting Cold Dark Matter." *ApJ* 555:504–523. doi:10.1086/321437.

Zeldovich, Y. B. 1972. "A hypothesis, unifying the structure and the entropy of the Universe." *MNRAS* 160:1P–+.

Zwicky, F. 1933. "Die Rotverschiebung von extragalaktischen Nebeln." *Helvetica Physica Acta* 6:110–127.

Acknowledgments

In the last months I thought a lot about this last chapter of the Thesis. Scientifically it is the most irrelevant part, but probably it will be the part the most people will read. For me it is definitely the most important chapter, in the sense that without the people I am going to thank all this work would not have been possible.

Thanks Matthias! Thanks for having chosen me to be one of your PhD students, thanks for the scientific freedom you left to me. Thanks for the support and encouragements, the long discussions about science and the world in general, for your patience and for your discreet way to correct my mistakes.

Thanks Matteo, for having introduced me into the magic world of gravitational lensing and filters. Thanks for your codes and the time you spent with me especially in the first part of my PhD.

Thanks Peter, for the very stimulating discussions we had particularly in this last year and for the pressure you put on me (maybe without realising) which helped me a lot to be focused on our common projects.

Thanks Jean-Claude and Claudia, for the time you spent with me after the coffee breaks on the stairs in front of ITA, for being friends before than colleagues, for the help you gave to me when I arrived here and the help in the last months translating German bureaucratic forms.

Thanks Carlo, Julian, Christian and Francesco! Thanks for your support, for the scientific help that I asked a lot of times and you never denied and thanks a lot for making ITA a nice and funny working environment.

Thanks to all the other ITA boys (and girls), my officemates Emanuel and Gregor, Luigi, Nils, Gero, Ana, Philipp. You made these three years in the institute a very pleasant time, which I will always happily remember.

Thanks Luca Amendola for being the second corrector of this Thesis, Eva Grebel and Karlheinz Meier for being part of my Thesis committee.

Voglio ringraziare di cuore i miei genitori, mio fratello e mia sorella. Grazie per il supporto che non mi avete mai fatto mancare da Trieste e per la libertà che mi avete sempre lasciato nel seguire le mie idee e la mia strada.

Thanks Paolo and Enrico for the unforgettable moments we spent together around the world. Planning our trips and travelling in strange places gave definitely a more spicy taste to these three years.

Thanks Olga, Gisella, Alessandra, Ioanna, Giulia, Giovanna, Eleonora, Viviana, Sara, Kelly, Vivi for your friendship, for the beautiful conversations we had, for the crazy things we did together and for the weekends spent together between Untere strasse and P11! A PhD without Bier, friends and fun is not a serious PhD!

Thanks Federica! Thanks for making me laughing a lot of times, specially when I was more depressed, for having taken care of me in these last months of the Thesis and for the very profound discussion I always had with you.

Thanks Giovanni, for the conversations we had, for your efforts in trying to understand me, for your relaxed attitude, very important for me specially in the final stages of the PhD.

Thanks Denija! How many times did I dial 1891 in these three years? I think the answer has three digits! I really don't know how the PhD would have been without you, your wisdom and also your whining during the grey German depressive days. But the biggest thank is for the help, the nice words, the presence you granted me in a very particular moment of my life. I will never forget it!

Thanks Baybars! There are a lot of things for which I must say thanks to you. In short thanks for your big support during these years from the small things (unpacking the boxes the day in which my mum came here) to the most important things (well...you know what I am talking about!). I will always remember our dinners in Handschusheim...they were really useful to have a break, make the point, and start running again...

Ad maiora...